Carrier Dynamics in Photovoltaic Nanostructures

Carrier Dynamics in Photovoltaic Nanostructures

ACADEMISCH PROEFSCHRIFT

ter verkrijging van de graad van doctor
aan de Universiteit van Amsterdam
op gezag van de Rector Magnificus
prof. dr. D.C. van den Boom
ten overstaan van een door het college voor promoties ingestelde
commissie, in het openbaar te verdedigen in de Aula der Universiteit
op woensdag 12 mei 2010, te 14.00 uur

door

Joseph Johannes Henricus Pijpers

Geboren te Geleen

Promotiecommissie:

Promotor:	prof. dr. M. Bonn
Copromotor:	prof. dr. D.A.M. Vanmaekelbergh
Overige leden:	prof. dr. C. Delerue
	prof. dr. T. Gregorkiewicz
	prof. dr. J.T.M. Walraven
	dr. C. de Mello Donegá
	dr. E. Hendry
	dr. J.B. Goedkoop

Faculteit der Natuurwetenschappen, Wiskunde en Informatica

PUBLICATIONS COVERED IN THIS THESIS

J.J.H. Pijpers, E. Hendry, M.T.W. Milder, R. Fanciulli, J. Savolainen, J. Herek, S. Ruhman, D.A.M. Vanmaekelbergh, D. Mocatta, D. Oron, U. Banin, and M. Bonn.
   Carrier Multiplication and its reduction by photodoping in colloidal InAs quantum dots, *J. Phys. Chem. C*, 111 (11), 4146, 2007

J.J.H. Pijpers, E. Hendry, M.T.W. Milder, R. Fanciulli, J. Savolainen, J. Herek, S. Ruhman, D.A.M. Vanmaekelbergh, D. Mocatta, D. Oron, U. Banin, and M. Bonn.
   Carrier Multiplication and its reduction by photodoping in colloidal InAs quantum dots, *J. Phys. Chem. C*, 112 (12), 4783, 2008

J.J.H. Pijpers, M.T.W. Milder, C. Delerue, and M. Bonn.
   (Multi)exciton dynamics and exciton polarizability in colloidal InAs quantum dots, published in *J. Phys. Chem. C*. DOI: 10.1021/jp911948z

J.J.H. Pijpers, R. Ulbricht, K.J. Tielrooij, A. Osherov, Y. Golan, C. Delerue, G. Allan, M. Bonn.
   Assessment of carrier-multiplication efficiency in bulk PbSe and PbS, *Nature Phys.* 5, 811, 2009

C. Delerue, G. Allan, J.J.H. Pijpers and M. Bonn.
   Carrier Multiplication in bulk and nanocrystalline semiconductors: mechanism, efficiency, and interest for solar cells*, Phys. Rev. B*, 81, 125306, 2010

J.J.H. Pijpers, R. Koole, W.H. Evers, A.J. Houtepen, S. Böhme, C. de Mello Donegá, D.A.M. Vanmaekelbergh, and M. Bonn.
   Ultrafast spectroscopic investigations of electron injection in PbSe quantum dot sensitized mesoporous oxide films, *submitted*

OTHER PUBLICATIONS

E. Hendry, M. Koeberg, J.J.H. Pijpers, and M. Bonn.
   Reduction of carrier mobility in semiconductors caused by charge-charge interactions, *Phys. Rev. B.*, 75, 233202, 2007

A.S. Meijer, J.J.H. Pijpers, H.K. Nienhuys, M. Bonn and W.J. van der Zande.
   A THz spectrometer based on a CsI prism, *J. Optics A*, 10, 095303, 2008

Chapter 1: Introduction

1.1 A global Energy Perspective

The supply of secure, clean, and sustainable energy is one of the major scientific and technical challenges of the 21st century. In 2001, the world energy consumption amounted to $4.25 \cdot 10^{20}$ J, corresponding to an average energy consumption rate of 13.5 terawatt (TW)[1]. The majority of this energy (86%) was obtained from fossil fuels[2]. In principle, the total fossil fuel reserves are still abundant: based on the 1998 energy consumption, 50-150 years of oil, 60-160 years of gas, and 1000-2000 years of coal and tar sands are available[3].

However, one of the major drawbacks of a fossil fuel based energy supply is the emission of CO_2. During the past 650,000 years, the atmospheric CO_2 concentration has been between 200 and 300 ppm[4]. Anthropogenic CO_2 emission from 50 years of fossil fuel combustion has raised the concentration to above 380 ppm. It has been estimated that CO_2 concentrations will reach more than double the pre-anthropogenic values within the 21st century[2]. Such high CO_2 concentrations have been predicted[4] to lead to an increase of the average temperature of the earth surface with 3-5°C. This forecast is based on natural climate changes in the past, by looking at ancient glacial cycles (going back millions of years in time)[4]. The effect of this temperature rise on the weather is not exactly known due to uncertainties in climate models, but climate scientists predict extreme rainfall and droughts, and increasing intensity of hurricanes due to rising sea temperatures. A substantial rise of sea-levels can be predicted with higher accuracy, since historical climate data documents show a clear correlation between CO_2 concentrations and the sea level[4].

A possible approach to reduce CO_2 emissions is to reduce the energy consumption, i.e. burn less fossil fuel. However, there is a direct correlation between the energy use of a country and its GDP (Gross Domestic Product). Since there exists no country developing policy against economic growth, future energy demand is expected to increase considerably as a result of economic growth and the growing world population. In light of reduction of CO_2 emissions, the main route for producing large amounts of carbon-free power is to use renewable energy. Of all the available renewable energy resources, sunlight is by far the largest resource available. The energy from sunlight that reaches the earth in 1 hour ($4.3 \cdot 10^{20}$ J) is enough to fulfill the global annual energy consumption ($4.25 \cdot 10^{20}$ J in 2001)[3]. To utilize this vast energy resource, capture and storage of solar energy is required on a large scale against low costs. Possible technologies for utilization of solar energy include:

- Solar thermal technologies: integrated capture, conversion and storage of solar energy as heat
- Biomass: storing solar energy in fast-growing crops (e.g. switch grass)
- Artificial photosynthetic systems: conversion of solar energy in chemical bonds using synthetic or biomimetic catalysts
- Photovoltaics: direct conversion of solar energy in electricity by a solar cell

This thesis focuses on investigating new concepts for the last-mentioned technology in the above list, i.e. photovoltaics. Currently, the most employed solar cell technology is based on silicon. For fundamental reasons[5] (see section 1.3), however, the maximum theoretical conversion efficiency for silicon solar cells is limited to 30% (without sun concentration). In the last decade, several promising alternatives have been proposed to overcome this upper limit in efficiency. These approaches have been called "third generation concepts", and deal with the development of highly efficient solar cells at low cost[6]. Among these concepts, different approaches to convert the sunlight more efficiently into electricity utilize nanostructured semiconducting materials like Quantum Dots (QDs)[7]. Several special properties make QDs promising for achieving better solar cell performances and these particular properties are discussed in the next sections. Besides gains in conversion efficiency, colloidal QDs are also promising from an economical viewpoint since they can be synthesized via chemical procedures at relatively low temperatures. Chemical processes are easily scalable and synthesis at low temperatures requires relatively little energy input, allowing for the production of large quantities of QDs at low cost, in contrast to the production of crystalline bulk semiconductors.

1.2 Bulk semiconductors versus Quantum Dots

Nearly all solar cell concepts make use of inorganic semiconducting materials, either in their bulk or nanostructured form. Fig. 1.1 depicts the differences in energy structure between a bulk semiconductor and a nanostructured semiconductor (in this case a QD). In bulk material, a large number of atoms (of order 10^{20} or more) is brought together to form a solid. Unlike the presence of discrete energy states in atoms, the energy diagram of a bulk material is described by the existence of energy bands and bandgaps: the formation of energy bands can be described by the Nearly Free Electron Model, in which the electrons are treated as waves that interact with the lattice potential. The electron waves reflect and refract from mirror planes that arise from the periodic crystal lattice, resulting in forbidden states (located in the bandgap) that originate from destructive interference of forward and backward travelling electron waves. Constructive interference, in contrast, results in

allowed energy levels. Since the Pauli exclusion principle prevents two identical electrons from occupying the same energy level, a buildup of occupied states with increasing energy occurs, resulting in energy bands: the distance between energy levels within these bands is negligible, as a result of which an energy band can be considered as a continuum of states (Fig 1.1). An alternative approach to describe energy bands is the Tight Binding model. This approach is analogous to the formation of bonding and anti-bonding orbitals in molecules. The electronic structure of a solid is described by a superposition of wave functions for isolated atoms located at each atomic site.
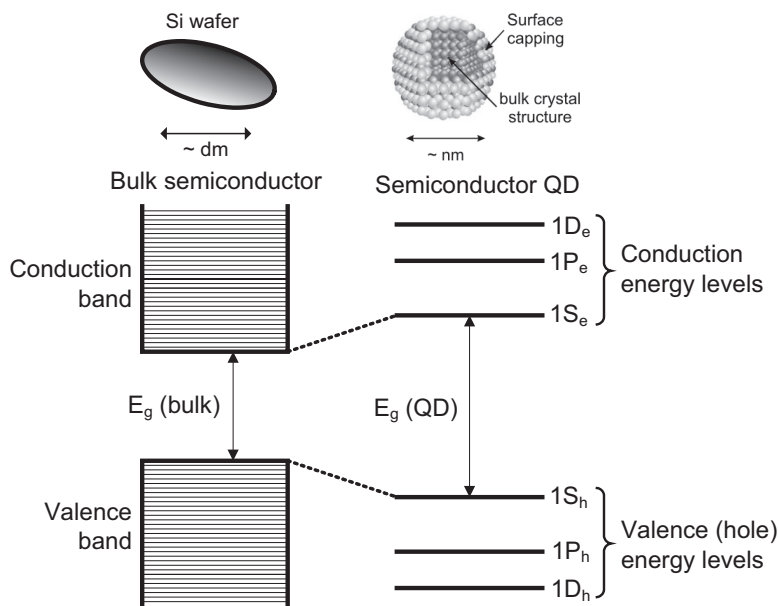

Figure 1.1 In bulk semiconductors, a continuum of energy levels is grouped in valence and conduction bands that are separated by the bandgap E_g. Because of strong spatial confinement of electron and hole wavefunctions in a QD, the energy levels are discrete and the energy gap is a function of the QD diameter.

Both the Nearly Free Electron model and the Tight Binding model result in the same energetic diagram for a bulk semiconductor (left picture in Fig. 1.1): the highest occupied energy band is named the valence band and lowest unoccupied band is the conduction band. In between these bands is the bandgap, a region in which no energy levels are allowed. The value of the bandgap, E_g, determines whether a material can be considered a semiconductor or an insulator. Materials with $E_g > 4$ eV are called insulators, whereas materials with $E_g < 4$ eV are denominated as semiconductors. As a result of this specific electronic band structure, a semiconductor has an electrical conductivity between that of a conductor and an insulator. At temperatures around 0 K, a semiconductor is insulating since all electrons

reside in the completely filled valence band where their mobility is low. By applying an electrical potential or by optical excitation, electrons are transferred from the valence band into the conduction band, leaving behind unoccupied levels in the valence band that are usually referred to as 'holes'. Both the valence band holes and conduction band electrons can contribute to the electrical conductivity. Hence, applying an electrical potential or optical excitation changes the state of a semiconductor from insulating into conducting.

In contrast to the large number of atoms in bulk material, semiconductor nanocrystals consist typically of only 100 – 10000 atoms (right panel Fig. 1.1). Spherical nano-particles (quantum dots, QDs) have the most basic nanocrystal morphology. They can be synthesized using colloidal chemistry with nearly atomic precision[8-10]. More complex geometries include nanorods (elongated nanocrystals)[10], tetrapods[11], and hyperbranched nanoparticles[12]. The energetic structure of QDs changes dramatically with respect to bulk because of quantum confinement effects[13]. Whereas in bulk, photo-generated carriers can move freely throughout the material, the quasi-particles in QDs (electrons, holes, excitons) that are generated by photo-excitation are confined in the three spatial directions of the QD volume. Since the length-scale of the quasi-particle wavefunctions is typically larger than the QD size, the QD should be considered as a *quantum box* with respect to the quasi-particles. In contrast, the QD size (1 – 10 nm) is larger than the lattice constant for the most common semiconductors and the QD can be treated as a macroscopic crystal with respect to the lattice properties. Hence, in spite of the absence of energy bands and an energy dispersion relationship, the bulk values for effective masses can be used for QDs. This approximation is generally referred to as the Effective Mass Approximation (EMA)[13].

Solving the 'particle in a box' problem for a one-dimensional potential well, results in a discrete set of energy levels (see right panel of Fig 1.1), analogous to the hydrogen atom. The energy values are given by[13]:

$$E_n = \frac{\pi^2 \cdot \hbar^2}{2m^* \cdot d^2} n \quad\quad\quad (1.1)$$

where $\hbar$ is Planck's constant, m^* is the carrier effective mass, d is the QD diameter, and n is the principal quantum number. In case the potential walls of the box are infinitely high, the wave functions vanish at the surface and the probability of finding a particle inside the QD is exactly unity (see left panel of Fig. 1.2). In reality, the potential walls often have a finite height resulting in leakage of wave functions outside the QD volume (when $|x| > d/2$, see right panel of Fig. 1.2). For visual clarity, Fig. 1.2 shows the wavefunction distribution in a one-dimensional potential well. In reality, a QD is of course a three-dimensional object, in which the energy levels are calculated using a spherical potential well.
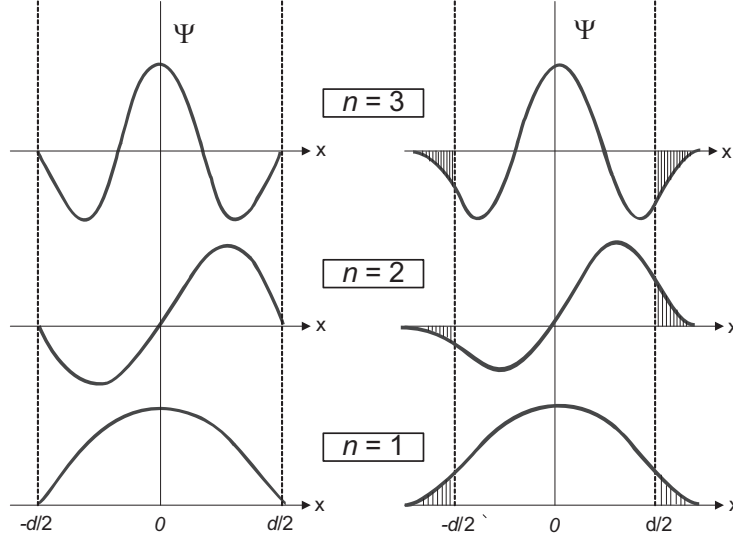
Figure 1.2 Representation of a particle in a one-dimensional box with infinite (left panel) and finite (right panel) potential walls. In both cases, there are discrete energy levels. For infinite potential walls, the probability of finding particles within the volume of the QDs is unity. For finite potentials walls, the wavefunctions extend to the region where $|x| > d/2$. This figure is a one-dimensional schematic representation of the occurrence of wavefunctions in QDs. In reality, a QD is described by a three-dimensional (in)finite spherical box.

The degree of quantum-confinement can be quantified by two quantities: the size of the quantum dots characterized by the diameter d and the exciton Bohr radius, a_b. The concept of excitons is known from bulk materials, where a positive hole and negative electron interact via Coulombic attraction to form a bound electron-hole pair. In analogy to the hydrogen atom (where there is similar Coulomb interaction between the proton and electron), the length scale of the exciton is characterized by a_b, which is a bulk material property:

$$a_b = \frac{\varepsilon \cdot \hbar^2}{\mu \cdot e^2} \tag{1.2}$$

In equation 1.2, ε is the dielectric constant of the semiconductor host material, μ is the electron-hole reduced mass ($\mu^{-1} = m_e^{-1} + m_h^{-1}$), and e is the elementary electron charge. The degree of carrier confinement in a specific QD can be evaluated by considering the total energy of an exciton in the ground state. This quantity can be expressed as a sum of the bulk bandgap energy, the Coulombic attraction energy, and the confinement energy[13]:

$$E_{1S} = E_{g,bulk} - 1.786 \frac{e^2}{\varepsilon \cdot d} + \frac{\pi^2 \cdot \hbar^2}{2\mu \cdot d^2} \tag{1.3}$$

15

Strong confinement corresponds to the limit where $d << a_b$: in this situation, the Coulomb-term contribution in equation 1.3 becomes negligible, since the Coulombic contribution to the overall exciton energy scales with $1/d$, whereas the confinement energy scales with $1/d^2$. In the situation where the contribution of Coulombic interaction to E_{1S} is negligible, electrons and holes are often treated as 'uncorrelated' particles[13]. The position of the discrete $1S$ energy states (determining the emission wavelength) of these uncorrelated electrons and holes is determined by the 'confinement term' in equation 1.3. Reducing the QD size leads to enhanced confinement, resulting in larger values for the $1S$ transition. This effect is visualized in Fig. 1.3, where the photo-emission of QDs of increasing size experiences a red-shift.

Figure 1.3 A set of flasks containing CdSe QDs of different sizes, illuminated by UV light emitting diodes. Going from left to right, the QD diameter increases; clearly, the emission wavelength shifts from blue wavelengths (large 1S transition) to red wavelengths (smaller 1S transition) for increasing the QD diameter.

1.3 Solar cells

The operating principle of solar cells relies on the conversion of energy of light into electrical energy. Semiconducting materials facilitate this conversion process in all currently-known solar cell concepts. An intrinsic semiconductor in a dark environment at room temperature is highly resistive, since most electrons reside in the completely filled valence band. Only solids with partially filled energy bands are good electronic conductors, because transport of carriers through a material occurs via unoccupied energy states. When a semiconductor is illuminated, absorption of light leads to photo-generation of electrons in the conduction band and holes in the valence bands. After this absorption process, electrons and holes need to be separated in order to prevent electron-hole recombination. In silicon

solar cells, separation of photo-generated free electrons and holes is usually achieved by a built-in electric field provided by a *p/n*-junction. By selectively doping two sides of a silicon wafer *p* type and *n* type, a potential barrier between the two regions is achieved that acts as a membrane. The *p/n*-junctions results in a low resistance path for electrons to the *n* contact and a low resistance path for holes to the *p* contact. Hence, selective extraction of electrons and holes at metal contacts can be achieved and the resulting current can do electrical work in an external circuit.

Unfortunately, the maximum *theoretical* light-to-current conversion efficiency of a single-junction solar cell is limited to 30% (the so-called Shockley-Queisser limit[5]), and efficiencies of commercial solar cells are typically only 10 – 20%. Two fundamental loss mechanisms (governing the low conversion efficiencies) for a silicon-based solar cell are depicted in Fig. 1.4. Firstly, the infrared part of the solar spectrum is not absorbed by silicon, since the infrared photons do not have enough energy to excite electrons over the bandgap (1.1 eV for silicon, corresponding to a photon wavelength of $\lambda \sim 1100$ nm). Secondly, the absorption of photons with energy in excess of the bandgap results in generation of 'hot' electrons and holes. These 'hot charge carriers' relax to the band edges via sequential emission of phonons on ultrafast timescales[14]. Via this so-called 'thermalization' process, the excess energy of visible photons is converted into phonons (or lattice vibrations). Consequently, a large part of the visible part of the solar spectrum is not converted into electricity but lost as heat.
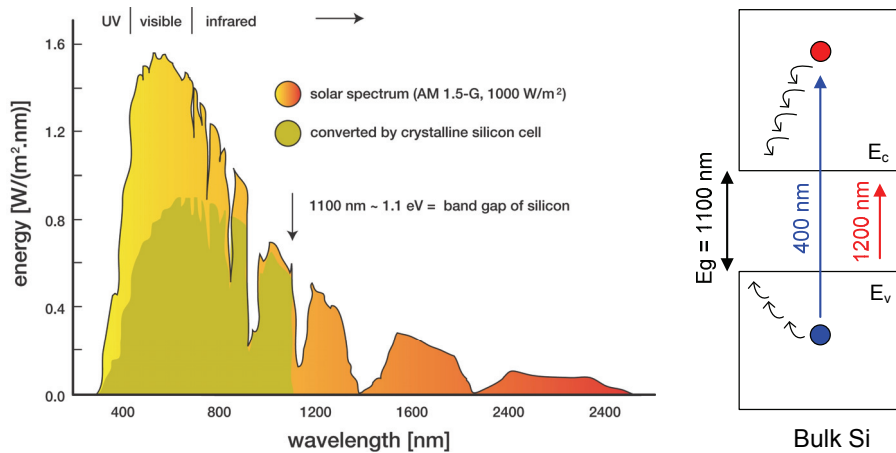

Figure 1.4 Left: solar spectrum and conversion efficiency by a silicon solar cell. Right: schematic of mismatch between solar spectrum and silicon solar cell. The excess energy of visible photons is lost via thermalization of hot carriers to the band edges. The IR part of the solar spectrum is not absorbed since the bandgap of silicon is too high.

17

The above-mentioned loss mechanisms are typical for solar cells consisting of a single semiconducting absorber material. To overcome the fundamental drawbacks of 'single-junction' silicon cells, various research strategies exist that aim at minimizing thermalization losses. One approach is a tandem cell configuration, in which multiple *p-n* junctions are stacked on top of each other, each one tuned to absorb a particular frequency of the solar spectrum. Following this strategy, highly efficient tandem cells have been reported, with an efficiency of up to 41.1% (Fraunhofer Institute, January 2009)[15]. These tandem cells consist of multiple layers of different III-V semiconductors, which are semiconducting alloys of elements from group III and V of the periodic system (e.g. GaAs). III-V materials are often chosen because of the high absorption coefficients and the possibility of tuning the bandgap by stoichiometric variation of ternary (e.g. GaInAs) and quaternary alloys[16]. As an example, Figure 1.5 schematically depicts a GaInP/GaAs cell in which the two layers are connected in series[16]. In such a configuration, the voltages of the two cells are added up. It is required that the currents from each cell are matched for an optimal cell performance. Further challenges of multi-layer tandem cells include mismatches in lattice constants and different thermal expansivity of various cell components (potentially leading to defective interfaces)[16]. The major drawback of this concept is the high production costs, explaining why this technology is currently not employed on a large scale for terrestrial applications. Nonetheless, III-V tandem cells are widely used in aerospace applications (e.g. satellites), for which the efficiency is more important than the cost of the solar cell.

As mentioned in section 1.1, QDs are promising materials for more efficient light conversion. The reasons why QDs are considered attractive, besides low-cost synthesis, include their size-tunable bandgap, the expected reduced cooling rates of hot charge carriers, and the potential occurrence of efficient Carrier Multiplication (CM). CM is the process in which absorption of a single high-energy photon results in the generation of multiple electron-hole pairs. QD solar cell concepts based on reduced cooling rates and CM
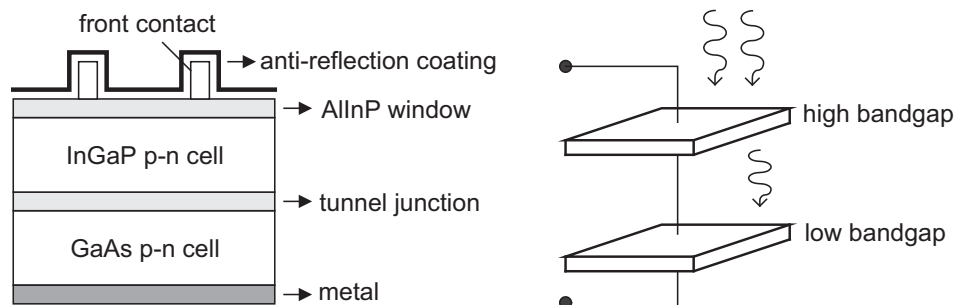

Figure 1.5 Schematic representation of a III-V tandem cell. In most multi-layer tandem cells, the cells are connected in series in a 'two terminal' configuration.

18

rely on special mechanisms of carrier relaxation in QDs due to quantum-confinement. Therefore, different carrier relaxation (or recombination) mechanisms in bulk and QDs are discussed in the next section.

1.4 Carrier recombination and relaxation in bulk and QDs

The transition in which a charge carrier is transferred from a high energy to a low energy state is called carrier recombination or relaxation[17]. In a bulk semiconductor, excited state electrons can relax via various relaxation pathways (see Fig. 1.6), the most important of which are listed below[17]:

1. Radiative recombination: electron in conduction band recombines with hole in the valence band by emitting a photon.
2. Auger recombination: three-particle process in which an electron for instance recombines with a hole by simultaneously transferring the recombination energy to a third particle. Auger rates typically depend on carrier density.
3. Relaxation of hot carriers via sequential emission of phonons (thermalization). In most bulk semiconductors, this process occurs with rates of ~ 1-2 eV/ps.
4. Trapping into defects: electrons in the conduction band relax to defect levels in the bandgap. Recombination is possible into physical defects (vacancies, grain boundaries, surface states, etc.) and chemical defects in the form of impurities.
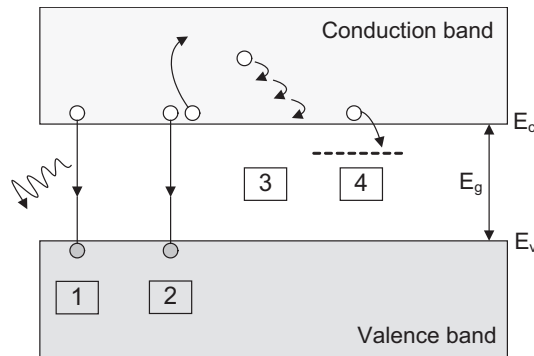
Figure 1.6 Carrier recombination in a bulk semiconductor via radiative recombination (1), Auger recombination (2), thermalization of hot carriers (3), and trapping into defect states (4).

Radiative and Auger relaxation (recombination processes 1 and 2) are inevitable relaxation processes, since the transition probabilities originate from the existence of energy bands The associated relaxation rate strength depends on the coupling between the initial and the final state and on the number of pathways via which the transition can occur (i.e. the density

of final states). The transition rate in these relaxation processes is described by Fermi's Golden rule:

$$k_{if} = \frac{2\pi}{\hbar} \left| \left\langle \Psi_f \left| V_{Coul} \right| \Psi_i \right\rangle \right|^2 \rho_f \qquad (1.4)$$

where k_{if} is the transition rate, Ψ_f and Ψ_i are the wavefunctions of the final and initial states, respectively, V_{Coul} is an operator for the Coulombic interaction that couples in the final and initial states, and ρ_f is the density of final states. The inverse of the transition rate, $1/k_{if}$, is related to the lifetime of the excited state τ.

Thermalization of hot carriers (relaxation process 3) in bulk material occurs via interactions of hot carriers with the crystal lattice, i.e. the hot carrier relaxes by sequential emission of longitudinal optical (LO) phonons (having an energy of ~ 40 meV). This relaxation process, in which the excess energy of hot carriers is converted into lattice vibrations or heat, typically occurs on a < 1 ps timescale[14]. Relaxation process 4 in Figure 1.6 involves trapping of carriers in physical defects such as vacancies or dislocations or in chemical defects such as impurities. This relaxation process can in principle be avoided by using a perfect crystalline sample with passivated surfaces.

Relaxation of carriers in QDs proceeds via the same pathways as in bulk. However, the relaxation rates of the various relaxation processes change considerably in QDs as a result of the discretization of energy levels and the spatial confinement of electronic wave functions[18]. First, by confining the wave functions in the small QD volume, carrier-carrier Coulomb interactions are strongly enhanced in QDs, leading to higher relaxation rates of radiative and Auger processes (see Eq. 1.4). Second, leakage of wave functions outside the QD (see Fig. 1.2) enhances recombination rates, since the dielectric constant outside the QDs is typically smaller than within the QD material. As a result, the leaking parts of the wave function experience strongly reduced dielectric screening and the Coulomb interaction is further enhanced. Third, the spacing between discrete energy levels is rather large, typically 250 - 550 meV for the electron $1S_e \rightarrow 1P_e$ transition[19]. Thermalization of hot carriers in bulk occurs by sequential emission of LO phonons (~ 40 meV energy)[14]. To accommodate relaxation of a hot carrier in the $1P_e$ state of a QD, however, the *simultaneous* emission of about 10 LO phonons is required, which is a phenomenon with a very low probability. The absence of a phonon-mediated relaxation channel for hot charge carriers is usually called the 'phonon-bottleneck'. Finally, the surface-to-volume ratio is much higher in QDs leading to large amount of surface defects, via which relaxation and recombination processes can proceed.

1.5 Quantum Dots as solar cell materials

As a result of the special carrier recombination and relaxation mechanisms, QDs can potentially convert parts of the solar spectrum into electricity that are not converted in conventional solar cells[7]. Below, two different concepts are discussed of how QDs can potentially absorb sunlight with fewer losses. Also, the extraction of carriers from QDs into an external circuit is discussed.

1.5.1 Hot Carrier QD solar cell

As described in section 1.3, two inherent limitations in conversion efficiency in single-gap solar cells are the rapid thermalization of hot carriers and the absence of absorption of light with below-gap photon energy. About 20 years ago, it was proposed to overcome these fundamental limitations in a so-called 'hot carrier' solar cell, in which extraction of hot carriers through selective contacts should occur before thermalization can take place[20,21]. This should be achieved in a low bandgap bulk semiconducting material (absorbing IR photons) in which intraband carrier relaxation is significantly slowed down. After photo-generation of hot carriers, the distribution of the kinetic energies of the hot carrier population is brought into equilibrium within ~ 100 fs through elastic carrier-carrier scattering[14]. This equilibrium of 'hot' carriers can be described by a chemical potential that is naturally higher than the potential of 'cold' charge carriers. In normal semiconducting materials like silicon, this equilibrated hot electron-hole plasma subsequently thermalizes via interactions with the lattice within ~ 1 ps[14]. If this electron-phonon thermalization can be slowed down significantly *and* if the hot carriers can be extracted through a selective contact, the resulting photo-voltage of the extracted carriers is higher than in a solar cell in which the excess energy of hot carriers is lost via thermalization.

Until now, the hot carrier solar cell is still conceptual and no proof-of-principle has been realized, as it has been challenging to find a suitable material in which interactions of hot carriers with the lattice are sufficiently suppressed. The emphasis of hot carrier solar cell research has been on finding suitable *bulk* semiconducting materials. Recently[7], however, it was proposed that semiconducting QDs are promising candidates for use as absorbing materials in hot carrier solar cells. The discrete and tunable energy levels make QDs potentially suitable for this purpose since (1) carrier cooling rates are potentially reduced because of the phonon-bottleneck, (2) charge and energy transfer can be controlled to a large extent, and (3) high-energy excitonic states can be occupied by a combination of inter-band (near IR – visible) and intra-band (near IR) transitions in parallel with high-energy transitions in the visible-near UV. These three characteristics are schematically represented in Figure 1.7. The concepts of Fig. 1.7 rely on the use of QD "molecules", i.e. coupled QDs with different energy gaps. Hot electrons can be generated by populating hot

energy levels directly with UV or blue photons. Subsequently, separation of the hot electron from the hole occurs by charge transfer to the adjacent QD. Charge transfer is only allowed when the alignment of energy levels between the different QDs is appropriate: without extra energy input, electrons can only go downwards in energy during a charge transfer process. Because of this requirement, it is dictated that the two QDs within the molecule should have different radii (larger radius → smaller gap) in case QDs of the same materials are used. When the molecule consists of QDs of different material, the sizes of the dots are dictated by the energy alignment between the different QDs. An alternative method of generating a hot charge carrier is that a visible photon creates an electron in the 1S (cold) energy level after which the subsequent absorption of an IR photon promotes the electron to a hot energy level. In both scenarios, the hot electron needs to be extracted into a wide-gap bulk semiconductor sufficiently fast to prevent recombination of hot carriers to cold energy levels. The utilization of hot carriers in solar cells is advantageous because it results in higher photo-voltages. The simultaneous use of a larger part of the solar spectrum (i.e. sub-gap photons) and the more efficient use of above-gap photons leads in theory to solar cell efficiencies of ~ 65% for unconcentrated sunlight[16]. Before these theoretical predictions can be fulfilled, the fundamental properties of intraband relaxation pathways for carriers within QDs and charge extraction from QDs need to be understood and controlled.
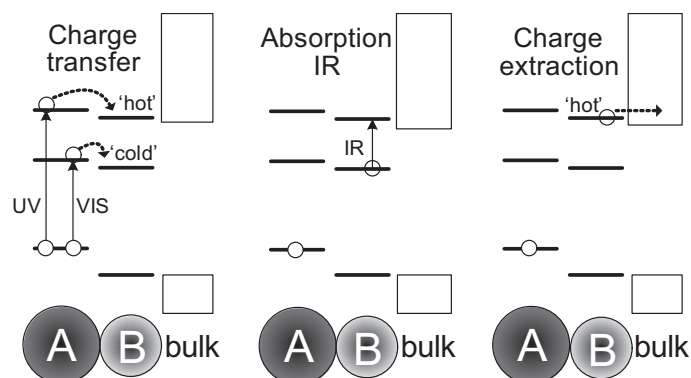

Figure 1.7 Schematic representation of a hot carrier QD solar cell. Using QD molecules, hot energy levels can be populated directly by absorption of high-energy photons, or by subsequent absorption of visible and IR light. Fast extraction of hot electrons is required to prevent recombination to cold levels.

1.5.2 QD solar cell based on Carrier Multiplication

Absorption of above-gap photons results in hot carriers with excess kinetic energy. An alternative approach to the hot carrier concept is to utilize the excess energy of the hot carriers by means of Carrier Multiplication (CM). CM is the process in which the excess energy of hot carriers is used to excite additional electrons over the bandgap. In case of

efficient CM, absorption of a single high-energy photon results in multiple electron-hole pairs, leading to higher photo-currents for a given solar flux.

CM occurs only when the photon energy E_{ph} is larger than twice the value of E_g, due to energy conservation restrictions. At visible photon energies, CM has been shown to be relatively inefficient for bulk materials like silicon[22] and germanium[23]. In bulk materials, CM occurs through impact ionization, which is a non-radiative Auger recombination mechanism occurring with a rate defined by Fermi's golden rule (equation 1.4). As such, impaction ionization is the inverse process of the Auger recombination pathway depicted as process no. 2 in Fig. 1.6. The efficiency of CM in bulk material is determined by two competitive processes for relaxation of hot carriers (see Figure 1.8): relaxation by (phonon-mediated) thermalization and relaxation via impact ionization. CM has been expected to be more efficient in QDs due to: 1) expected slow phonon-mediated relaxation because of the discretization of energy levels (phonon-bottleneck effect) and 2) stronger Coulombic interaction between carriers resulting in higher impact ionization rates[7]. The latter argument follows from equation 1.4: the rate of the Auger process is increased when Coulombic coupling between the initial and final states is stronger.
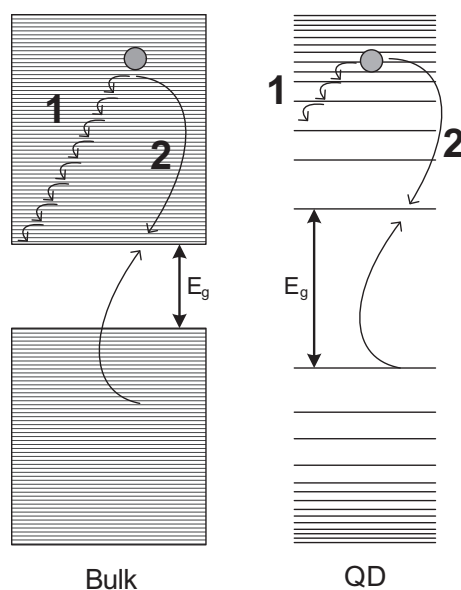

Figure 1.8 Illustration of CM in bulk and QDs. The efficiency of CM is determined by two competitive processes that are involved in the relaxation of hot carriers: 1) relaxation via sequential emission of phonons, and 2) relaxation via impact ionization. In bulk materials, the phonon-mediated relaxation pathway dominates and the CM efficiency is relatively low. CM was predicted to be enhanced in QDs because of slower phonon-mediated relaxation (due to the phonon-bottleneck effect) and the higher rates of relaxation via impact ionization resulting from stronger Coulombic interactions in QDs.

CM in QDs has received considerable attention following the initial report of efficient CM in PbSe QDs[24]. In this report, on average 2.18 excitons were observed per absorbed 3.1 eV photon in PbSe QDs with $E_g = 0.81$ eV. Over the past years, many groups have reported efficient CM in a range of QD materials including PbSe[25-27], PbTe[26], CdSe[28], and InAs[29,30]. More recently, however, these high efficiencies and even the occurrence of CM in QDs has

been questioned in PbSe[31], CdSe[32], and InAs[33,34] QDs. To evaluate the potential of CM for QD solar cells, several issues need to be addressed. First of all, the mechanism for efficient CM in QDs compared to bulk needs to be understood. A thorough understanding of the mechanism of CM in QDs would allow one to engineer the QD (material, size, surface passivation, etc.) for optimal CM efficiency. Secondly, CM generates multiple excitons per QD that need to be extracted before recombination. This is not a trivial question, since multi-excitons recombine on a timescale of typically $\sim$ 10-100 ps[35], in contrast to the long radiative liftimes ($\sim$ 100 ns) of single excitons. Hence, carrier extraction needs to take place on a picosecond timescale to utilize the full potential of CM.

Before CM can be applied successfully in a QD solar cell, fundamental knowledge on carrier dynamics in QDs needs to be acquired. The work presented in this thesis comprises research on the CM efficiency in QDs compared to bulk, the timescale of multi-exciton recombination, and carrier extraction dynamics.

1.5.3 Extraction of carriers from QDs

QD solar cells based on hot carriers or CM will only work if extraction of carriers into an external circuit can be achieved with minimum losses. A configuration to extract the photo-generated carriers from QDs is the 'Grätzel-cell' concept[36,37]. The conventional Grätzel cell is based on a nanocrystalline TiO_2 film that is sensitized with a ruthenium-based dye. The TiO_2 film is interpenetrated by a hole-transporting material, usually a liquid electrolyte containing an iodine/iodide redox couple. After absorption of sunlight by the dyes, charge separation is achieved by ultrafast injection of electrons from the excited dye into the TiO_2 anode. Subsequently, the electrons move through the semiconductor film towards the current collector and the external circuit. The remaining cationic dye is oxidized by the iodide ions in the electrolyte: $2h^+ + 2I^- \rightarrow I_2$. The formed iodine molecules migrate towards the cathode of the electrochemical cell, where the iodine is reduced to iodide by the electrons that re-enter the system via the external circuit. The idea of a QD-sensitized solar cell (QDSSC) is to replace the dyes with QDs and exploit the potential advantages of QDs like the possibility of hot carrier extraction and CM. The schematic layout of such QDSSC is given in Figure 1.9. QDs can be linked chemically to the oxide surface using bi-functional molecules such as Mercapto Propionic Acid (MPA)[38]. In an efficient QD solar cell, charge transfer of electrons into the TiO_2 should proceed faster than recombination pathways like intraband relaxation (hot carrier concept) or multi-exciton recombination (CM concept). For electron injection to be fast and efficient, the QD energy levels have to be positioned above the oxide conduction band edge. This can be achieved by careful selection of the oxide material and the QD size. In dye-sensitized Grätzel cells, electron injection has been shown to be an important limitation for device performance[39,40], even when injection from dyes is known to occur on picosecond timescales[39-41]. It is not obvious

that electron injection from QDs occurs on similarly fast timescales, since the carriers in QDs are confined in a potential well and hence have to overcome a significant potential barrier. Therefore, elucidation of carrier dynamics in oxide-QD systems and the parameters that determine electron injection from QDs is a crucial step in understanding and optimizing QD-sensitized solar cells.
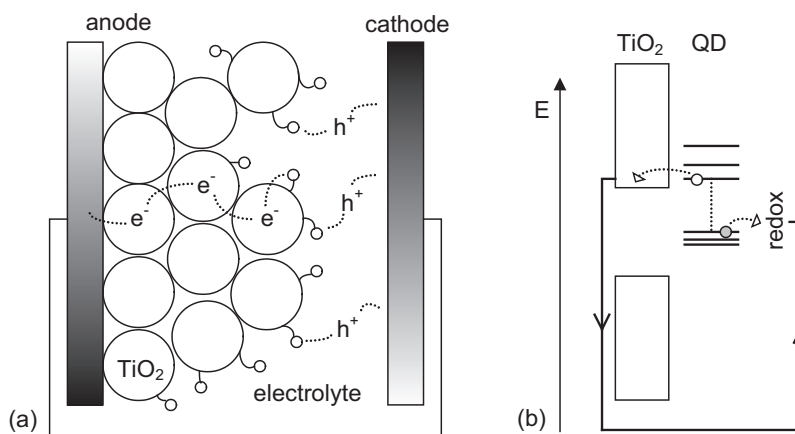

Figure 1.9 a) Schematic layout of a QD-sensitized solar cell (QDSSC), analogous to the Grätzel cell[36], in which QDs are chemically linked to a mesoporous TiO$_2$ film. After excitation, electrons are injected from the excited QD into the TiO$_2$ conduction band and the remaining holes in the oxidized QD migrate towards the cathode via an electrolyte. b) Energetic band diagram of a QD sensitized solar cell.

1.6 Outline of this thesis

This thesis aims at evaluating the potential of Quantum Dots (QDs) as light-absorbing materials in solar cells. The steps immediately following photo-excitation of QDs will determine the overall light conversion efficiency. Carrier cooling, carrier recombination, and carrier extraction into a bulk wide-bandgap semiconductor are pivotal processes that need to be understood before a QD-based solar cell can be properly designed and optimized. All these processes occur on (sub)picosecond timescales, explaining why the use of spectroscopic techniques with high time-resolution is essential. Chapter 2 deals with the experimental techniques that are used for studying ultrafast carrier dynamics in QDs. The focus in Chapter 2 lies on TeraHertz time-domain spectroscopy (THz-TDS) and on the analysis of (transient) THz spectra. Chapter 3 presents a fundamental study of carrier dynamics in InAs QDs, including exciton polarizability and intraband relaxation of hot electrons. In Chapter 4, the timescale of multi-exciton recombination is investigated and the efficiency of Carrier Multiplication in InAs QDs is determined. Subsequently, CM is investigated in bulk PbSe and PbS in Chapter 5 and a comparison is made between the

occurrence of CM in QDs and bulk material. In Chapter 6, the dynamics of charge extraction of electrons from PbSe QDs into mesoporous oxide films is investigated. Also, the effect of 'solar cell conditions' (i.e. the presence of an electrolyte) on the dynamics of charge extraction is studied in Chapter 7. Finally, an outlook on the potential of QDs as light absorbing materials in future solar cells is given in Chapter 8.

References

(1)   Energy Information Administration, *Annual Energy Outlook*, US Dept of Energy, Washington DC (2005).
(2)   Lewis, N. S.; Nocera, D. G. *PNAS* **2006**, *103*, 15729-15735.
(3)   United Nations Development Program, *World Energy Assesment Report: Energy and the Challenge of Sustainability,* United Nations, New York (2003).
(4)   Archer, D. *The Long Thaw*; Princeton University Press, 2009.
(5)   Shockley, W.; Queisser, H. J. *Journal Of Applied Physics* **1961**, *32*, 510-519.
(6)   Green, M. A. *Physica E* **2002**, *14*, 65-70.
(7)   Nozik, A. J. *Physica E* **2002**, *14*, 115-120.
(8)   Murray, C. B.; Norris, D. J.; Bawendi, M. G. *J. Am. Chem. Soc.* **1993**, *115*, 8706-8715.
(9)   Kagan, C. R.; Murray, C. B.; Nirmal, M.; Bawendi, M. G. *Phys. Rev. Lett.* **1996**, *76*, 1517-1520.
(10)   Peng, X.; Manna, L.; Yang, W.; Wickham, J.; Scher, E.; Kadavanich, A.; Alivisatos, A. P. *Nature* **2000**, *404*, 59-61.
(11)   Manna, L.; Scher, E. C.; Alivisatos, A. P. *J. Am. Chem. Soc.* **2000**, *122*, 12700-12706.
(12)   Gur, I.; Fromer, N. A.; Chen, C. P.; Kanaras, A. G.; Alivisatos, A. P. *Nano Lett.* **2007**, *7*, 409-414.
(13)   Gaponenko, S. V. *Optical Properties of Semicondcutor Nanocrystals*; Cambridge University Press, 1998.
(14)   Goldman, J. R.; Prybyla, J. A. *Phys. Rev. Lett.* **1994**, *72*, 1364.
(15)   Guter, W.; Schöne, J.; Philipps, S. P.; Steiner, M.; Siefer, G.; Wekkeli, A.; Welser, E.; Oliva, E.; Bett, A. W.; Dimroth, F. *Appl. Phys. Lett.* **2009**, *94*, 223504-223506.
(16)   Nelson, J. *The Physics of Solar Cells*; Imperial College Press, 2003.
(17)   Landsberg, P. T. *Recombination in Semiconductors*; Cambridge University Press, 2003.
(18)   Klimov, V. I. *Ann. Rev. Phys. Chem.* **2007**, *58*, 635-673.
(19)   Banin, U.; Cao, Y. W.; Katz, D.; Millo, O. *Nature* **1999**, *400*, 542-544.
(20)   Ross, R. T.; Nozik, A. J. *J. Appl. Phys.* **1982**, *53*, 3813-3818.
(21)   Würfel, P. *Solar Energy Materials and Solar Cells* **1997**, *46*, 43-52.
(22)   Kolodinski, S.; Werner, J. H.; Wittchen, T.; Queisser, H. J. *Appl. Phys. Lett.* **1993**, *63*, 2405-2407.
(23)   Koc, S. *Czech. J. Phys.* **1957**, *7*, 91-95.
(24)   Schaller, R. D.; Klimov, V. I. *Phys. Rev. Lett.* **2004**, *92*.
(25)   Schaller, R. D.; Sykora, M.; Pietryga, J. M.; Klimov, V. I. *Nano Lett.* **2006**, *6*, 424-429.
(26)   Ellingson, R. J.; Beard, M. C.; Johnson, J. C.; Yu, P. R.; Micic, O. I.; Nozik, A. J.; Shabaev, A.; Efros, A. L. *Nano Lett.* **2005**, *5*, 865-871.
(27)   Schaller, R. D.; Agranovich, V. M.; Klimov, V. I. *Nature Phys.* **2005**, *1*, 189-194.
(28)   Schaller, R. D.; Petruska, M. A.; Klimov, V. I. *Appl. Phys. Lett.* **2005**, *87*, 253102.

(29)   Pijpers, J. J. H.; Hendry, E.; Milder, M. T. W.; Fanciulli, R.; Savolainen, J.; Herek, J. L.; Vanmaekelbergh, D.; Ruhman, S.; Mocatta, D.; Oron, D.; Aharoni, A.; Banin, U.; Bonn, M. *J. Phys. Chem. C* **2007**, *111*, 4146-4152.
(30)   Schaller, R. D.; Pietryga, J. M.; Klimov, V. I. *Nano Lett.* **2007**, *7*, 3469-3476.
(31)   Nair, G.; Geyer, S. M.; Chang, L.-Y.; Bawendi, M. G. *Phys. Rev. B* **2008**, *78*, 125325-125310.
(32)   Nair, G.; Bawendi, M. G. *Phys. Rev. B* **2007**, *76*, 4.
(33)   Pijpers, J. J. H.; Hendry, E.; Milder, M. T. W.; Fanciulli, R.; Savolainen, J.; Herek, J. L.; Vanmaekelbergh, D.; Ruhman, S.; Mocatta, D.; Oron, D.; Aharoni, A.; Banin, U.; Bonn, M. *J. Phys. Chem. C* **2008**, *112*, 4783-4784.
(34)   Ben-Lulu, M.; Mocatta, D.; Bonn, M.; Banin, U.; Ruhman, S. *Nano Lett.* **2008**, *8*, 1207-1211.
(35)   Klimov, V. I.; Mikhailovsky, A. A.; McBranch, D. W.; Leatherdale, C. A.; Bawendi, M. G. *Science* **2000**, *287*, 1011-1013.
(36)   O'Regan, B.; Gratzel, M. *Nature* **1991**, *353*, 737-740.
(37)   Gratzel, M. *Nature* **2001**, *414*, 338-344.
(38)   Robel, I.; Subramanian, V.; Kuno, M.; Kamat, P. V. *J. Am. Chem. Soc.* **2006**, *128*, 2385-2393.
(39)   Haque, S. A.; Palomares, E.; Cho, B. M.; Green, A. N. M.; Hirata, N.; Klug, D. R.; Durrant, J. R. *J. Am. Chem. Soc.* **2005**, *127*, 3456-3462.
(40)   Koops, S. E.; O'Regan, B. C.; Barnes, P. R. F.; Durrant, J. R. *J. Am. Chem. Soc.* **2009**, *131*, 4808-4818.
(41)   Tachibana, Y.; Moser, J. E.; Gratzel, M.; Klug, D. R.; Durrant, J. R. *J. Phys. Chem.* **1996**, *100*, 20056-20062.

Chapter 2: Experimental Techniques and Analysis

2.1 The TeraHertz frequency

Spectroscopy is the detection and analysis of the interaction of light with atoms, molecules, and solid-state materials. Different types of resonances are associated with different regions of the electromagnetic spectrum. Fig. 2.1 summarizes the wavelength and frequency regions of the electromagnetic spectrum along with some specific excitations for each region. Typical timescales of the oscillation period of these different excited species are also given in Fig. 2.1. This schematic illustrates that THz light is very suitable to study rotational transitions of molecules and electronic motion in conducting materials. However, it was not until the late 1980's that THz spectroscopy was established as a mature technology[1,2]. This is primarily because of the difficulty of generation and detection of THz radiation[3]. A frequency of 1 THz corresponds to a photon energy of 4 meV, which is much less than the electronic transitions of semiconductors that are usually used in sources or detectors of optical light.
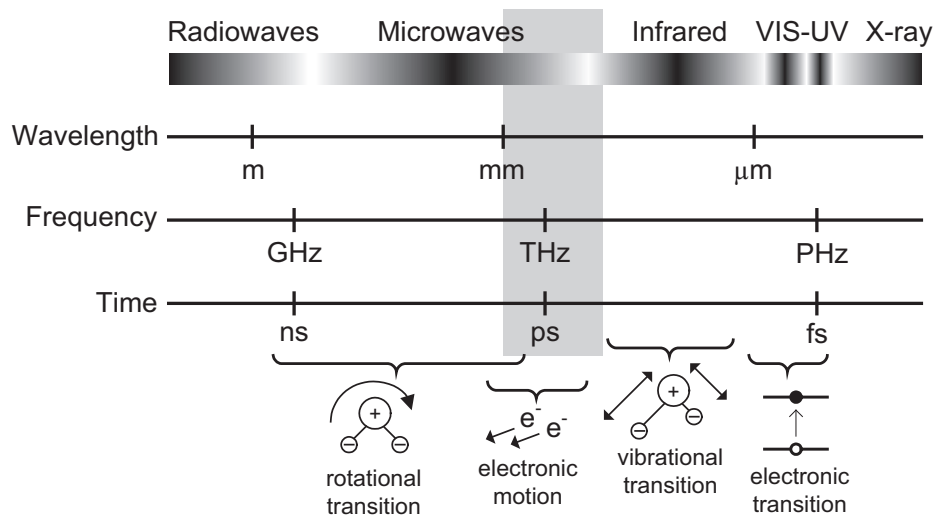

Figure 2.1 The electromagnetic spectrum from radiowaves to the x-ray region. Rotational, vibrational, and electronic transitions are shown along with electronic motion. The area accessible with THz spectroscopy is shown in shaded grey.

On the long wavelength side of the electromagnetic spectrum, GigaHertz and MegaHertz radiation can be easily generated with electronic devices. However, scaling GigaHertz electronics to operate in the THz region is limited by the frequency response of such devices. Because of the difficulty of generating and detecting light of THz frequencies, the spectral region between 'electronics' and 'photonics' has often been referred to as the 'THz gap'. Spectroscopy in this THz region has become possible only after the realization of the generation and detection of single-cycle THz pulses by means of photoconductive antennas[1,2] and optical rectification[4]. After this technological breakthrough, the technique has been used for time-resolved studies of polar and non-polar liquids[5-7], biological media[8], and solid-state materials like semiconductors[9-11], conducting polymers[12,13], and superconductors[14]. Most relevant for solar cell research is the ability of THz spectroscopy to study ultrafast carrier dynamics in various types of semiconductors. The oscillating THz field interacts strongly with charge carriers and the obtained frequency dependent response gives information on the nature of carrier conductivity in a material. As such, THz spectroscopy has been widely used to investigate the fundamental properties of a wide range of semiconductors used in photovoltaic applications, including bulk inorganic semiconductors[9,15], mesoporous semiconducting films[16], semiconducting polymers[12,13] and QDs[15,17,18]. Also, charge separation dynamics and transport properties in nanostructured QD- and dye-sensitized solar cells can be studied using light of THz frequencies as a probe, as will be shown in this thesis. In this chapter, we will first describe the experimental setup and the characteristics of the THz light that we use as a probe. After discussing how the photoconductivity of a material can be extracted from the interaction of that material with the THz probe, we will discuss the THz response of three different types of charge carriers, i.e. free carriers in bulk semiconductors, confined carriers in QDs, and carriers in mesoporous semiconducting films.

2.2 TeraHertz time-domain spectroscopy (THz-TDS)

The goal of many of the THz experiments presented in this thesis is to determine the transient photoconductivity in a semiconducting material. For this purpose, we generate electrons in the conduction band by a visible pump pulse and we probe the carriers in the sample with a second pulse of THz frequencies. Hence, THz-TDS is a pump-probe technique. When delaying the probe pulse with respect to pump, the photoconductivity can be determined as a function of the pump-probe delay (the time in between arrival of the pump and the probe pulse). Since both the pump and the probe pulse have (sub)picosecond duration, the photoconductivity can de determined with ultrafast time-resolution. An additional advantage of THz-TDS is the contact-free nature of the experiment, since both

pump and probe are freely propagating optical pulses. This is especially advantageous when studying the photoconductivity in nanostructured materials, where it is difficult to apply electrical contacts directly.

2.2.1 The THz waveform

Fig. 2.2 shows a typical measurement of the THz electric field as measured by the THz spectrometer (see section 2.2.2). This waveform was measured in dry N_2 to avoid absorption of THz light arising from rotations of gas-phase water molecules, since these resonances are located in the THz frequency region[19]. As can be seen in Fig. 2.2, the THz pulse is essentially a single oscillation of an electric field with a period of approximately 1 picosecond and a peak electric field of ~ 1 kV/cm. This field strength is sufficiently low to keep the system in the weak perturbation limit and, hence, the THz pulse acts as a true probe pulse. THz-TDS is special in the sense that both amplitude and phase of the probe pulse are recorded. This is in contrast to conventional Transient Absorption spectroscopy, where only the time-dependent spectral amplitude of the probe light is measured. Fourier transforming the time-domain THz trace into the frequency domain yields the power spectrum and the frequency-dependent phase of the THz pulse. As can be seen in Fig. 2.2, the THz pulse covers a wide spectral range from 0.2 – 2 THz. The advantage of detecting the amplitude *and* the phase is that both the real *and* imaginary components of the complex conductivity can be extracted simultaneously from the THz data (see section 2.3).
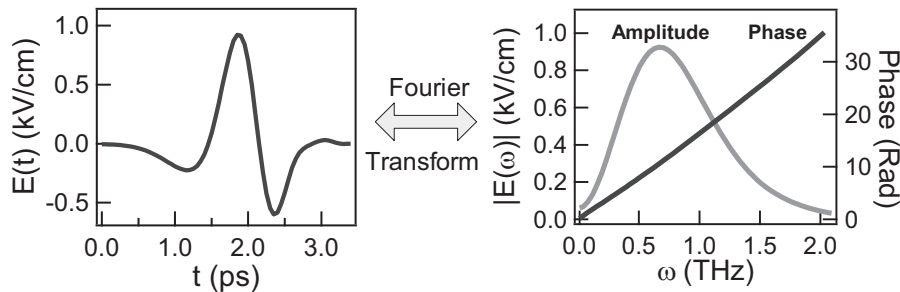
Figure 2.2 Typical waveform of a THz pulse propagating through air $E_{air}^{out}(t)$, measured by electro-optic sampling. Fourier-transforming the time-domain waveform yields the spectral amplitude and the phase of the THz electric field.

2.2.2 The THz-TDS spectrometer

The layout of the THz time-domain spectrometer is shown in Fig. 2.3. The light source used to operate the spectrometer is a pulsed laser system that is based on a Coherent Legend regenerative amplifier (Regen), seeded by a Coherent Verdi (790 nm central wavelength, 110 fs pulse duration FWHM, 80 MHz repetition rate, 500 mW output power). The Regen

is pumped by a Coherent Evolution system (527 nm central wavelength, 20 ns pulse duration FWHM, 1 KHz repetition rate, 23 W output power). The amplified output of the Regen is centered at 800 nm has a pulse duration of 110 fs FWHM and a repetition rate of 1 kHz. Of the 2.5 W output power of the Regen, ~ 900 mW is used to run the pump-probe THz-TDS setup.
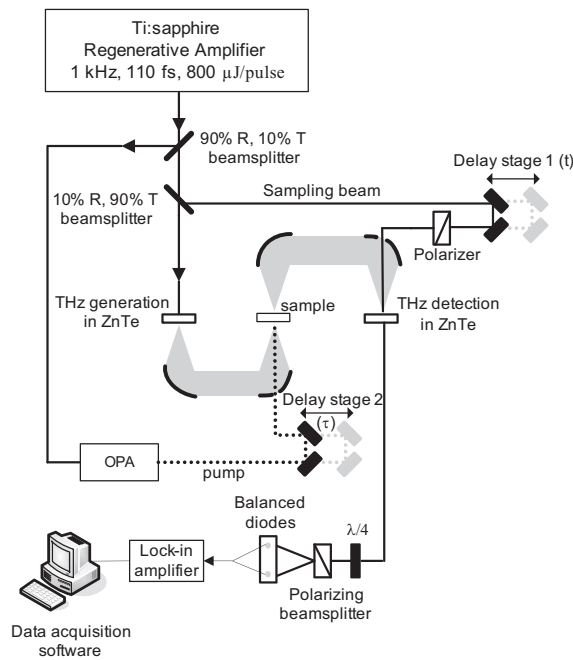

Figure 2.3 Schematic layout of the THz spectrometer. THz radiation is generated in a ZnTe crystal by means of optical rectification. The resulting divergent THz beam is collimated and focused on the sample using a pair of off-axis parabolic mirrors. Transmitted THz pulses are recollimated and focused on a second ZnTe crystal for detection via electro-optic sampling: the THz pulse induces birefringence in the ZnTe detection crystal and as a result, the polarization of the 800 nm sampling beam is changed from perfectly linear to slightly elliptical. By scanning the temporally short 800 nm sampling beam over the THz field using delay stage 1, the THz electric field can be recorded as a function of time *t*. In pump-probe experiments, a pump pulse is used to excite the sample and information on carrier dynamics is obtained by varying the pump-probe delay τ using delay stage 2.

For the THz generation and detection, 10% of the incoming laser beam is used (90 μJ/pulse). THz radiation is generated in a phase-matched manner by optical rectification[4] in a ZnTe crystal (<110> orientation, 10x10x1 mm thickness, purchased from MaTeck). The ZnTe generation crystal is pumped with a slightly focused beam (~ 3 mm diameter) of 800 nm light (80 mW power). The THz light exits the ZnTe generation crystal slightly divergent and is first collimated and subsequently focused on the sample using a pair of off-axis parabolic mirrors. The sample can be mounted optionally in a closed cycle helium cryostat (Air Products) for temperature dependent measurements between 20 – 300 K.

The transmitted THz pulses are recollimated and focused on a second ZnTe detection crystal by another pair of parabolic mirrors, where they are imaged through electro-optical sampling[20]. As a result of the strong electro-optical activity of ZnTe, the THz field induces a small birefringence in the detection crystal. This induced birefringence can be probed

using 800 nm laser pulses with linear polarization as a sampling beam (< 1 μJ/pulse). Since the pulse duration of the sampling beam pulses (110 fs) is much shorter than THz pulse (several picoseconds), the sampling beam samples the quasi-instantaneous field strength at different times within the duration of the THz pulse. Upon passing through the birefringent ZnTe crystal, the initially linearly polarized sampling pulse becomes elliptically polarized. The *s* and *p* components of the elliptically polarized sampling pulse are separated by a second polarizer, which is a Wollaston prism, and the difference in intensity of the two polarization components is detected with balanced diodes. A quarter wave plate is used to ensure that the system is operating in the linear regime. Hence, the output signal is proportional to the magnitude and the sign of the field of the THz pulse at each point in time as defined by the arrival of the sampling pulse. By varying the delay (*t*) between the THz and the sampling pulse, one can reconstruct the temporal profile of the detected THz field, *E(t)*. Since this detection scheme relies on 'gating' with 110 fs sampling pulses, the time-resolution is better than the duration of the THz pulse duration[21], and transient photoconductivity in materials can be studied with subpicosecond time-resolution.

2.2.3 A typical THz experiment

The response of a material to the THz probe can be described in terms of the complex refractive index (n_{sample}). The real part of this complex parameter describes the refraction of THz light by the investigated material, whereas the imaginary part is associated with absorption of THz light by a material. The refractive index is related to the complex dielectric function (ε_{sample}) through:

$$\varepsilon_{sample} = n_{sample}^2 \tag{2.1}$$

Fig. 2.4(a) depicts the measurements of the THz field transmitted through air $E_{air}^{out}(t)$ and transmitted through the unexcited sample $E_{sample}^{out}(t)$, in this case a silicon wafer.

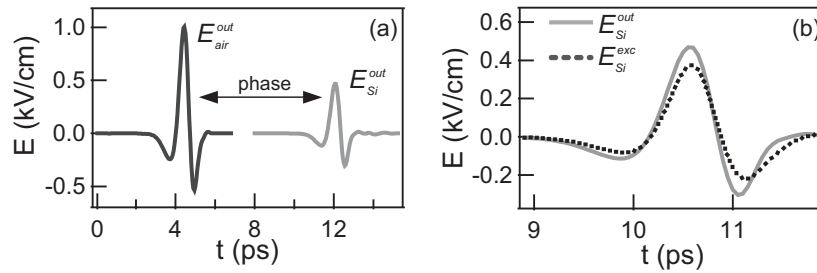**Figure 2.4** Measured waveforms in a typical THz-TDS experiment. (a) THz field transmitted through air (black line) and unexcited silicon (gray line). The scans contain both amplitude (absorption) and phase (refraction) information. (b) Transmitted THz fields through unexcited (gray solid line) and excited (black dashed line) silicon, required to extract the real and imaginary photoconductivity.

33

The refractive index of silicon at THz frequencies can be obtained from the delay of $E_{sample}^{out}(t)$ with respect to $E_{air}^{out}(t)$ in combination with knowledge of the sample thickness. The reduction of the amplitude of the THz field is related to reflection losses at the air-sample and sample-air interfaces and to absorption of THz radiation by the (unexcited) sample.

The main focus in many THz-TDS measurements is, however, to extract the THz response of a photo-excited sample in a pump-probe configuration. After photo-excitation of a material, the complex refractive index and dielectric function are described by $n_{sample}+\Delta n$ and $\varepsilon_{sample}+\Delta\varepsilon$, respectively, where Δn and $\Delta\varepsilon$ are the photo-induced changes in the refractive index and dielectric function, respectively. The complex photoconductivity of the material can be related to Δn (or, equivalently, to $\Delta\varepsilon$) by[6]:

$$\Delta\sigma(\omega) = -2i\omega\varepsilon_0 n_{sample}\Delta n \tag{2.2}$$

where ω is the angular frequency and ε_0 is the vacuum permittivity. The unit of the photoconductivity is Siemens per meter (S/m, SI units). In a typical pump-probe measurement, the pump beam is chopped and $\Delta E(t)$ is measured, which is the difference between the THz field transmitted through an unexcited sample $E_{Si}^{out}(t)$ and the transmission through the excited sample $E_{Si}^{exc}(t)$. As can be seen in Fig. 2.4(b), $E_{Si}^{exc}(t)$ has a smaller amplitude than $E_{Si}^{out}(t)$ and is also delayed slightly. This THz response originates from the interaction of the THz field with the photo-generated carriers in the silicon wafer. Combining $\Delta E(t)$ with $E_{sample}^{out}(t)$ allows extracting the real and imaginary part of the photoconductivity σ (see section 2.3). Throughout this thesis, $E_{air}^{out}(t)$ and $E_{sample}^{out}(t)$ are measured for determining the response of the unexcited sample (described by n and ε), whereas $E_{sample}^{out}(t)$ and $E_{sample}^{exc}(t)$ are used to extract $\Delta\sigma$, which is related to the modified THz response due to photo-excitation.

Depending on the material, the bandgap of a semiconductor varies between ~ 0.25 and 4 eV. In our setup, excitation wavelengths of 800 nm (1.55 eV), 400 nm (3.1 eV) and 266 nm (4.66 eV) are readily available from the fundamental laser beam and its higher harmonics. Conversion of the fundamental 800 nm laser beam into other excitation wavelengths from the UV to the IR was done by optical parametric generation and amplification in commercial OPA's (TOPAS, Light Conversion Inc. and Opera, Coherent). In all pump-probe experiments, the beam size of the pump beam (~ 5 mm diameter) is larger than the THz beam size (~ 2 mm diameter) to ensure that a homogeneously excited region is probed. Optionally, the pump beam profile can be homogenized using diffusers in case an homogeneous excitation fluence is an absolute prerequisite for quantitative determination of the carrier density (see e.g. Chapter 5).

2.3 Determination of the complex parameters n, ε, and $\Delta\sigma$

In this paragraph, the general concepts of extracting the complex parameters n, ε, and $\Delta\sigma$ from the time-domain THz waveforms[6] are discussed. In the case of an unexcited sample, the THz refractive index n is obtained by comparing the THz electric field measured with ($E_{sample}(t)$) and without ($E_{air}(t)$) the sample. The formulation below is fully equivalent to the extraction of the complex dielectric function to characterize the material response (see equation 2.1). Fig. 2.5(a) illustrates schematically the transmission of a THz pulse though a sample -in this case a piece of semiconducting material- that is surrounded by air. A THz pulse with electric field $E_{THz,in}$ enters a sample of thickness d at an angle of incidence θ. The sample has a complex THz refractive index n_2 and at the first interface, the THz pulse experiences a reflection coefficient of r_{12} and a transmission factor t_{12} according to the Fresnel equations[22]. The transmitted THz field then propagates through the sample and undergoes a change in amplitude by the complex factor p_2. Finally, the pulse leaves the sample through the second interface with an additional transmission factor of t_{21}. In the case of large refractive index mismatches and thin samples, multiple reflections at the interfaces also contribute to the emerging THz field, as is explained below.
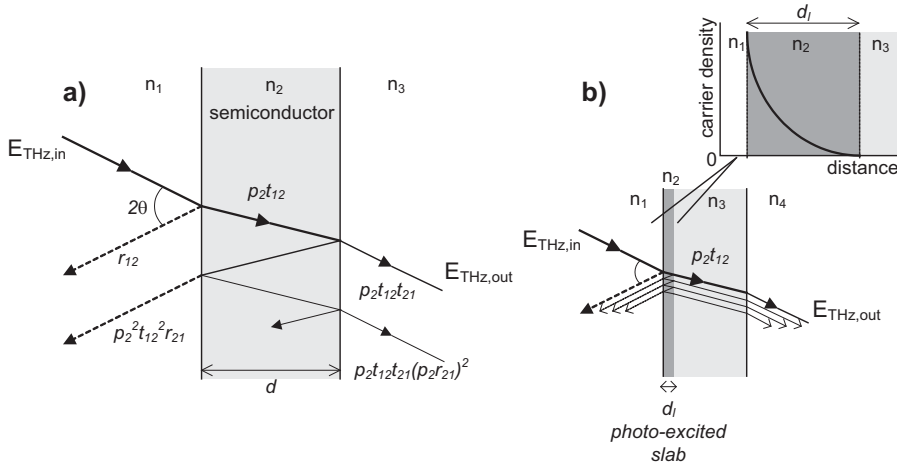
Figure 2.5 (a) schematic representation of the transmission of the THz field through a semiconducting sample that is surrounded by air ($n_1 = n_3 = 1$). The THz field enters the sample of refractive index n_2 and thickness d. The emerging THz field from the sample, $E_{THz,out}$, is related to the incoming THz field via the Fresnel factors, as described in the text. (b) Transmission of the THz field through a photo-excited sample. In many semiconductors, the penetration depth of optical light is small and a thin slab of material is photo-excited (inset: exponential excitation profile in slab). In case the slab is much thinner than the THz wavelength, the excitation density (and hence the refractive index) in the slab is approximated to be homogeneous. Taking multiple reflections within the slab into account, the emerging THz field is formed by constructive interference, as defined by the Fresnel factors described in the text.

The emerging THz field, $E_{sample}^{out}(\omega)$ in Fig. 2.5a is given by[6]:

$$E_{THz,out}(\omega) = \frac{p_2 t_{12} t_{21}}{1 - (p_2 r_{21})^2} E_{THz,in}(\omega) \qquad (2.3)$$

Equation 2.3 is written in the frequency domain as a function of the angular frequency ω. The numerator in this equation accounts for directly transmitted THz radiation, whereas the $(p_2 r_{21})^2$-term in the denominator accounts for multiple reflections. These reflections have to be taken into account when $2n_2 \cdot d/c$, i.e. the propagation time of the reflected THz pulse through the sample (where c is the speed of light) is comparable to, or smaller than, the typical THz pulse duration. For such samples, it is assumed that the contributions to $E_{sample}^{out}(\omega)$ from multiple reflections overlap spatially and add coherently. The contribution of multiple reflections can be neglected in case of relatively thick samples, where the directly propagated THz pulse is temporally separated from the contributions associated with reflections at the interfaces. For the case of normal incidence, the Fresnel factors in equation 2.3 are given by[6,22]:

$$t_{12} t_{21} = \frac{4 n_1 n_2}{(n_1 + n_2)^2} \, , \, r_{21} = \frac{n_1 - n_2}{n_1 + n_2} \, , \text{ and } \, p_2 = \exp(\frac{i n_2 \omega \cdot d}{c}) \qquad (2.4)$$

In an additional measurement, the THz transmission is determined without the sample. In this situation, $E_{air}^{out}(\omega)$ also obeys equation 2.3 but the refractive index of the sample is substituted by that of air. When knowing the sample thickness d, the refractive index of the sample can be obtained from a comparison of the measured waveforms $E_{air}^{out}(\omega)$ and $E_{sample}^{out}(\omega)$.

In the majority of the experiments presented in this thesis, the behavior of the photo-excited sample is investigated. This situation is represented in Fig. 2.5(b), where the photo-excited region is denoted as a thin slab. The excitation profile within the sample usually obeys the Lambert-Beer equation and the excitation density decreases exponentially with distance (see inset Fig. 2.5(b)). In many semiconductors, the penetration depth of the pump beam at optical excitation wavelengths is much smaller than the typical wavelength of THz radiation (at 1 THz, $\lambda = 300$ µm). In this limit, the photo-excited region in the sample can be approximated as a slab with homogeneous excitation density, because different parts of the THz pulse always experience the same excitation density, when scanning the THz-pulse in the time-domain. The opposite limit occurs when the absorption is very weak and most of the pump light is transmitted through the sample. In this case, the excitation density is approximately constant as a function of the distance in the sample and all material in the sample is homogeneously excited.

In these extreme limits, the photoconductivity, or equivalently the photo-induced refractive index Δn_2, can be extracted from an adapted version of equation 2.3[6]:

$$E_{sample}^{out}(\omega) + \Delta E_{sample}^{out}(\omega) = \frac{p_2^* t_{12}^* t_{21}^*}{1-(p_2^* t_{21}^*)^2} E_{THz,in}(\omega) \tag{2.5}$$

where the asterisks indicate that the Fresnel factors now describe the response to the photo-excited sample. Usually, the changes in the THz waveform as a result of photo-excitation, $\Delta E_{sample}^{out}(\omega)$ are at most a few percent, indicating that we are operating the operating in the regime of weak perturbation. Hence, the Fresnel factors can be linearized for small changes[6] and the change in the refractive index can be inferred from the changes in the transmitted THz pulses through:

$$\Delta n_2 = \left[\frac{i\omega \cdot d_l}{c} - \frac{n_2 - n_1}{n_2(n_2+n_1)} + MR \right]^{-1} \frac{\Delta E_{sample}^{out}(\omega)}{E_{sample}^{out}(\omega)} \tag{2.6}$$

Applying this equation to the situation of strong absorption, Δn_2 corresponds to the change of the refractive index in the excited slab, of which the thickness is defined by the penetration depth d_l (which is much smaller than the sample thickness d). In case of homogeneously excited samples, Δn_2 corresponds to the change of the refractive index over the full thickness of the sample (in this situation, d_l in equation 2.6 is equal to d). In a typical photo-excitation experiment, $E_{sample}^{out}(\omega)$ is recorded by chopping the THz generation beam, whereas $\Delta E_{sample}^{out}(\omega)$ is recorded while the pump beam is chopped. The term in the bracket in equation 2.6 describes that the transmitted THz field is affected by pump-induced changes via modification of propagation losses, changes in surface reflections, and a contribution from multiple reflections, respectively. The latter contribution is given by[6]:

$$MR = \frac{2(p_2 r_{21})^2}{1-(p_2 r_{21})^2}\left(\frac{i\omega \cdot d_l}{c} - \frac{2n_1}{(n_2^2 - n_1^2)} \right) \tag{2.7}$$

Throughout this thesis, the response of a photo-excited material to the THz field is given by the photoconductivity. This quantity is related to Δn_2 through[6]:

$$\Delta \sigma = -2i\omega\varepsilon_0 n_2 \Delta n_2 \tag{2.8}$$

2.4 Interaction of THz radiation with carriers

The behavior of charge carriers in semiconductors (determining the type of photoconductivity) depends on the semiconductor material, the morphology, and the temperature. Three different types of conductivities in the THz window are discussed below. The discussed models are representative for several systems that are investigated in this thesis.

2.4.1 THz response to free carriers (Drude model)

The conductivity of charge carriers in bulk semiconductors is usually described by the Drude model. In this model, carriers are treated as an ideal gas of free particles, interacting with the crystal lattice (i.e. impurities or phonons) only through momentum-changing collisions. In the absence of an electric field, the movement of charge carriers has no preferential direction but exhibits a random walk throughout the lattice, characterized by the mean free path in between collisions, l_0. In the presence of an externally applied electric field, the carriers are accelerated along the direction of the applied field. In a quantum mechanical picture, electrons and holes are pictured as waves that can propagate through the oscillating potential of the perfect crystal lattice. In a perfect lattice at cryogenic temperatures, the acceleration of the carriers is not damped by interaction with the lattice. In reality, however, each material contains a certain amount of defect centers (of structural or chemical nature) and carriers will scatter from these impurities. At low temperatures, scattering from impurities is the dominating scattering mechanism. At elevated temperatures, carriers will predominantly scatter with phonons. Scattering from impurities and phonons are the dominant processes that are damping the drift motion of free carriers. As a consequence, the carrier motion can be characterized by a scattering time τ_r (the average time in-between scattering events) and a net drift velocity v_d, which is much smaller (typically $\sim 10^{-3}$ m/s) than the thermal velocity of the carriers (typically $\sim 10^5$ m/s).

The motion of a carrier that is accelerated by a time-varying electric field and damped by scattering from impurities or phonons can be described by a first order differential equation[23]. In the case of applying an sinusoidal electric field, $E(t) = E_0 e^{i\omega t}$, the solution of this differential equation yields the drift velocity as a function of time[23,24]:

$$v_d = -\frac{e\tau_r}{m^*}\frac{1}{1-i\omega\tau_r}E_0 e^{i\omega t} \qquad (2.9)$$

where m^* is the carrier effective mass and e is the electron charge. The carrier mobility $\mu(\omega)$ is the proportionality factor between $E(t)$ and v_d and is defined as:

$$\mu(\omega) = \frac{e\tau_r}{m^*}\frac{1}{1-i\omega\tau_r} \qquad (2.10)$$

The magnitude of $\mu(\omega)$ indicates how easy carriers can move through a material. From equation 2.10, it follows that mobility is largely determined by the carrier effective mass and the scattering time: the former quantity is a material property whereas the latter is determined by the quality of the sample (amount of defects per unit volume), the temperature (availability of phonons), and the carrier density (carrier-carrier interactions). The macroscopic electrical properties of a material depend on the carrier mobility *and* the carrier density, N. Therefore, the conductivity of a macroscopic material is defined as:

$$\sigma(\omega) = Ne\mu(\omega) \qquad\qquad (2.11)$$

which is equivalent to:

$$\sigma(\omega) = \frac{\varepsilon_0 \omega_p^2 \tau_r}{1 - i\omega\tau_r} \text{ where } \omega_p^2 = \frac{e^2 N}{\varepsilon_0 m^*} \qquad\qquad (2.12)$$

This relationship is called the Drude equation, in which ω_p is the plasma frequency and ε_0 is the vacuum permittivity. Figure 2.6(a) plots the real and imaginary part of the conductivity. The resonance for absorption of electromagnetic light by free carriers (peak of the real conductivity) is positioned at $\omega = 0$. In many types of harmonic motion, like vibrations and rotations of molecules, the resonance is positioned at $\omega > 0$. The position of the resonance is determined by the force constant, which is the proportionality factor between the displacement of the particle and its restoring force. For free carriers, the force constant is zero, giving rise to a linear damping of the electronic motion and explaining why the resonance in the Drude model is positioned at $\omega = 0$. Figure 2.6(b) shows the conductivity of free carriers in germanium in the frequency window of our THz spectrometer. The sample was excited with 400 nm pulses and the conductivity was
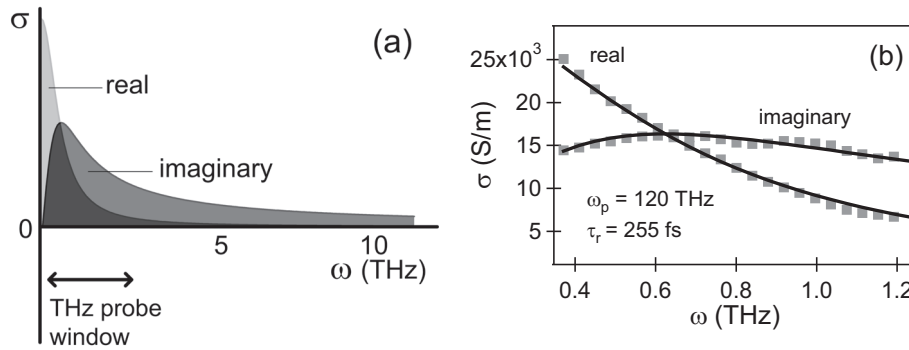
Figure 2.6 a) plot of the Drude equation as a function of the angular frequency. The resonance of free carriers is positioned at $\omega = 0$ and the frequency at which the real and imaginary conductivity cross, is determined by the scattering time: $\tau_r = 1/2\pi\omega_{cross}$. b) measured conductivity of free carriers in germanium (grey dots), after excitation with 400nm pulses. Fitting the data (spheres) with the Drude equation (solid line) yields values for ω_p and τ_r.

39

measured at a pump-probe delay of 50 ps. Clearly, the real part of the conductivity continuously increases towards lower frequencies, which is indicative of the free carrier resonance at $\omega = 0$. The frequency at which the real and imaginary conductivity cross, defines the scattering time ($\tau_r = 1/2\pi\omega_{cross}$). The data can be fitted accurately with the Drude model (solid line in Fig. 2.6b), yielding ω_p and τ_r. The strength of THz-TDS is illustrated clearly by Fig. 2.6(b): the fits of the two traces (real and imaginary photoconductivity) using the Drude equation describe the offset, the curvature and the amplitude of the two curves surprisingly well, using only two global parameters, ω_p and τ_r. Hence, THz-TDS measurements are excellently suited for determining the two key parameters of the photoconductivity, ω_p and τ_r in a bulk semiconductor like germanium.

The Drude model as discussed above is a simple model that describes the electrical properties of many materials surprisingly well. However, the model is based on a number of drastic simplifications that makes it not generally applicable. First of all, the interaction of carriers with the lattice is only incorporated by scattering processes, and Coulomb interactions are neglected. For highly polarizable materials, the Coulomb interaction of charge carriers with the charged lattice should be taken into account. For very strong carrier-lattice interactions, the carriers may become self-trapped and transport occurs by a hopping process. Secondly, holes and electrons are treated as an ideal classical gas, i.e. interactions between them are neglected. It has been demonstrated, however, that carrier-carrier interactions are significant at high carrier densities (especially in materials with low dielectric constants)[25]. In this situation, the Drude model (including only scattering with phonons) does not correctly describe the conductivity anymore, but has to be extended with carrier-carrier interactions. And finally, all carriers are treated as equivalent particles, whereas in reality, there is a distribution of electron velocities and scattering times. These three simplifications make the Drude model inappropriate for describing the conductivity in certain situations, e.g. when the carrier density is high and carrier-carrier interactions cannot be neglected. However, in many situations, the Drude model is a very suitable description to describe the electrical behavior of carriers in a macroscopic sample.

2.4.2 THz response to excitons

Electrons and holes in photo-excited semiconductors are not always present as free carriers. In some cases, they form bound electron-hole pairs that are referred to as excitons. There can be different reasons for the formation of excitons instead of free carriers. In low dielectric function materials, charge screening is relatively weak and the Coulombic attraction energy can be higher than the thermal energies of electrons and holes, especially at low temperatures. The low-temperature formation of excitons in materials like silicon and GaAs has been studied extensively with THz-TDS[11,26-28].

More relevant within the scope of this thesis is the existence of excitons in nanostructured materials like quantum dots. As explained in chapter 1, the dominating contribution to the exciton energy comes from the confinement energy, rather than from Coulombic attractions. Because of quantum-confinement, excitons are formed in QDs also at room temperature and their response to THz radiation is similar to that of excitons in bulk materials at low temperature. In contrast to free carriers, an electron (hole) within the exciton cannot be displaced significantly by an applied THz field, because the oppositely charged hole (electron) provides a restoring force by means of Coulombic attraction. As a result, the characteristic exciton resonance is different from the free carrier Drude response (resonance positioned at zero frequency). Rather, the excitonic resonance originates from intraband transitions of holes and electrons (see Fig. 1.1). The energy associated with these resonances is determined by the spacing between the energy levels: the relative position of these energy levels (and hence the associated spacing between the levels) is determined by the QD radius and the carrier effective masses (see Eq. 1.3). Fig. 2.7(a) shows a schematical representation of the conductivity of the lowest-energetic intraband transition. In most materials, the effective mass of holes is significantly larger than that of electrons[29], resulting in typical energy spacings between valence levels of 40-100 meV and spacings between conduction levels of 300-600 meV[30,31]. Since the spectrum of our THz probe lies between ~ 0.2 – 2 THz (~ 1–8 meV), the energy of the THz probe is insufficient to excite intraband transitions in QDs directly. Therefore, the THz light is not absorbed by excitons in QDs (no real photoconductivity), but the THz pulse experiences a phase-shift as a result of the polarization of excitonic wavefunctions. THz data of InAs QDs after excitation with 800 nm light in Fig. 2.7(b) is in agreement with the expected excitonic THz response. Clearly,
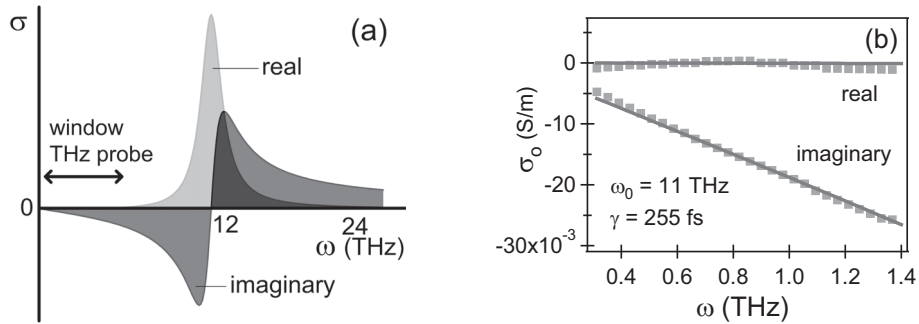
Figure 2.7 THz conductivity for excitons. (a) Schematic of the lowest-energetic excitonic resonance, which is positioned at finite frequency (in contrast to the zero frequency Drude conductivity). The interaction of THz light with excitons originates from intraband electronic transitions. (b) Conductivity of 4.4 nm InAs QDs (grey dots) in the frequency window of the THz spectrometer, after excitation with 800 nm light. The real conductivity is zero (no absorption) and the imaginary conductivity is negative and decreasing with frequency, in agreement with the theoretical excitonic conductivity depicted in (a). The solid line in (b) is a fit of the data with equation 2.21.

the real conductivity is zero and the imaginary conductivity is negative and decreasing with frequency, corresponding to the photo-induced phase shift of the THz pulse.

To describe the THz response in Fig. 2.7(b) quantitatively, the QDs can be treated as polarizable spheres on a macroscopic and a microscopic level. For a macroscopic sample, the total electric dipole moment P is given by[32]:

$$P = \chi E \tag{2.13}$$

where E is the external electric field and χ is the dielectric susceptibility, which is related to the dielectric constant by $\varepsilon = 1 + 4\pi\chi$. In a microscopic description, the polarization induced in a single QD is a result of the *internal* electric field, E', which is different from the *external* electric field because of the dielectric screening of the field by the QD. The internal electric field inside the (spherical) particle is given by[32]:

$$E' = E + \frac{4\pi}{3} P \tag{2.14}$$

For a single QD, the electric dipole moment p is defined as:

$$p = \alpha \cdot E' \tag{2.15}$$

where α is the polarizability of the QD. The microscopic dipole moment p is connected to the macroscopic total dipole moment P by:

$$P = N \cdot p = N \cdot \alpha \cdot E' \tag{2.16}$$

On eliminating E' from the above equations, one finds the Lorentz-Lorenz formula that relates the microscopic polarizability α with the macroscopic dielectric constant ε:

$$\alpha = \frac{3}{4\pi N} \frac{\varepsilon - 1}{\varepsilon + 2} = R^3 \frac{\varepsilon - 1}{\varepsilon + 2} \tag{2.17}$$

The polarizability α of an *excited* QD consists of a contribution from valence electrons (reflected by the ground state dielectric constant ε) and a contribution from the polarizable exciton (reflected by the photo-induced change in the dielectric constant $\Delta\varepsilon$). Combining equations 2.1, 2.2, and 2.17, one finds the expression that relates the exciton conductivity σ_0 to the exciton polarizability α_{exc}:

$$\frac{(\varepsilon - 1) + i\sigma_0(\omega)/\omega\varepsilon_0}{(\varepsilon + 2) + i\sigma_0(\omega)/\omega\varepsilon_0} = \frac{\varepsilon - 1}{\varepsilon + 2} + \frac{\alpha_{exc}(\omega) N_{exc}}{3} \tag{2.18}$$

42

where N_{exc} is the exciton density. Analogous to the hydrogen atom, the polarizability of a transition dipole of an intraband resonance is characterized by a Lorentzian lineshape given by[23]:

$$\alpha_{exc}(\omega) = \alpha_{0,exc} \frac{\omega_0^2}{\omega_0^2 - \omega^2 - i\gamma\omega} \qquad (2.19)$$

where α_0 is the static (DC) polarizability associated with of a specific intraband transition, ω_0 is the intraband transition energy defined by the spacing between energy levels, and γ is the linewidth of the absorption. Rearranging equation 2.18 gives the expression that defines σ_0 as a function of α_{exc}:

$$\sigma_0(\omega) = \frac{-i\omega\varepsilon_0(\varepsilon+2)^2 \alpha_{exc}(\omega)N}{(9 - (\varepsilon+2)\alpha_{exc}(\omega)N)} \qquad (2.20)$$

Typically, $\alpha_{exc}N < 1$ and equation 2.20 can be reduced to

$$\sigma_0(\omega) = -(1/9)i\omega\varepsilon_0(\varepsilon+2)^2 \alpha_{exc}(\omega)N \qquad (2.21)$$

Fitting the data in Fig 2.7(b) with equation 2.21 yields ω_0 and γ. In the fitting procedure, a value for α_0 of 15.000 Å^3 was used, which was determined from THz-TDS measurements in Chapter 3. In this thesis, the excitonic response at THz frequencies was used to investigate exciton dynamics in colloidal QDs (see Chapters 3 and 4).

2.4.3 THz response to nanostructured semiconductors

Nanocrystalline semiconductor films are widely used in dye-sensitized solar cells, because of the large surface area per unit volume[33]. Most commonly, the films are $1 - 10$ μm thick and consist of sintered TiO_2 particles of $10 - 50$ nm size. Such TiO_2 films are also candidates as supporting material for QD-sensitized solar cells, as explained in paragraph 1.5. The THz response of carriers within TiO_2 nano-films is vastly different from bulk semiconductors[16,23,34,35], even though the constituent TiO_2 particles have bulk properties since their size is much larger than the exciton Bohr radius of TiO_2 (~ 1 nm). The reason is the large dielectric contrast between nano-particles and the surrounding medium, typically air or an organic solvent. Microscopically, the applied electric field that causes acceleration of free carriers is screened by the highly polarizable TiO_2 particles ($\varepsilon_p \sim 120$)[23]. As a result, the internal electric field is reduced compared to the field experienced in a homogeneous sample of the bulk material.

To calculate the conductivity of nanocrystalline films, it is necessary to define an effective dielectric function for a material consisting of two phases (e.g. TiO_2 and air). A commonly used approach is the Maxwell-Garnett effective medium theory[23,36] that relates

the dielectric function of the polarizable particles, ε_p, and of the surrounding medium, ε_m, to the *effective* dielectric function ε of the composite by:

$$\frac{\varepsilon - \varepsilon_m}{\varepsilon + 2\varepsilon_m} = f \frac{\varepsilon_p - \varepsilon_m}{\varepsilon_p + 2\varepsilon_m} \qquad (2.22)$$

where f is the filling fraction of the polarizable particles. For example, a film of TiO_2 particles ($\varepsilon_p = 120$)[23] in air ($\varepsilon_p = 1$) with $f = 0.4$ results in $\varepsilon = 2.9$ according to equation 2.21. The photo-conductivity of carriers in a nanoporous medium can be obtained by combining the Drude model ($\sigma = -i\omega\varepsilon_0\varepsilon$) with equation 2.22:

$$\frac{\varepsilon + i\sigma/\omega\varepsilon_0 - \varepsilon_m}{\varepsilon + i\sigma/\omega\varepsilon_0 + 2\varepsilon_m} = f \frac{\varepsilon_p + i\sigma_p/\omega\varepsilon_0 - \varepsilon_m}{\varepsilon_p + i\sigma_p/\omega\varepsilon_0 + 2\varepsilon_m} \qquad (2.23)$$

Figure 2.8(b) gives the complex conductivity of a 2 μm nanocrystalline TiO_2 film in air. The film consists of sintered anatase TiO_2 particles of 15 nm in diameter (see Fig. 2.8(a) for a scanning electron microscope image) and is directly excited with 266 nm pulses. The solid line in Fig. 2.8 is a fit to the Maxwell-Garnett effective medium theory (equation 2.23). Clearly, the combination of the Drude equation with effective medium theory is consistent with two characteristic features of the conductivity in nanocrystalline semiconductors, i.e. the fact that the conductivity becomes zero for $\omega \rightarrow 0$ and the fact that the imaginary conductivity is negative. Both features are inconsistent with the 'normal' Drude model, but can be accounted for by incorporating local field effects.
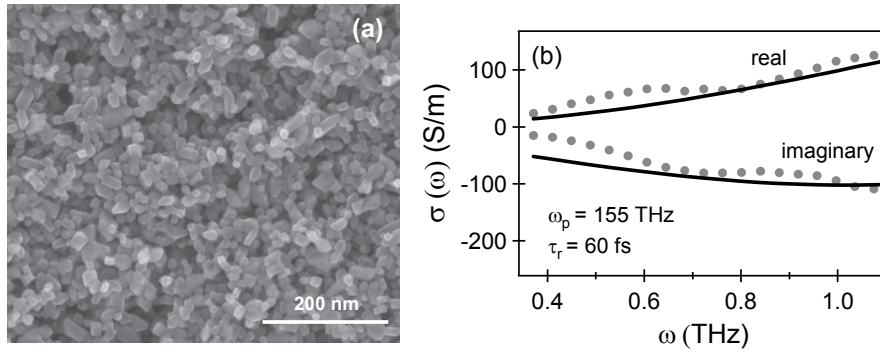

Figure 2.8 (a) SEM image of a nanostructured TiO_2 film. (b) THz conductivity of a nanostructured TiO_2 film (grey dots), measured after direct excitation with 266 nm light. The solid line is a fit to the Maxwell-Garnett effective medium theory (see text).

2.5 Transient Absorption

Transient Absorption (TA) is one of the most common techniques for the investigation of ultrafast excited state dynamics in QDs[37-40] and dyes[41]. Like THz-TDS, it is a pump-probe technique using ultrashort pulses of ~ 50 – 150 fs. The main difference with THz-TDS is that TA makes use of a probe pulse of visible or infrared (IR) frequencies. While a probe at THz frequencies is ideally suited for investigating the carrier mobility and conductivity in (nano-structured) semiconductors via the complex refractive index, TA gives information on the dynamics of electronic and vibrational excitations by tuning the probe light to the transition of interest in for instance molecules and QDs. In this thesis, TA is used to obtain information about the population of electronic excitations in QDs. The choice between visible and IR probe light is dictated by the QD material: CdSe QDs have interband transitions at visible frequencies[42], whereas the transitions in InAs[43] and PbSe[44] QDs are located in the IR region (see chapter 3 and 6).

In a typical TA experiment, a QD sample is irradiated with a visible pump pulse resulting in photo-excitation of electrons into 'conduction' energy levels (see Fig. 1.1). Subsequently, a probe pulse is transmitted through the sample having a photon energy equal to the interband transition. QDs in the excited state absorb less probe light compared to unexcited QDs, since fewer electronic transitions are available due to the population of electrons in conduction levels. Measuring the difference in absorption of the probe light between the excited and unexcited sample, $\Delta\alpha$, gives information about the population of QDs in the excited state. As in THz-TDS, the dynamics of the excited state population can be detected on a picosecond timescale by varying the delay between the pump and the probe pulse.

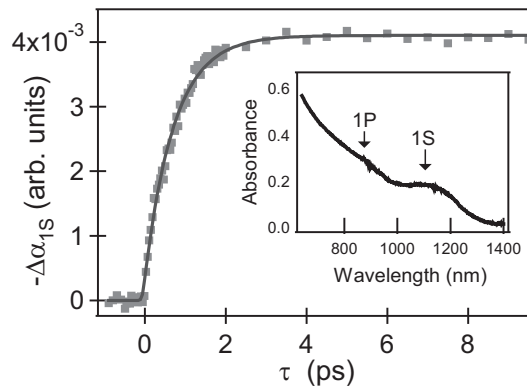**Figure 2.9** Dynamics of a TA measurement on 4.4 nm InAs QDs. The dynamics were determined using a pump intensity of 1.1 $\mu J/mm^2$ (excitation at 800 nm). The inset shows the absorption spectrum for 4.4 nm core-shell InAs QDs. The $1S_e$ population was probed with 1200 nm light to ensure that only dynamics of the 1S transition (positioned at 1100 nm) are probed.

Typical TA data is shown in Fig. 2.9. An experiment was performed where 4.4 nm core-shell InAs QDs were excited with 800 nm pulses and the population of electrons in the $1S_e$ level was probed with 1200 nm light. The bandgap of 4.4 nm InAs QDs is positioned at 1100 nm (1.13 eV, see inset Fig. 2.9) and by probing at 1200 nm we ensure that only the dynamics of the 1S transition, and not the higher-lying 1P transition, are probed. In the experiment presented in Fig. 2.9, the 800 nm excitation fluence is chosen sufficiently low that no more than one exciton per quantum dot is generated. Absorption of an 800 nm photon will excite electrons into hot conduction levels. The initial rise of the signal in Fig. 2.9 can be attributed to relaxation of hot electrons to the $1S_e$ level, with a time constant of ~ 0.8 ps, as obtained from fitting the data with a two-level model (solid line, see Chapter 3 for details fitting procedure).

The schematic layout of the TA setup is given in Figure 2.10. Similar to the THz spectrometer, the TA setup is based on ultrashort 800 nm pulses with a pulse duration of ~ 110 fs FWHM and a repetition rate of 1 KHz. Part of this beam is used to pump the sample with 400 or 800 nm pulses and the remainder is used to generate the probe light. For InAs or PbSe QDs, the probe light is tuned to the QD bandgap at IR frequencies by an Optical Parametric Amplifier (OPA, Coherent). CdSe QDs are probed with a white light continuum that is generated by irradiating a sapphire plate with 400 nm pulses. The transmitted probe light through the sample is spectrally dispersed by a grating and detected on a diode array. In a TA experiment, only the intensity of the probe light is detected and not the phase, which is a major difference with THz-TDS.
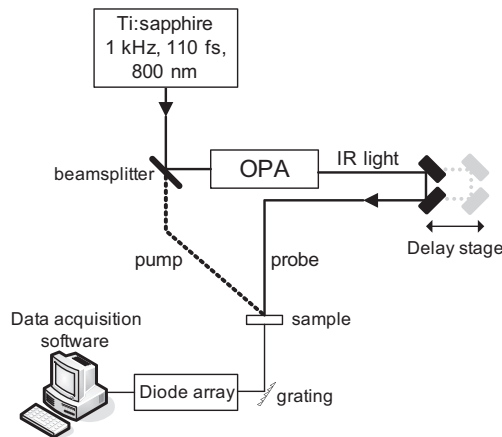
Figure 2.10 Schematic layout of the TA setup. The sample is excited with a pump pulse of visible frequencies (400 or 800 nm) and subsequently probed with visible or IR light pulses, depending on the QD material. The IR light is tuned to the QD bandgap by an Optical Parametric Amplifier (OPA, Coherent). When probing at visible frequencies, a white light continuum is made by pumping a sapphire plate with 400 nm pulses (not shown in figure). The transmitted probe light is spectrally separated by a grating and subsequently detected on a diode array.

References

(1)   Fattinger, C.; Grischkowsky, D. *Appl. Phys. Lett.* **1989**, *54*, 490-492.
(2)   van Exter, M.; Fattinger, C.; Grischkowsky, D. *Appl. Phys. Lett.* **1989**, *55*, 337-339.
(3)   Dexheimer, S. L. *Terahertz Spectroscopy: Principles and Applications*; CRC Press: Boca Raton, 2007.
(4)   Zhang, X. C.; Jin, Y.; Ma, X. F. *Appl. Phys. Lett.* **1992**, *61*, 2764-2766.
(5)   Keiding, S. R. *J. Phys. Chem. A* **1997**, *101*, 5250-5254.
(6)   Knoesel, E.; Bonn, M.; Shan, J.; Wang, F.; Heinz, T. F. *J. Chem. Phys.* **2004**, *121*, 394-404.
(7)   Knoesel, E.; Bonn, M.; Shan, J.; Heinz, T. F. *Phys. Rev. Lett.* **2001**, *86*, 340.
(8)   Markelz, A. G.; Roitberg, A.; Heilweil, E. J. *Chem. Phys. Lett.* **2000**, *320*, 42-48.
(9)   Jeon, T.-I.; Grischkowsky, D. *Phys. Rev. Lett.* **1997**, *78*, 1106.
(10)   Huber, R.; Tauser, F.; Brodschelm, A.; Bichler, M.; Abstreiter, G.; Leitenstorfer, A. *Nature* **2001**, *414*, 286-289.
(11)   Kaindl, R. A.; Carnahan, M. A.; Hagele, D.; Lovenich, R.; Chemla, D. S. *Nature* **2003**, *423*, 734-738.
(12)   Jeon, T.-I.; Grischkowsky, D.; Mukherjee, A. K.; Menon, R. *Appl. Phys. Lett* **2000**, *77*, 2452-2454.
(13)   Hendry, E.; Schins, J. M.; Candeias, L. P.; Siebbeles, L. D. A.; Bonn, M. *Phys. Rev. Lett.* **2004**, *92*.
(14)   Averitt, R. D.; Lobad, A. I.; Kwon, C.; Trugman, S. A.; Thorsmølle, V. K.; Taylor, A. J. *Phys. Rev. Lett.* **2001**, *87*, 017401.
(15)   Pijpers, J. J. H.; Hendry, E.; Milder, M. T. W.; Fanciulli, R.; Savolainen, J.; Herek, J. L.; Vanmaekelbergh, D.; Ruhman, S.; Mocatta, D.; Oron, D.; Aharoni, A.; Banin, U.; Bonn, M. *J. Phys. Chem. C* **2007**, *111*, 4146-4152.
(16)   Hendry, E.; Koeberg, M.; O'Regan, B.; Bonn, M. *Nano Lett.* **2006**, *6*, 755-759.
(17)   Beard, M. C.; Turner, G. M.; Schmuttenmaer, C. A. *Nano Lett.* **2002**, *2*, 983-987.
(18)   Hendry, E.; Koeberg, M.; Wang, F.; Zhang, H.; Donega, C. d. M.; Vanmaekelbergh, D.; Bonn, M. *Phys. Rev. Lett.* **2006**, *96*, 057408-057404.
(19)   Exter, M. v.; Fattinger, C.; Grischkowsky, D. *Optics Letters* **1989**, *14*, 1128-1130.
(20)   Planken, P. C. M.; Nienhuys, H.-K.; Bakker, H. J.; Wenckebach, T. *J. Opt. Soc. Am. B* **2001**, *18*, 313-317.
(21)   Jepsen, P. U.; Schairer, W.; Libon, I. H.; Lemmer, U.; Hecker, N. E.; Birkholz, M.; Lips, K.; Schall, M. *Phys. Rev. Lett.* **2001**, *79*, 1291-1293.
(22)   Hecht, E. *Optics*, 4th ed.; Addison-Wesley: Reading, 2002.
(23)   Hendry, E. Charge Dynamics in Novel Semiconductors, University of Amsterdam, 2005.
(24)   Hook, J. R.; Hall, H. E. *Solid State Physics*; John Wiley & Sons: Chichester, 2004.
(25)   Hendry, E.; Koeberg, M.; Pijpers, J.; Bonn, M. *Phys. Rev. B* **2007**, *75*, 233202.
(26)   Koch, S. W.; Kira, M.; Khitrova, G.; Gibbs, H. M. *Nature Mater.* **2006**, *5*, 523-531.
(27)   Hendry, E.; Koeberg, M.; Bonn, M. *Phys. Rev. B* **2007**, *76*, 6.
(28)   Suzuki, T.; Shimano, R. *Phys. Rev. Lett.* **2009**, *103*, 057401-057404.
(29)   Madelung, O. *Semiconductors: Data Handbook*, 3rd ed.; Springer Verlag: New York, 2003; Vol. 17.
(30)   Norris, D. J.; Bawendi, M. G. *Phys. Rev. B* **1996**, *53*, 16338-16346.
(31)   Banin, U.; Cao, Y. W.; Katz, D.; Millo, O. *Nature* **1999**, *400*, 542-544.
(32)   Born, M.; Wolf, E. *Principles of Optics*, Second ed.; Pergamon Press: Oxford, 1964.
(33)   Grätzel, M. *Progress in Photovoltaics: Research and Applications* **2006**, *14*, 429-442.
(34)   Turner, G. M.; Beard, M. C.; Schmuttenmaer, C. A. *J. Phys. Chem. B* **2002**, *106*, 11716-11719.
(35)   Nienhuys, H. K.; Sundstrom, V. *Phys. Rev. Lett.* **2005**, *87*.

(36)   Bohren, C. F.; Huffman, D. R. *Absorption and scattering of light by small particles*; John Wiley & Sons: New York, 1983.
(37)   Klimov, V. I.; McBranch, D. W. *Phys. Rev. Lett.* **1998**, *80*, 4028-4031.
(38)   Guyot-Sionnest, P.; Shim, M.; Matranga, C.; Hines, M. *Phys. Rev. B* **1999**, *60*, R2181-R2184.
(39)   Klimov, V. I.; Mikhailovsky, A. A.; McBranch, D. W.; Leatherdale, C. A.; Bawendi, M. G. *Science* **2000**, *287*, 1011-1013.
(40)   Schaller, R. D.; Klimov, V. I *Phys. Rev. Lett.* **2004**, *92*.
(41)   Haque, S. A.; Palomares, E.; Cho, B. M.; Green, A. N. M.; Hirata, N.; Klug, D. R.; Durrant, J. R. *J. Am. Chem. Soc.* **2005**, *127*, 3456-3462.
(42)   Murray, C. B.; Norris, D. J.; Bawendi, M. G. *J. Am. Chem. Soc.* **1993**, *115*, 8706-8715.
(43)   Guzelian, A. A.; Banin, U.; Kadavanich, A. V.; Peng, X.; Alivisatos, A. P. *Appl. Phys. Lett.* **1996**, *69*, 1432-1434.
(44)   Koole, R.; Allan, G.; C., D.; A., M.; Vanmaekelbergh, D.; Houtepen, A. J. *Small* **2008**, *4*, 127-133.

Chapter 3: Intraband relaxation in QDs

3.1 Background

Colloidal quantum dots absorbing and emitting in the infrared (IR QDs) have received much attention over the past decade[1]. One reason is that IR QDs have interesting properties for the optical telecommunication market, where most IR components operate at wavelengths ranging from 1200-1600 nm. Since the emission of IR QDs can be easily controlled over this spectral range by varying the particle diameter, QDs can be used for optical switching, wavelength change or optical amplification outside the conventional erbium-doped-fiber amplifier window[1,2]. Another promising application is the use of IR QDs as fluorescent biological labels. Since human tissue absorbs little light in the near infrared region (NIR, 650-900 nm) and since few stable NIR-emitting dye molecules exist, NIR QDs are promising probes for *in vivo* imaging because their bandgap can be easily tuned to the 650-900 nm range[3,4]. Within the scope of this thesis, IR QDs are particularly interesting for use in QD solar cells[5-7]. In contrast to silicon solar cells, IR QD sensitizers can absorb IR light, which makes up approximately 20% of the total energy of the solar spectrum[8]. Furthermore, the excess energy of visible photons can potentially be harvested when using IR QDs as light absorbers by extracting hot carriers from the QDs or by generation of additional carriers via the CM process (see section 1.5).

When utilizing QDs as light absorbing material in solar cells, it is important to understand the interaction between light and QDs, and the dynamics of photogenerated carriers. Using terahertz time-domain spectroscopy (THz-TDS), we study these topics in colloidal InAs QDs (having a tunable energy gap between 600 and 1600nm). First, it is discussed in section 3.3 how confined excitons in QDs respond to an externally applied THz DC electric field. For this purpose, we determine the exciton polarizability (α_{exc}) as a function of QD size. The experimentally obtained values for the polarizability α_{exc} agree well with theoretically predicted values, as obtained from perturbative multi-band tight binding calculations.

Next, we combine THz-TDS with femtosecond transient absorption (TA) to study electron and hole intraband relaxation. In bulk semiconductors, the conduction and valence band consists of densely spaced energy levels and relaxation of 'hot' carriers occurs via sequential emission of longitudinal optical (LO) phonons. In the case of InAs QDs, the energy difference between the $1S_e$ and $1P_e$ level ranges from ~ 300 meV (6.0 nm diameter QDs) to ~ 550 meV (3.0 nm diameter QDs)[9], much larger than typical LO phonon energies (~ 30 meV). Intraband relaxation in CdSe and InP QDs, materials with similar material

characteristics as InAs, takes place via an Auger-process, in which the excess energy of the 'hot' electron is transferred to a 'cold' hole[10-12]. The resulting hot hole can subsequently relax via phonon emission since the energy difference between valence levels is of the order of typical LO phonon energies. In section 3.4, we use TA to probe the population of electrons in the $1S_e$ QD level, giving information about intraband electron dynamics between conduction energy levels. THz-TDS is complementary to TA in the sense that the THz response originates predominantly from the polarizability of holes in the $1S_{3/2}$ energy level, giving information on the intraband hole dynamics between valence energy levels. As such, the combination of TA and THz-TDS is excellently suited to investigate the dynamics of (Auger) electron intraband relaxation from the $1P_e \rightarrow 1S_e$ level. An understanding of this relaxation process is particularly important for the 'hot carrier' solar cell concept (see section 1.5), in which it is essential that the extraction of hot carriers is faster than intraband relaxation.

3.2 Samples: InAs QDs

Colloidal InAs QDs were synthesized as reported elsewhere[13,14]. The QDs for the polarizability experiments were trioctylphospine (TOP) passivated (4.0 nm diameter) or passivated with CdSe/ZnSe-shells (4.9 nm and 5.45 nm diameter InAs cores). These core/shell QDs consist of InAs cores onto which one atomic layer of CdSe and four layers of ZnSe are deposited. Samples are prepared by suspending the QDs in toluene in a 1 mm path length cuvet. The absorption and emission spectra of InAs cores and InAs core-shell QDs, respectively, are shown in Fig. 3.1. For both passivation methods, the absorption spectra and luminescence spectra are broadened inhomogeneously by the size distribution of the sample. The absorption spectrum of 4.9 nm InAs cores in Fig. 3.1(a) exhibits a clear 1S exciton transition at 1120 nm and the 1P transition can be identified by the shoulder at 830 nm. At shorter wavelengths, the absorption spectrum is characterized by the convolved spectra of high-energy transitions. The center of the luminescence spectrum (grey line) is slightly redshifted with respect to 1S absorption peak. The features in the luminescence spectrum around 1145 nm and 1200 nm are due to absorption by the solvent toluene, caused by secondary stretching overtones of methyl and aromatic C-H groups. For TOP-capped InAs QDs, the luminescence quantum yield is relatively low because of quenching via non-radiative decay channels[13]. As can be seen in Fig. 3.1(b), the main features in the absorption spectrum are preserved after addition of the passivating CdSe/ZnSe-shells. The 1S and 1P transitions are less distinct compared to InAs cores, because the size distribution of the QDs becomes broader upon adding multiple shells around the cores. The core/shell structure leads to a significantly improved quantum yield (50 -70%) as compared of the TOP-

passivated QDs (1 - 2.5%)[14]. This increase in fluorescence efficiency is caused by the effective removal of surface defects, leading to reduced losses associated with non-radiative decay channels. The redshift of the luminescence in the core-shell dots can be explained by the low potential barrier imposed by the CdSe shell on the InAs core[14]. As a result, the electron wavefunction leaks into the surrounding shell, effectively weakening the confinement.
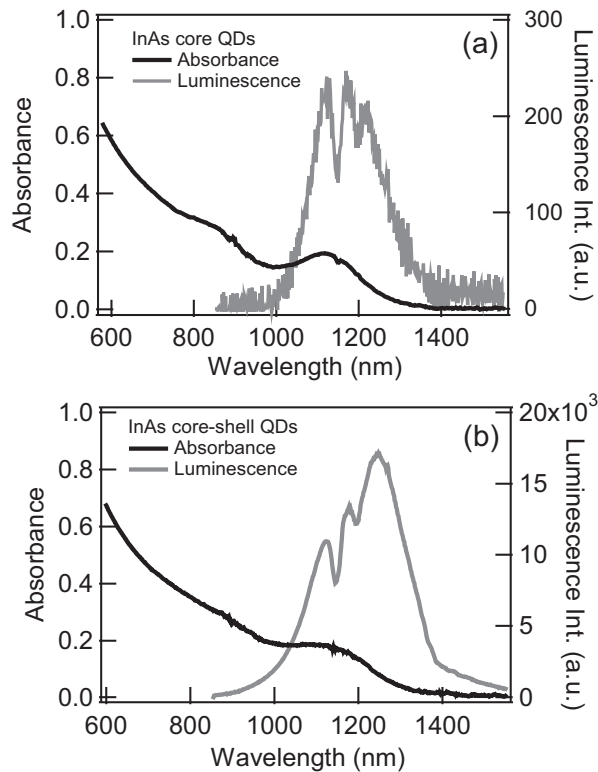
Figure 3.1 Absorption and luminescence spectra of 4.9 nm InAs cores (a) and InAs core-shell QDs (b). The core-shell QDs consist of a 4.9 nm InAs onto which one atomic layer of CdSe and four layers of ZnSe are deposited. The features in the luminescence spectrum around 1145 nm and 1200 nm are due to absorption by the solvent toluene

For the intraband relaxation experiments, TOP-passivated InAs cores are used (2.5 or 4.4 nm diameter), since it was difficult to synthesize small core-shell QDs with good size distribution.

3.3 Exciton polarizability

In this section, the response of quantum-confined excitons to an external electric field is discussed. For QDs with sufficiently strong confinement, the energies associated with (intra-)excitonic transitions are higher than typical THz photon energies. As such, the polarizability at THz frequencies equals the DC polarizability, which is an important parameter describing the QD response to an externally applied field. This response is usually parametrized as the exciton polarizability and has previously been inferred from Stark shift measurements for CdSe QDs[15-17]. Recently, THz-TDS has been successfully applied to determine the exciton polarizability in CdSe[18] and PbSe[19] QDs. The advantage of using THz-TDS is that it is a more direct determination of the polarizability, since the interaction of a THz electric field with a polarizable exciton is directly determined, in contrast to the more indirect procedure of the Stark shift measurements where the shift of the emission wavelength as a function of the applied electric field is recorded. When measuring carrier dynamics in photo-excited QDs using THz-TDS, the THz response is based on the exciton polarizability. Since we will extensively use THz-TDS for probing carrier dynamics in QDs in section 3.4 and chapter 4, it is important to have a detailed understanding of the behavior of the exciton polarizability in InAs QDs.

To determine the exciton polarizability, we first measure the electric field waveform $E_{THz}(t)$ through the unexcited sample. Next, the modulation in the THz waveform, $\Delta E_{THz}(t)$, is recorded by chopping the 800 nm excitation pulse and monitoring the differential THz
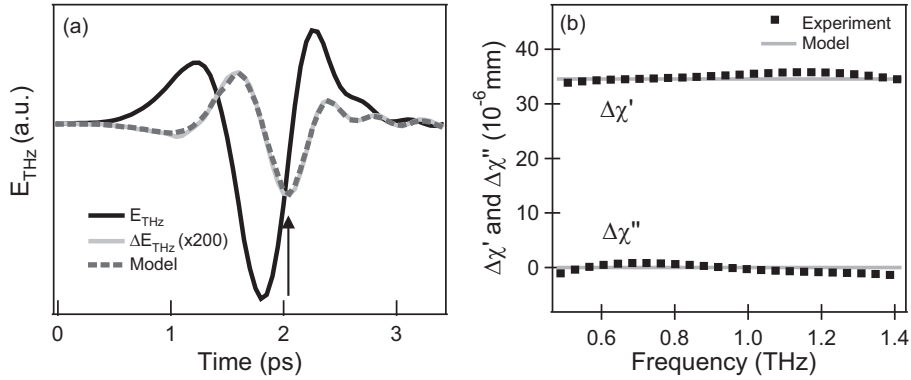
Figure 3.2. a) Transmitted THz pulse $E_{THz}(t, \tau)$ and the exciton-induced modulation thereof, $\Delta E_{THz}(t, \tau)$ for 5.45 nm InAs QDs. For monitoring the transient hole population, $\Delta E_{THz}(t, \tau)$ is measured at the point marked with an arrow (at $t = 2.0$ ps), as a function of τ. The dashed line corresponds to a model in which only the real part of the susceptibility is finite, with a frequency-independent value. b) Change in the real ($\Delta\chi'$) and imaginary ($\Delta\chi''$) part of the photo-induced sheet susceptibility of the QD dispersion. The black dots are obtained from the data in a) and the grey line represents a purely real, frequency-independent change in the susceptibility.

signal. $\Delta E_{THz}(t)$ is measured at a pump-probe delay τ of 20 ps in order to ensure that all excitons were in the ground state. Furthermore, low excitation fluences are used (< 2 μJ/mm^2 for the smallest QDs) to avoid the generation of multi-excitons by sequential-photon absorption. Fig. 3.2(a) shows $E_{THz}(t)$ and $\Delta E_{THz}(t)$ for the 5.45 nm InAs QDs. From the time-domain THz traces in Fig. 3.2(a), the photo-induced change of the complex sheet susceptibility of the sample, $\Delta\chi_{s}$, is obtained, which is defined as the change in the dipole moment per unit area divided by the THz electric field strength[18]. Following the procedure of reference [18], $\Delta\chi_s$ is related to the relevant waveforms in the frequency domain as follows:

$$\frac{\Delta E(\omega)}{E(\omega)} = i\frac{2\pi\omega}{c}\frac{\Delta\chi_s(\omega)}{\sqrt{\varepsilon}} \tag{3.1}$$

where c is the speed of light, ω is the angular frequency of the THz field, and ε is the dielectric constant of the unexcited QD solution. Fig. 3.2(b) shows the resulting complex sheet susceptibility $\Delta\chi_s(\omega) = \Delta\chi_s^{'}(\omega) + i\Delta\chi_s^{''}(\omega)$ as derived from the THz waveforms from Fig. 3.2(a) and equation (3.1). In the limit of dilute QD suspensions, the pump-induced macroscopic sheet susceptibility can be related to the polarizability α of individual quantum-confined excitons via effective medium theory[18]:

$$\Delta\chi_s = n_s \frac{9\varepsilon^2}{(\varepsilon_{InAs} + 2\varepsilon)^2}\alpha_{exc} \tag{3.2}$$

In this equation, $\varepsilon = 2.25$ is the dielectric constant of the QD solution, $\varepsilon_{InAs} \sim 12.4$ is the dielectric constant of unexcited InAs[20] and n_s is the sheet excitation density (number of absorbed photons per unit area). The exciton polarizability can also be retrieved from the complex conductivity, as explained in section 2.4.2, since the slope of the negative imaginary conductivity (see Fig. 3.3(a)) is proportional to the α_{exc} (see equation 2.20).

Fig. 3.3(b) shows α_{exc} as a function of the QD radius (open spheres). The values for the polarizability are of the order of ~ 10.000 Å^3, similar to values found for CdSe QDs[18,19], but larger than for PbSe QDs[19], which is in agreement with expectation; qualitatively, the magnitude of the DC polarizability in QDs is determined by two factors: the dielectric function, responsible for screening of the electric field, and the effective carrier masses, the magnitude of which is determining the exciton transition energies[19]. Both factors differentiate PbSe from CdSe and InAs: First, the dielectric constants of CdSe ($\varepsilon \sim 9.5$) and InAs ($\varepsilon \sim 12.4$) are rather small compared to PbSe ($\varepsilon \sim 215$)[20].
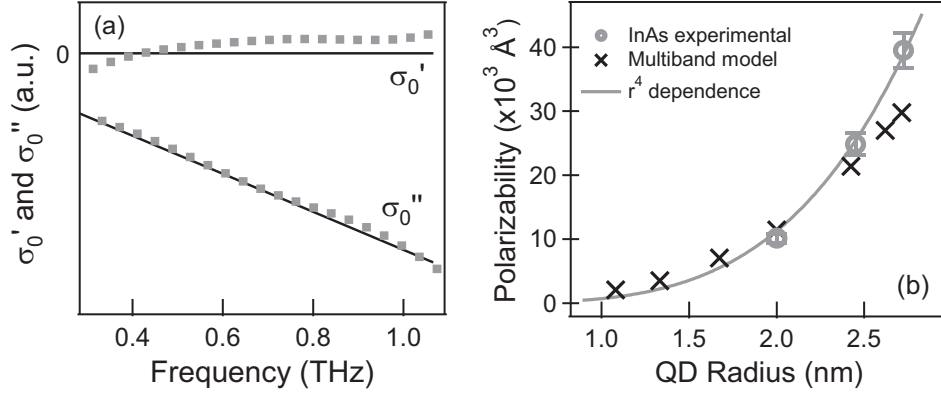
Figure 3.3. a) Complex conductivity of 5.45 nm InAs QDs b) Polarizability of single excitons in photo-excited InAs QDs as a function of the QD radius. The experimental data (open circles) are well-described with a simple R^4 scaling (solid line). The QD polarizability was calculated by perturbative multiband tight binding calculations (black crosses).

Hence, dielectric screening is relatively weak for CdSe and InAs QDs leading to a large exciton response compared to PbSe QDs. Secondly, the effective hole masses of CdSe and InAs are relatively high ($m_h \sim 0.4$)[20], resulting in low intraband hole transition energies, to which our off-resonant THz-probe is more sensitive than to the relatively large intraband transition energies for both electrons and holes in PbSe QDs (resulting from low effective masses in PbSe, $m_h = m_e = 0.05$)[20].

Based on effective mass arguments, it had been argued previously[18,19] that THz light is more sensitive to holes than to electrons in materials like InAs and CdSe QDs (for which $m_h > m_e$). This prediction has been corroborated recently by quantitative measurements which revealed that the polarizability of electrons is two orders of magnitude lower than the polarizability of excitons (consisting of electrons and holes)[21]. An illustration of the different contributions to the overall exciton polarizability is presented in scheme 3.1. The electron and hole intraband transitions in InAs have energies in the mid- and far-IR window, respectively[9]. The left panel of scheme 3.1 depicts the lowest energy transitions, which correspond to transitions between hole levels in InAs QDs. The energies of the frequency components in the THz probe, as depicted by the light gray box, are much lower than typical energies of the hole transitions. Hence, the THz probe is below-resonant and is only sensitive to photo-induced refraction but experiences no photo-induced changes in absorption. For the QDs under investigation ($R << a_b = 37$ nm), the confinement energy is much larger than the Coulombic attraction, and the electrons and holes can be treated as uncorrelated particles. The polarizability of electrons and holes in a specific energy level can be obtained by summing the contributions of i possible transitions to the polarizability

via the formula in scheme 3.1. The usual expression denoting the contribution of an electronic transition to the ground state polarizability reads[18]:

$$\alpha \sim \frac{|(eR)|^2}{\Delta E} \tag{3.3}$$

where $(e\cdot R)$ is the transition dipole moment of a specific intraband transition and ΔE is the corresponding transition energy. Since the carriers are confined in a volume of size R, the dipole is of the order $e\cdot R$ and the transition energy is $\sim h^2/mR^2$, where h is Planck's constant and m is the carrier mass. Hence, the polarizability follows to a first approximation a $\alpha \sim R^4$ scaling, which is confirmed in Fig. 3.3(b) and in Refs. [18,19].
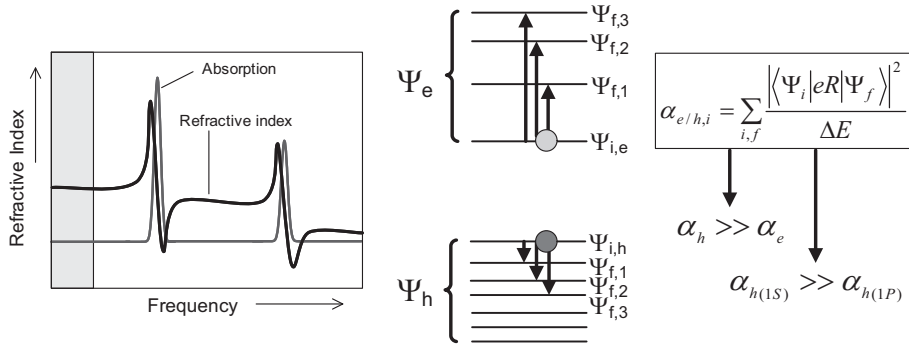
Scheme 3.1 Left panel: position of the THz probe (grey panel) with respect to the lowest intraband transition energies in InAs QDs. The frequency of the THz probe lies below the resonances and the THz response of photo-excited QDs originates only from the photo-induced changes in the refractive index, and not from photo-induced changes in THz absorption. Right panel: treating electrons and holes as uncorrelated particles, the polarizability of an electron or hole in a specific energy level is obtained by summing the values of α_i for i possible transitions.

To characterize the exciton polarizability more quantitatively, detailed calculations were performed by Christophe Delerue of the University of Lille. In these calculations, the electronic structure of InAs QDs is calculated using a tight binding approach as described in Ref. 22. The electronic states Ψ_k are written as linear combinations of s and p atomic orbitals, $\psi_k = \sum_{i,\alpha} c_{k,i\alpha} \varphi_{i,\alpha}$ where $\varphi_{i,\alpha}$ is the αth atomic orbital of atom i at position R_i. In tight binding, the response of a quantum-confined exciton to an external field E_{ext} is determined by the susceptibility matrix which in the uncorrelated-particle approximation and in first order perturbation is given by[23,24].

$$\chi_{ij}^0 = \sum_{k,k'} \frac{(f_k - f_{k'})}{\varepsilon_k - \varepsilon_{k'}} \left(\sum_\alpha c_{k,i\alpha} c_{k',i\alpha}^* \right) \left(\sum_\alpha c_{k,j\alpha} c_{k',j\alpha}^* \right) \tag{3.4}$$

where f_k (= 0,1) and ε_k are the population and the energy of the state Ψ_k, respectively. With equation 3.4 as the starting point, the exciton polarizability was calculated by means of perturbative calculations (black crosses in Fig. 3.3). In this approach, the field E' inside the QD is assumed to be uniform and given by the classical expression $E' = F \cdot E_{ext}$ where $F = 3/(\varepsilon_b + 2)$ is the local field factor. The exciton is polarized by the internal field and the induced dipole is defined by $\mathbf{p}^{exc} = \alpha \mathbf{E}_{in} = -e\sum_i \delta n_i^{exc} \mathbf{R}_i$ where $-e\delta n_i^{exc}$ is the displacement

of the charge on the atom i. In vector-matrix notation, δn^{exc} is equal to $\chi^{eh} V^{in}$ where V^{in} is the potential energy in the field E'. χ^{eh} is given by Eq. (3.4) but the set of states k is restricted to the excitonic electron and hole states. The polarizability is deduced by $\alpha = -e^2 \sum_{i,j} \chi_{ij}^{eh} (\mathbf{R}_i \cdot \mathbf{u})(\mathbf{R}_j \cdot \mathbf{u})$ where u is the unit vector along the electric field. The

perturbative calculations confirm that holes have a much larger polarizability in InAs QDs than electrons, owing to the much smaller energy spacing between valence levels due to the larger effective hole mass. This result is consistent with the previously-mentioned argument that THz-TDS is more sensitive to the population of holes than of electrons in InAs QDs as a result of effective mass arguments. Comparing the polarizability of holes in different valence levels, the $1S_{3/2}$ energy level makes the largest contributions to the overall exciton polarizability. As a result, the THz-TDS signal is proportional to the population of 'cold' holes in the $1S_{3/2}$ level. The results in Fig. 3.3(b) confirm that perturbation calculations correctly predict the polarizability of single excitons, as shown previously for CdSe and PbSe[18,19].

3.4 Intraband relaxation in InAs QDs

In this section, the assessment of intraband relaxation dynamics of hot carriers in InAs QDs is discussed. Knowledge, and ideally control of hot carrier relaxation is a crucial requirement for exploring possibilities for harvesting the excess energy of visible light (see Fig. 1.4) by hot carrier extraction or Carrier Multiplication, as was explained in Chapter 1. Intraband relaxation of hot carriers has been widely studied in CdSe QDs, where an Auger mechanism is usually proposed to explain sub-picosecond relaxation dynamics[10,11,25,26]. In the Auger relaxation process, the hot electron relaxes by transferring its excess energy to a cold hole, which is excited to a hot state. Subsequently, the hot hole will relax via emission of LO phonons, which is possible due to the relatively small energy spacing between hole levels in InAs QDs. Intraband relaxation via an Auger mechanism requires strong overlap between electron and hole wavefunctions. If the hole is trapped at the QD surface, the electronic overlap is reduced and the intraband relaxation of electrons has been reported to

proceed via unoccupied energy levels at the QD surface or via energy transfer to vibrations in the surface-passivating ligands[27].

To quantify carrier cooling dynamics in InAs QDs, THz-TDS measurements are complemented with Transient Absorption (TA) measurements. As explained in the previous section, the THz response in InAs QDs is dominated by holes in the $1S_{3/2}$ level and measuring $\Delta E_{THz}(t,\tau)$ at a time t when $E_{THz}(t) = 0$ [marked by an arrow in Fig. 3.1] for various pump-probe delays gives the transient hole population of the $1S_{3/2}$ level[26]. The risetime of the $\Delta E_{THz}(t,\tau)$ signal contains information about the timescale at which the $1S_{3/2}$ level is populated, yielding information about intraband *hole* dynamics. In principle, TA measurements give information about holes *and* electrons in the ground state, but as a result of the large difference of electron and hole masses in InAs ($m_h/m_e \approx 17$) and the degeneracy of the valence band, the TA signal is dominated by the electron population in the $1S_e$ level[10]. Hence, TA can be used to probe intraband *electron* dynamics. After photoexcitation of the QDs with 50 fs, 800 nm laser pulses, the bleach and the stimulated emission of the lowest energy *inter*-band transition (i.e. the transition between the electron and hole in their respective lowest energy states, described by $\Delta\alpha_{1S}$) are probed with a second 65 fs pulse tuned to the band edge of the QDs under investigation (wavelengths: 950 nm for 2.5 nm QDs and 1200 nm for 4.4 nm QDs) at time τ after photoexcitation.

From the linear absorption spectra and from Scanning Tunneling Microscopy measurements[28], it is known that the 1P energy transition is positioned at ~ 1.9 eV for the 2.5 nm QDs and at ~ 1.4 eV for the 4.4 nm QDs. Hence, absorption of a 800 nm (1.55 eV) photon will generate electrons in the $1P_e$ state for the 4.4 nm particles but this photon energy is insufficient to populate the $1P_e$ level for the 2.5 nm particles, as is schematically depicted in Scheme 3.2.
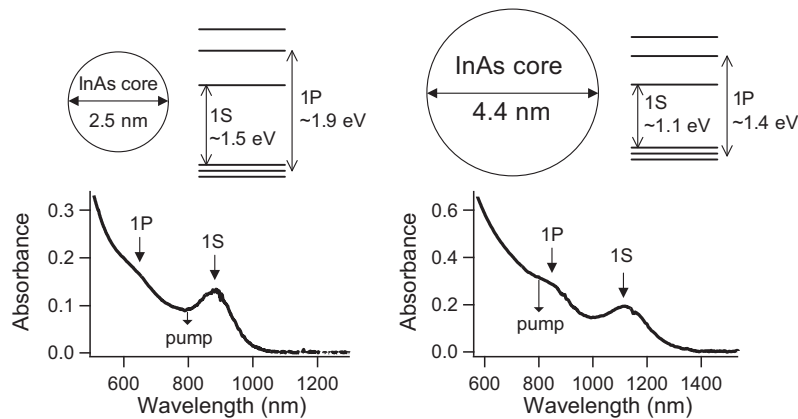
Scheme 3.2 Absorption spectra for the two QD sizes used in the intraband relaxation experiment, combined with a schematic diagram of the QD energy levels and the laser excitation energies.
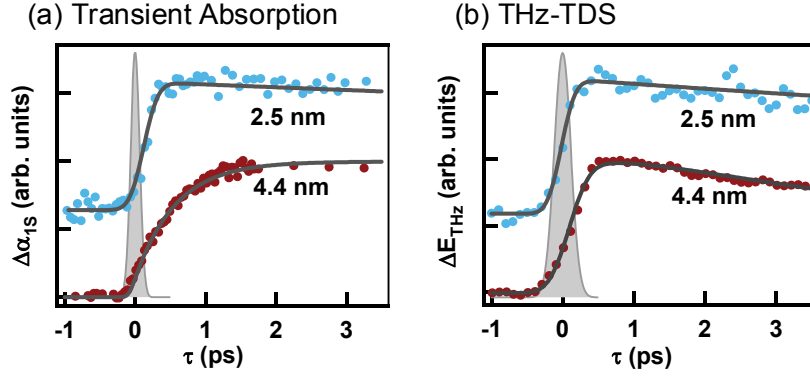
(a) Transient Absorption

(b) THz-TDS

Figure 3.4 (a) Rise dynamics of the TA signal at the gap energy corresponding to 950 nm (2.5 nm QDs) and 1200 nm (4.4 nm QDs). The TA signal reflects the transient electron population of the $1S_e$ level. (b) Dynamics of the rise of $\Delta E_{THz}(t, \tau)$, representing the transient hole population of the $1S_{3/2}$ level. In both measurements, TOP-capped InAs QDs were used. The grey shaded regions correspond to the instrument response functions for the TA and THz experiments.

The results of the TA experiments are shown in Fig. 3.4(a) for 2.5 and 4.4 nm diameter InAs QDs, having a 1S energy transition of 1.4 eV and 1.1 eV, respectively. The fact that for 2.5 nm particles absorption of the 800 nm photon (at $\tau = 0$ ps) results in electrons in the $1S_e$ level, explains the very fast rise of the TA signal for 2.5 nm QDs after excitation; the rise time is limited by the instrument response function (black line through the data), reflecting the instantaneous population of $1S_e$ electrons. However, the rise of the signal is clearly slower for the larger (4.4 nm) QDs. This is indicative of the delayed population of the $1S_e$ level due to intraband relaxation of an electron from the $1P_e$ state. Since the TA signal is proportional to the population of $1S_e$ electrons, the TA signals can be fitted with a two level model (see Scheme 3.3), representing the population of the $1P_e$ and $1S_e$ levels (the fits are the black lines in Fig. 3.4(a)). From the fit of the TA signal of 4.4 nm QDs, the electron relaxation time is found to be ~ 0.8 ps, which is very similar to previous reports on

$$N_{elec}^{hot} \quad\quad\quad \tau_{e\text{-}h} \quad\quad \text{Electron levels} \quad\quad N_{elec}^{cold}$$

$$\frac{dN_{elec}^{hot}}{dt} = -\frac{1}{\tau_{e-h}} N_{elec}^{hot} \quad \left\{ \begin{array}{l} + 0, \ d = 2.5 \ \text{nm} \\ + \delta(t), \ d = 4.4 \text{nm} \end{array} \right.$$

$$\frac{dN_{elec}^{cold}}{dt} = \frac{1}{\tau_{e-h}} N_{elec}^{hot} \quad \left\{ \begin{array}{l} + \delta(t), \ d = 2.5 \ \text{nm} \\ + 0, \ d = 4.4 \text{nm} \end{array} \right.$$

Scheme 3.3 Two-level model used to fit the TA data in Fig. 3.4(a). In the TA experiment, the probe light is sensitive to the population of electrons in the $1S_e$ level ('cold' electrons). The time dependent populations *(N)* of each level are given by two coupled differential equations, in which τ_{eh} is the electron-hole coupling time. The function $\delta(t)$ describes the occupation of the relevant electron state at t_0 using a Gaussian function to describe the temporal profile of the excitation pulse.

relaxation times in CdSe[10,11,26,29] and InP[12] QDs. The observation that intraband electron relaxation occurs on a similar timescale in CdSe, InP, and InAs QDs is consistent with the very similar dielectric constant in these materials (ε = 9.5, 12.5 and 12.4, respectively, resulting in comparable dielectric screening) and the similar energy structure (high m_h, low m_e) for these materials. These two material characteristics favor fast intraband relaxation via an Auger mechanism, since a low dielectric constant leads to stronger (Coulombic) electron-hole interaction and since hot holes (generated by electron-hole energy transfer) can lose their excess energy via sequential phonon emission. PbSe, in contrast, has a high dielectric function (ε = 215) and a different energy structure ($m_h = m_e = 0.05$ for PbSe[20], whereas $m_h \sim 0.4$ for InAs and CdSe). Hence, the material characteristics are less favorable for Auger intraband relaxation process since dielectric screening is high and relaxation of hot holes can not occur via sequential phonon emission. Indeed, it has been reported that intraband relaxation in PbSe QDs occurs via a (temperature-dependent) multi-phonon process[30], which is consistent with the different material properties of PbSe.

The rise of the THz signals, reflecting hole relaxation dynamics in InAs QDs, is shown in Fig. 3.4(b). As explained above, carrier relaxation via an Auger process involves energy transfer from hot electrons to cold holes. As a result, cold holes are excited to higher energy levels and the effective time-constant of hole cooling increases. Hence, it is expected that the rise time of the THz signal (describing the population of cold holes) increases in case of Auger relaxation[26]. Since $m_e << m_h$ in InAs, most of the excess energy of incident 800 nm photons ($\sim$ 0.42 eV for 4.4 nm InAs QDs) will be transferred to the electrons. For the 4.4 nm QDs, an Auger process should lead to a slower rise of the THz signal as compared to the 2.5 nm QDs, due to the emergence of hot holes with 0.42 eV excess energy. Qualitatively, the predicted (Auger-like) behavior of hole cooling was confirmed in our measurements. In Fig. 3.4(b), it can be seen that the rise of the THz signal is slower for the 4.4 nm QDs than for the 2.5 nm QDs, although the difference is rather small. To quantify this effect, we fitted our THz data with a four level model consisting of N_{hole}^{cold}, N_{hole}^{hot}, N_{elec}^{cold}, and N_{elec}^{hot}, which represent the population of hot and cold electrons and holes. This four-level model for Auger intraband relaxation is schematically depicted in Scheme 3.4, together with the coupled differential equations. The function $\delta(t)$ describes the occupation of the relevant electron and hole state at t_0 using a Gaussian function to describe the temporal profile of the excitation pulse.

For the case of the 2.5 nm QDs, the cooling of holes with 0.13 eV excess energy occurs very rapidly and only an upper limit for the corresponding time constant (τ_h) can be determined (<150 fs). In case of the 4.4 nm QDs, the excess energy of the hot holes is larger (0.42 eV, transferred from electrons), giving rise to a small but significant slowing

$$N_{elec}^{hot} \quad\rule{3cm}{0.4pt}\circ\quad$$

$$\tau_{e-h} \downarrow \quad \text{Electron levels}$$

$$N_{elec}^{cold} \quad\rule{3cm}{0.4pt}\quad$$

$$N_{hole}^{cold} \quad\rule{3cm}{0.4pt}\circ\quad$$

$$\tau_h \uparrow \quad \tau_{e-h} \downarrow \quad \text{Hole levels}$$

$$N_{hole}^{hot} \quad\rule{3cm}{0.4pt}\circ\quad$$

$$\frac{dN_{elec}^{hot}}{dt} = -\frac{1}{\tau_{e-h}} N_{elec}^{hot} \quad \begin{cases} + 0, \ d = 2.5 \ nm \\ + \delta(t), \ d = 4.4 nm \end{cases}$$

$$\frac{dN_{elec}^{cold}}{dt} = \frac{1}{\tau_{e-h}} N_{elec}^{hot} \quad \begin{cases} + \delta(t), \ d = 2.5 \ nm \\ + 0, \ d = 4.4 nm \end{cases}$$

$$\frac{dN_{hole}^{hot}}{dt} = -\frac{1}{\tau_h} N_{hole}^{hot} + \frac{1}{\tau_{e-h}} N_{elec}^{hot} + \delta(t)$$

$$\frac{dN_{hole}^{cold}}{dt} = \frac{1}{\tau_h} N_{hole}^{hot} - \frac{1}{\tau_{e-h}} N_{elec}^{hot}$$
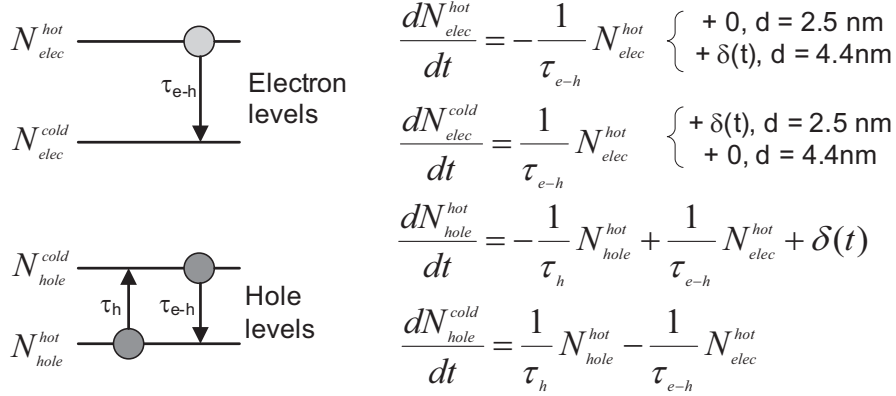
Scheme 3.4 Four-level model for Auger intraband relaxation in QDs. The time dependent populations *(N)* of each level are given by four coupled differential equations, in which τ_h is the hole cooling time, and τ_{eh} is the electron-hole coupling time. The function $\delta(t)$ describes the occupation of the relevant electron and hole state at t_0 using a Gaussian function to describe the temporal profile of the excitation pulse.

down of the hole cooling process. Given the limited time resolution and signal-to-noise of our experiments, again only an upper limit for τ_h can be extracted from the THz data on the 4.4 nm QDs, of ~ 150 fs. Although we are not able to quantify the absolute value of τ_h from either of the two data sets, the data in Fig. 4.3(b) clearly indicate that the THz signal rise time is slower in the larger QDs, which makes the results of the THz-TDS and TA measurements consistent with an Auger mechanism for intraband relaxation of hot electrons in InAs QDs with an electron relaxation time of ~ 0.8 ps.

In absolute terms, the timescale of hole relaxation in InAs QDs (< 150 fs) is at least a factor of two faster than that reported for CdSe QDs[26,29]. However, the energy dissipation rate of hot holes is comparable for both materials, amounting to ~ 1-2 eV/ps, depending on the QD size. Parameters that influence the exact value of the energy dissipation rate of hot holes in InAs and CdSe QDs include the QD size (relative to the exciton Bohr radius), the initial excess energy of the hot hole, and the hole-phonon coupling constant.

3.5 Conclusions

THz-TDS has been used to probe the response of individual quantum-confined excitons to an external electric field. The polarizability of excitons in InAs QDs was found to be of the order of ~ 10.000 Å[3] and increases with the QD radius to the fourth power. These findings are in excellent agreement with previous THz studies on CdSe and PbSe QDs[18,19]. Perturbative calculations confirm the notion that the THz signal is proportional to the

population of holes in the 'cold' $1S_{3/2}$ level and quantitatively reproduce the experimental results. By combining THz-TDS with Transient Absorption, where one probes electrons in the 'cold' $1S_e$ level, dynamics of intraband relaxation from 'hot' to 'cold' levels in QDs has been studied. It was found that relaxation of electrons from the $1P_e$ level to the $1S_e$ level takes place on a sub-picosecond timescale. Our observations are consistent with the currently accepted Auger mechanism for intraband relaxation. All findings reported in this chapter can be qualitatively explained by the low dielectric constant of InAs (resulting in strong carrier-carrier interactions) and the low energy spacing between valence levels (resulting from the relatively high value of the hole effective mass). For application of QDs in solar cells, material properties like the dielectric constant and the carrier effective masses are hence crucial design parameters.

References

(1)   Rogach, A. L.; Eychmuller, A.; Hickey, S. G.; Kershaw, S. V. *Small* **2007**, *3*, 536-557.
(2)   Harrison, M. T.; Kershaw, S. V.; Burt, M. G.; Rogach, A. L.; Kornowski, A.; Eychmuller, A.; Weller, H. *Pure and Applied Chemistry* **2000**, *72*, 295-307.
(3)   Bruchez, M.; Moronne, M.; Gin, P.; Weiss, S.; Alivisatos, A. P. *Science* **1998**, *281*, 2013-2016.
(4)   Zimmer, J. P.; Kim, S. W.; Ohnishi, S.; Tanaka, E.; Frangioni, J. V.; Bawendi, M. G. *J. Am. Chem. Soc.* **2006**, *128*, 2526-2527.
(5)   Yu, P. R.; Zhu, K.; Norman, A. G.; Ferrere, S.; Frank, A. J.; Nozik, A. J. *J. Phys. Chem. B* **2006**, *110*, 25451-25454.
(6)   Cui, D. H.; Xu, J.; Zhu, T.; Paradee, G.; Ashok, S.; Gerhold, M. *Appl. Phys. Lett.* **2006**, *88*, 3.
(7)   Jiang, X. M.; Schaller, R. D.; Lee, S. B.; Pietryga, J. M.; Klimov, V. I.; Zakhidov, A. A. *J. Mater. Res.* **2007**, *22*, 2204-2210.
(8)   Santbergen, R.; van Zolingen, R. J. C. *Solar Energy Materials and Solar Cells* **2008**, *92*, 432-444.
(9)   Banin, U.; Cao, Y. W.; Katz, D.; Millo, O. *Nature* **1999**, *400*, 542-544.
(10)   Klimov, V. I.; McBranch, D. W. *Phys. Rev. Lett.* **1998**, *80*, 4028-4031.
(11)   Guyot-Sionnest, P.; Shim, M.; Matranga, C.; Hines, M. *Phys. Rev. B* **1999**, *60*, R2181-R2184.
(12)   Blackburn, J. L.; Ellingson, R. J.; Micic, O. I.; Nozik, A. J. *J. Phys. Chem. B* **2003**, *107*, 102-109.
(13)   Guzelian, A. A.; Banin, U.; Kadavanich, A. V.; Peng, X.; Alivisatos, A. P. *Appl. Phys. Lett.* **1996**, *69*, 1432-1434.
(14)   Aharoni, A.; Mokari, T.; Popov, I.; Banin, U. *J. Am. Chem. Soc.* **2006**, *128*, 257-264.
(15)   Sacra, A.; Norris, D. J.; Murray, C. B.; Bawendi, M. G. *J. Chem. Phys.* **1995**, *103*, 5236-5245.
(16)   Empedocles, S. A.; Bawendi, M. G. *Science* **1997**, *278*, 2114-2117.
(17)   Seufert, J.; Obert, M.; Scheibner, M.; Gippius, N. A.; Bacher, G.; Forchel, A.; Passow, T.; Leonardi, K.; Hommel, D. *Appl. Phys. Lett.* **2001**, *79*, 1033-1035.

(18)   Wang, F.; Shan, J.; Islam, M. A.; Herman, I. P.; Bonn, M.; Heinz, T. F. *Nature Mater.***2006**, *5*, 861-864.
(19)   Dakovski, G. L.; Lan, S.; Xia, C.; Shan, J. *J.Phys.Chem.C* **2007**, *111*, 5904-5908.
(20)   Madelung, O. *Semiconductors: Data Handbook*, 3rd ed.; Springer Verlag: New York, 2003; Vol. 17.
(21)   Mandal, P. K.; Chikan, V. *Nano Lett.***2007**, *7*, 2521-2528.
(22)   Niquet, Y. M.; Delerue, C.; Allan, G.; Lannoo, M. *Phys.Rev.B* **2002**, *65*, 165334.
(23)   Delerue, C., Lannoo, M. *Nanostructures: Theory and Modelling*; Springer-Verlag: Berlin/Heidelberg/New York, 2004.
(24)   Hedin, L., Lundqvist, S. *Solid State Physics*; Academic: New York, 1969; Vol. 23.
(25)   Klimov, V. I.; McBranch, D. W.; Leatherdale, C. A.; Bawendi, M. G. *Phys.Rev.B* **1999**, *60*, 13740-13749.
(26)   Hendry, E.; Koeberg, M.; Wang, F.; Zhang, H.; Donega, C. d. M.; Vanmaekelbergh, D.; Bonn, M. *Phys.Rev.Lett.***2006**, *96*, 057408-057404.
(27)   Guyot-Sionnest, P.; Wehrenberg, B.; Yu, D. *J.Chem.Phys.***005**, *123*.
(28)   Krapf, D.; Kan, S. H.; Banin, U.; Millo, O.; Sa'ar, A. *Phys.Rev.B* **2004**, *69*, 073301-073304.
(29)   Cooney, R. R.; Sewall, S. L.; Anderson, K. E. H.; Dias, E. A.; Kambhampati, P. *Phys.Rev.Lett.***2007**, *98*, 177403-177404.
(30)   Schaller, R. D.; Pietryga, J. M.; Goupalov, S. V.; Petruska, M. A.; Ivanov, S. A.; Klimov, V. I. *Phys.Rev.Lett.***2005**, *95*, 196401-196404.

Chapter 4: Carrier Multiplication and multi-exciton recombination in InAs QDs

4.1 Background

Over the past decade, colloidal semiconductor quantum dots (QDs) have become available that have large absorption cross sections, and a bright and stable luminescence. These particles cover the visible to near-infrared spectral range and have important potential applications in future solar cells, as explained in Chapter 1. Solar cells rely on the conversion of light into excited electrons and holes (excitons), and knowledge of the processes immediately following photo-excitation is therefore essential for an optimal design of a QD-based solar cell, in addition to the fundamental interest in exciton and charge carrier dynamics in QDs. As such, there has been much interest recently in exciton dynamics in QDs, especially in exciton decay[1], exciton cooling[2-5], multi-exciton dynamics[6-9], and Carrier Multiplication (CM)[10]. For solar cell applications, the occurrence of highly efficient CM in QDs could in principle be promising. CM is the process in which the absorption of a single, high-energy photon results in the generation of 2 or more electron-hole pairs. CM occurs only in the limit of energy conservation, when the photon energy E_{ph} is larger than twice the value of E_g. The utilization of novel light-absorbing materials that can employ the excess energy of hot carriers for generation of additional electron-hole pairs would lead to higher photocurrents, which is naturally very appealing for solar energy conversion.

As explained in Chapter 1, the efficiency of CM in bulk material is determined by two competitive processes for relaxation of 'hot' carriers to the valence or conduction band edge. First, hot carriers can relax via sequential emission of phonons (heat generation) but an alternative relaxation pathway for hot carrier relaxation is impact ionization. In this Auger process, the excess kinetic energy of the initially excited electron is employed to excite a second electron over the bandgap, rather than being converted into heat. The rate of impact ionization is described by Fermi's golden rule (equation 1.4) and is determined by Coulombic coupling between initial (hot carrier) and final (bi-exciton) states, and by the density of final states. In bulk materials, unfortunately, relaxation of hot carriers via phonon emission is faster than relaxation via impact ionization. As a result, CM has been shown to be relatively inefficient for bulk materials like silicon[11] and germanium[12] at visible photon energies and impact ionization does not contribute significantly to higher photo-currents in bulk semiconductor solar cells.

However, CM has been argued to be more efficient in QDs due to quantum-confinement effects causing (i) a slowing of the phonon-mediated relaxation channel[10] and (ii) enhanced Coulomb interactions[13], resulting from forced overlap between wave functions and reduced dielectric screening at the QD surface[14]. The expectation of high CM factors (defined as the number of photo-generated excitons per absorbed photon) in QDs was fulfilled by a first report on efficient CM in PbSe QDs by the Klimov group[13]. After this initial report, several femtosecond spectroscopy studies have revealed considerable CM in PbS and PbSe[13,15,16,17,18,19], PbTe[20], CdSe[21], Si[22,23], and InAs[24,25] QDs. The highest CM factor was reported for PbSe QDs, with a demonstrated yield of up to seven carriers per photon[17]. In recent years, however, the occurrence and the reported high CM factors in QDs have been questioned by several groups[26-28]. Therefore, it is important to perform additional CM measurements on QDs to obtain an explanation for the discrepancy in literature reports.

The work in this chapter contributes to the discussion in literature by an investigation of multi-exciton recombination (MER) dynamics and an assessment of the CM factor in colloidal InAs QDs. CM in QDs is usually demonstrated by signatures of MER (indicating the presence of multi-excitons) in the limit of low excitation densities (<< 1 absorbed photon per QD). We investigate the characteristics of MER in InAs QDs and discuss the challenges that are associated with the determination of the mechanism underlying MER using ultrafast spectroscopic techniques like TA or THz-TDS. Understanding MER is not only important in the assessment of the fundamental CM factors, but is also relevant for the utilization of CM in a QD-based solar cell: in order to extract the additional carriers generated by CM, the multi-excitons need to be extracted from the QDs before MER takes place. Hence, the extraction yield is determined by two competitive processes, MER and extraction of charges from the QDs. In section 4.3, the timescale of MER is characterized and in Chapter 6, the timescale of carrier extraction is investigated. In section 4.4, we asses the CM factor in InAs QDs after excitation with 400 nm excitation pulses. For the investigated QDs, the energy of a 400 nm photon corresponds to 2.74 and 3.26 times the QD energy gap, hence CM should be possible from the point of view of conservation of energy. At the end of this chapter, a summary of possible experimental pitfalls in the determination of CM in QDs is presented.

4.2 Experimental

Multi-exciton recombination (MER) can be monitored by probing the transient population of excitons in TA measurements[13,15,17,18,21,27] or THz-TDS measurements[29,30]. Additionally, MER can be probed by monitoring the radiative emission of (multi)excitons in time-resolved luminescence measurements[26,28]. Fig. 4.1(a) illustrates the nature of the signal in these different experimental approaches. Firstly, MER can be determined in TA
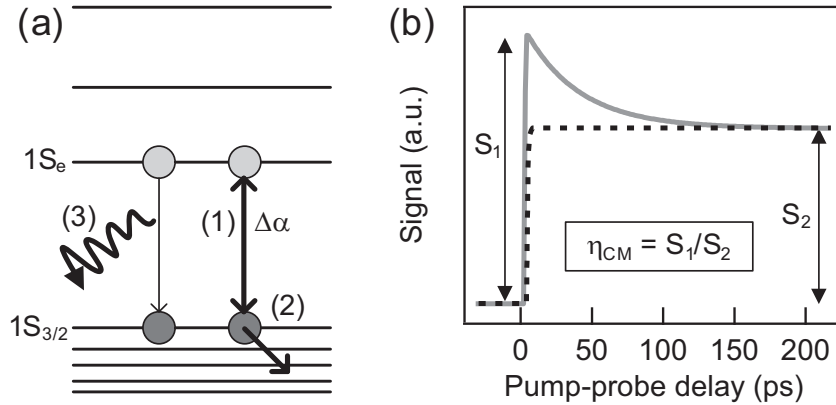
Figure 4.1 (a) Different experimental approaches to monitor multi-exciton recombination in CM studies: 1) TA, probing the bleach ($\Delta\alpha$) of the 1S exciton transition, 2) THz-TDS, probing the population of the $1S_{3/2}$ hole level via the exciton polarizability (see Chapter 3) and 3) time-resolved luminescence probing the radiative emission originating from the 1S exciton transition. (b) Two possible outcomes of a CM experiment in which the QDs are excited with low excitation fluence (<<1 photon absorbed per QD). In case only single excitons are formed (black dashed line, no CM), the signal is a step-like function since the lifetime of single excitons is much larger (~ 100 ns) than the time-window of the ultrafast experiment. In case of CM (grey solid line), multi-excitons are formed that decay to the single exciton state on a picosecond timescale. The CM factor, η_{CM}, is determined by dividing the signal right after excitation (S_1) by the long–time signal (S_2).

measurements by monitoring the bleach ($\Delta\alpha$) of the 1S exciton transition as a function of pump-probe delay time. Secondly, as explained in Chapter 3, THz-TDS can be used to probe the transient exciton population by monitoring the population of the $1S_{3/2}$ hole level via the exciton polarizability. Thirdly, time-resolved luminescence measurements are used to probe the radiative emission originating from (multi)excitons. The determination of MER dynamics in InAs QDs, as presented in section 4.3, was done by performing THz-TDS experiments and the results were compared with MER reports from literature that were obtained with TA or time-resolved luminescence. MER was characterized by exciting the InAs QDs with 800 nm light at various excitation fluences. The energy of an 800 nm photon (1.55 eV) is lower than $2 \cdot E_g$, as a result of which CM cannot take place due to energy conversation restrictions and multi-excitons are only generated by sequential photon absorption. MER was investigated in InAs QDs of 4.0, 4.9, and 5.45 nm diameter, corresponding to energy gaps of 1.33, 1.11, and 0.95 eV, respectively. The 4.0 nm QDs were TOP-passivated and the 4.9 nm and 5.45 nm QDs were passivated with CdSe/ZnSe-shells.

The experimental determination of CM relies on the detection of multi-excitons when exciting with low fluences (<< 1 photon absorbed per QD). In a typical time-resolved CM experiment (TA, THz-TDS or time-resolved luminescence), QDs are excited with photons

that have more energy than two times the QD energy gap. The reason that photons should have *more* energy than twice the QD energy gap is that the excess energy of the photon is usually distributed over the electron and the hole. Hence, a photon with exactly two times the energy of the QD 1S transition does usually not create hot carriers with sufficient energy for CM to occur. The demonstration of CM relies on the presence of a MER signature in the limit where at most one photon was absorbed per QD. This low excitation density limit (<< 1 photon absorbed per QD, on average) is typically achieved by exciting the sample with very low pump fluence. It is crucial that the excitation fluence is sufficiently low, since multi-excitons can also be created by sequential absorption of multiple photons, as is evident from MER experiments.

CM was studied in 4.9 and 5.45 nm InAs QDs by exciting the QDs with 400 nm laser pulses. Fig. 4.1(b) illustrates two possible outcomes for a typical measurement to determine the occurrence of CM in QDs. In case the absorption of a single high-energy photon results in the formation of a single exciton (no CM, black dashed line), the signal is a step-like function since the lifetime of single excitons is much larger (~ 100 ns) than the time-window of the ultrafast experiment. In contrast, in case of efficient CM the absorption of a single high-energy photon results in the generation of multi-excitons. Multi-excitons decay to the single exciton state on a picosecond timescale (grey solid line). In the example of Fig. 4.1(b), the time constant for the multi-exciton decay is (arbitrarily) chosen to be 35 ps. The CM factor, η_{CM}, is determined by dividing the signal right after excitation (S_1) by the long lived signal (S_2).

The energy of a 400 nm photon (3.1 eV) corresponds to $2.74 \cdot E_g$ (4.9 nm QDs) and $3.26 \cdot E_g$ (5.45 nm QDs). Hence, a 400 nm photon has in principle enough energy to generate carriers with sufficient energy to make relaxation via CM possible. To fulfill the requirement that no more than one 400 nm photon is absorbed by the QDs, the 400 nm excitation fluence should be chosen very low because the absorbance increases rapidly with photon energy, as is shown in Fig. 4.2. As follow from Lambert-Beer law[31], the absorbance is equal to $A = \sigma \cdot l \cdot N$, where σ is the absorption cross section, l is the path length of the sample, and N the (number) density. For a given sample (with constant values of l and N), the wavelength-dependent absorbance varies linearly with the wavelength-dependent absorption cross section. Hence, the relative difference between the absorption cross sections at 400 nm excitation (σ_{400nm}) and at 800 nm excitation (σ_{800nm}) can be obtained from the absorption spectrum. The ratio between the absorbance at 400 nm and 800 nm in Fig. 4.2 indicates that σ_{400nm} is roughly 10 times larger than σ_{800nm}. To avoid multi- photon absorption in the CM experiment, the 400 nm excitation fluence has to be 10 times lower than in the low-excitation (<< 1 photon absorbed per QD) 800 nm experiment.
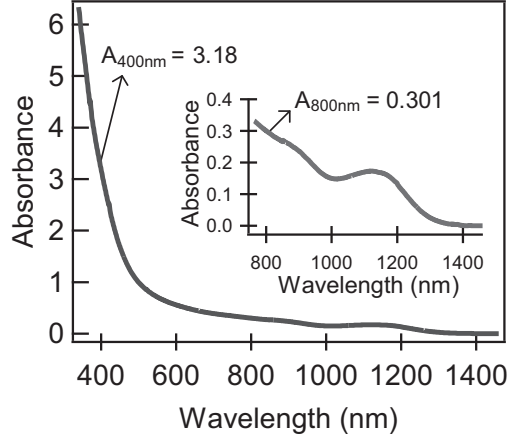
Figure 4.2 Absorption spectrum of 4.9 nm InAs QDs, dispersed in toluene. The inset is a close-up view of the absorption spectrum around the 1S exciton transition (located at ~ 1100 nm). From the values of the absorbance at 400 and 800 nm, it follows that the absorption cross section at 400 nm, σ_{400nm} is roughly 10 times larger than σ_{800nm}.

4.3 Multi-exciton recombination (MER) in InAs QDs

The fast (~ picosecond) decay of multi-excitons in QDs is usually assumed to be caused by an Auger recombination process, in which the recombination energy of an exciton is transferred to a third particle, either an electron or a hole[6,7,9]. In bulk material, the decay of the carrier density via Auger recombination can be described with the following differential equation:

$$\frac{dn_{eh}}{dt} = -\frac{n_{eh}}{\tau_A} \tag{4.1}$$

In this equation, the time constant for Auger recombination τ_A corresponds to a continuum of density-dependent recombination times: $\tau_A^{-1} = (C_A n_{eh}^2)$, in which C_A is the Auger constant[32]. In contrast, Auger recombination in QDs is characterized by a set of discrete recombination constants τ_2, τ_3, and τ_4, corresponding to the recombination rates of the bi-exciton, tri-exciton, and four-exciton state, respectively[6]. Hence, the discrete decay time constant τ_N in the Auger regime is given by $\tau_N^{-1} = C_A(N^2/V_0^2)$ for $N \geq 2$, in which N is the number of excitons and V_0 is the QD volume. From this expression for the discrete decay time constant, a ratio for $\tau_4/\tau_3/\tau_2$ of 0.25/0.44/1 can be predicted, which was also experimentally observed in Refs. 6,7,9. The conclusion that MER proceeds via an Auger mechanism based on the value of the τ_3/τ_2 ratio should be made with care, however. The

initial proposition that a τ_3/τ_2 ratio of 0.44 always corresponds to an Auger mechanism[6], was later refined by taking into account the symmetry of the multi-exciton states[9]. Furthermore, the value of the τ_3/τ_2 ratio for QDs of a specific material is not constant, but has been observed to increase with QD size[7,9]. For example, the τ_3/τ_2 ratio has been reported to change from $\sim$ 0.44 for 2.9 nm CdSe QDs to $\sim$ 0.29 for 8.0 nm CdSe QDs[9]. An alternative indication for an Auger-like mechanism of MER would be a decreased recombination rate for decreasing overlap between hole and electron wavefunctions. However, the work of Pandey et al. has indicated that separation of electrons and holes has a negligible effect on τ_2, which is inconsistent with the Auger hypothesis[8]. The authors of Ref. 8 therefore propose that MER might occur via a two-step process, in which two $1S_e$ electrons pair up to form a metastable state (with a rate-determining step), which reacts subsequently with a hole.

In this section, we characterize the timescale of bi-exciton recombination, which is useful knowledge in the experiment to assess the occurrence of CM (section 4.4). Another goal of the MER experiments was to gain insight in the mechanism of MER by inferring the τ_3/τ_2 ratio from transient THz data. We demonstrate the difficulties in extracting reliable numbers for τ_3 from transient spectroscopy data. These difficulties are due to the uncertainty in the initial distribution of excitons at high excitation fluences. An additional complication arising specifically for THz spectroscopy (and also for TA) is that the magnitude of the THz signal does not increase linearly with the number of excitons per QD.

As in Chapter 3, we use the ability of THz-TDS to probe the transient population of the $1S_{3/2}$ hole level to study the dynamics of MER. The $1S_{3/2}$ hole level in InAs QDs is sixfold degenerate[33], allowing us to monitor the population dynamics of multiple (> 2) excitons directly[24]. This is in contrast to TA, where the population of the twofold degenerate $1S_e$ level is probed, as a results of which probing of multiple (> 2) excitons is much more indirect[6,9]. However, we point out below that, for two reasons, the THz signal does not necessarily increase linearly when increasing the number of excitons per QD. The first reason is that the polarizability varies from one electronic state to another[34], and therefore the total polarizability varies non-linearly with the occupation of states. The second reason comes from the saturation of the polarizability due to the depolarization field inside the QD (self-consistency). For a single QD of radius R, the total polarizability is given by the relationship[35]:

$$\alpha^{\text{tot}} = R^3 \frac{(\varepsilon_b - 1)}{(\varepsilon_b + 2)} \qquad (4.2)$$

where ε_b is the dielectric constant of the QD material. After excitation, the sphere becomes more polarizable. The maximum value of the total polarizability is obtained when $\varepsilon_b \rightarrow \infty$, resulting in the following relationship for its variation:

$$\Delta\alpha_{max}^{tot} = R^3 \left[1 - \frac{(\varepsilon_b - 1)}{(\varepsilon_b + 2)} \right] = FR^3 \qquad (4.3)$$

Using $\alpha = \Delta\alpha_{max}^{tot} / F^2$ [equivalent to Eq. (3.2)], we deduce that the polarizability of the excitons is necessarily smaller than a maximum value given by

$$\alpha_{max} = R^3 / F \qquad (4.4)$$

For the 4.9 nm QDs, α_{max} is equal to 70.000 Å^3, while the experimentally observed polarizability of a single exciton is $\sim$ 25.000 Å^3 (see Fig. 3.3). Therefore, it is evident that the THz-signal arising from a QD containing 3 excitons cannot be three times as large as the signal from a QD containing 1 exciton. It is also clear that perturbation calculations, which work quite well for single excitons, cannot predict correctly the polarizability of multi-excitons.

Fig. 4.4(a) shows the THz dynamics of 5.45 nm QDs for a range of 800 nm excitation intensities. The relevant time constants of the low-fluence data traces are quantified by modeling the system using a three-level model, where the levels consist of N_1, N_2, and N_3 containing one, two, and three excitons per QD, respectively. The time dependent populations (N_i) of each level are given by three coupled differential equations (see details in Fig. 4.3). We found that for the 0.25 μJ/mm^2 data trace, the contribution of tri-excitons is negligible and the dynamics can be described by a bi-exciton time constant τ_2 of 38 ± 2 ps. A similar analysis was done for the 4.0 and 4.9 nm QDs, yielding values for τ_2 of 9.5 ± 1 ps and $= 24 \pm 2$ ps, respectively. The scaling of τ_2 with QD radius follows roughly a R^3 dependence (inset Fig. 4.4a), which is in agreement with a cubic size dependence reported in Refs. 6-9.

$$\frac{dN_3}{dt} = A_3 \cdot \delta(t) - \frac{1}{\tau_3} N_3$$

$$\frac{dN_2}{dt} = A_2 \cdot \delta(t) + \frac{1}{\tau_3} N_3 - \frac{1}{\tau_2} N_2$$

$$\frac{dN_1}{dt} = A_1 \cdot \delta(t) + \frac{1}{\tau_2} N_2 - \frac{1}{\tau_1} N_1$$
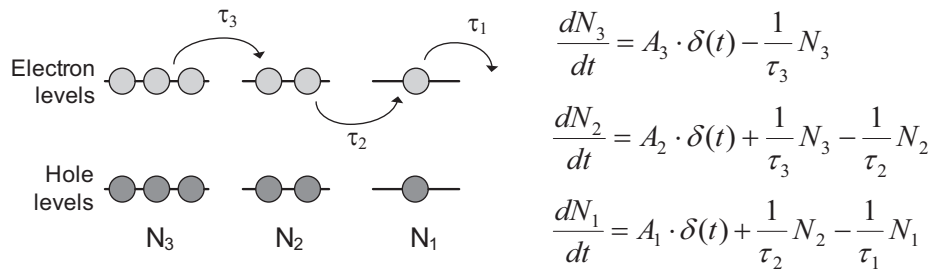
Figure 4.3 Schematic of the three-level model used infer the time constants for MER from the low-fluence data traces in Fig. 4.4, where the levels consist of N_1, N_2, and N_3 containing one, two, and three excitons per QD, respectively. The time dependent populations (N_i) of each level are given by three coupled differential equations.
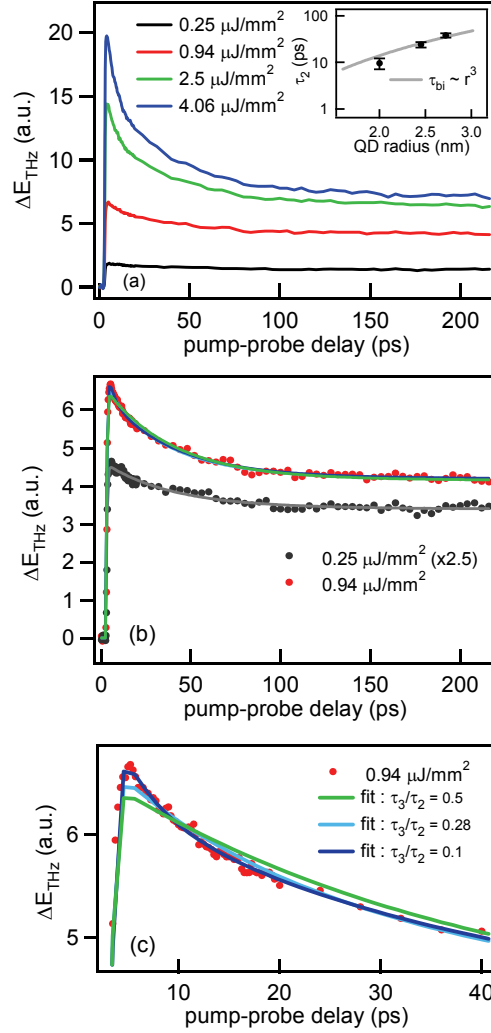
Figure 4.4 (a) Decay dynamics of THz measurements for 5.45 nm QDs for various 800 nm pump intensities. At high pump fluences multiple photons are absorbed per QD, leading to recombination of multi-excitons to the single exciton state within tens of picoseconds. The inset depicts the scaling of τ_2 with QD radius. (b) Fitting of two THz traces (0.25 and 0.94 μJ/mm^2) with a model of coupled rate equations, as described in the text. (c) Enlargement of the peak of the 0.94 μJ/mm^2 data trace.

Increasing the excitation fluence leads to appreciably faster decay dynamics, arising from recombination of higher exciton states (> 2 excitons per QD). The motivation for analyzing the decay time constants of these higher exciton states was to find a ratio for τ_3/τ_2 in order gain insight in the MER mechanism. Quantifying these recombination timescales

would be relatively straightforward in case the initial excitation distribution is known. However, the non-linear scaling of the THz signal with the number of QDs (discussed above) makes it difficult to directly infer the initial distribution of excitations from the magnitude of the THz signal. In principle the problem of this non-linear response could be overcome by assuming a Poissonian distribution for the initial excitation distribution[6,9,15]. However, it has been argued that the excitation distribution is non-Poissonian when $\langle N_0 \rangle > 1$ ($\langle N_0 \rangle$ is the average number of excitons per QD immediately following photo-excitation)[36]. For the high fluence data traces in Fig. 4.4(a), $N_{eh} > 1$, as a result of which the validity of Poissonian statistics is not ensured. Therefore, the 0.94 μJ/mm^2 data trace was fitted with the above-mentioned three-level model while letting the amplitudes free (since the initial excitation distribution was not known exactly). The excitation levels for the 0.94 μJ/mm^2 fluence are sufficiently low that the decay is predominantly caused by bi-exciton and tri-exciton recombination. The value of τ_2 was fixed at 38 ps. As can be seen in Fig. 4.4(b) and 4.4(c), the data is described best by a small value of the τ_3/τ_2 ratio (~ 0.1), which is much smaller than expected from the expression for the discrete decay time constant in an Auger process.

An alternative approach to extract MER time constants from transient data, following Ref. 6, did not give reliable results: This procedure[6] - a "subtractive" procedure to analyze TA data – has previously been applied to CdSe QDs. In this procedure, the transients at various fluences are normalized so that the long-time decay values match. The low pump intensity trace ($N_{eh} \ll 1$) is considered to show only single exciton dynamics and is subtracted from a trace recorded with sufficient pump intensity to excite bi-excitons. This procedure is assumed to yield purely bi-exciton dynamics and is repeated for traces with higher pump fluences, making it possible to extract also τ_3 and even τ_4. We attempted to implement this procedure for our THz traces at low fluences (0.25 and 0.94 μJ/mm^2 in Fig. 4.4(a), for which the non-linearity of the THz-signal is expected to be modest. However, we experienced that the outcome of this procedure is very sensitive to the exact value of the pump-probe delay at which the data is normalized. Therefore, it is conceivable that our THz data is more reliably analyzed with the multi-level model of coupled rate equations.

The above analysis illustrates that the extraction of τ_3 from THz data, and presumably also from TA data, is challenging. In contrast, the radiative emission from mono, bi, and tri-exciton states can be spectrally separated by transient photoluminescence measurements, as was shown in CdSe QDs[7], making it possible to reliably determine values for τ_2 and τ_3. We therefore argue that time-resolved photoluminescence spectroscopy is a more appropriate technique for drawing conclusions on the MER mechanism in InAs QDs from the τ_3/τ_2 ratio. However, THz-TDS is a suitable technique to assess bi-exciton

recombination dynamics in QDs, allowing one to use THz-TDS for CM QD studies (see next section).

4.4 CM in InAs QDs

In 2006, we performed initial experiments to assess the occurrence of CM in 4.9 nm InAs QDs, and based on these measurements we reported a CM factor of ~ 1.6 excitons per absorbed 400 nm photon[24]. However, after the reports of negligible CM in CdSe, CdTe[26], and InAs[27] QDs and the concurrently emerging controversy in the CM community, we decided to reproduce our initial measurements, and the results of these (optimized) experiments are discussed in this section.

As explained in Section 4.2, CM is characterized by the presence of relatively short-lived biexcitons (lifetime tens of ps)[13] which are created by the absorption of a single photon. However, biexcitons are also readily created by sequential multi-photon absorption. Hence, the relative yield of bi- versus single excitons has to be determined for fluences where multi-exciton generation by multi-photon absorption is negligible. In section 4.3, we have determined the magnitude of the 800 nm excitation fluence, for which light absorption resulted in no more than 1 exciton per QD. From Fig. 4.2, we concluded that σ_{800nm} is roughly 10 times smaller than σ_{400nm} for 4.9 nm InAs QDs, hence the 400 nm fluence should be chosen 10 times lower than the lowest 800 nm fluence in section 4.3 to ensure that at most one 400 nm photon is absorbed per QD. We verified that σ_{400nm} is also ~ 10 times larger than σ_{800nm} for 5.45 nm InAs QDs.

Figure 4.5 shows a comparison of the THz-TDS data for 400 and 800 nm excitation fluences that result in approximately the same average number of absorbed photons per QD (considering the optical density of the sample at the two wavelengths and the ratio of absorption cross sections $\sigma_{400nm}/\sigma_{800nm} = 10$). Fig. 4.5(a) shows this comparison for the 4.9 nm InAs QDs for the limit of low excitation fluence (<< 1 photon absorbed per QD). For 4.9 nm QDs ($E_g = 1.11$ eV), the 400 nm and 800 nm photon energy is equal to 2.79 and 1.40 times the QD energy gap, respectively. It is apparent from the data that there is no significant bi-exciton decay visible for excitation at low 400 nm fluence, pointing to the absence of CM. For the 5.45 nm QDs ($E_g = 0.95$ eV) in Fig. 4.5(b), the initially generated hot carriers have more excess energy, since 400 nm and 800 nm photons correspond to 3.26 and 1.63 times the QD energy gap, respectively. There seems to be a small bi-exciton decay component in the data of Fig. 4.5(b), but this component is present for both the 400 nm and 800 nm excitation wavelengths. Since the 5.45 nm QDs have a larger absorption cross section than the 4.9 nm QDs, this decay component (for comparable excitation fluence in Fig. 4.5(a) and 4.5(b) must originate from multi-photon absorption. Indeed, if we increase
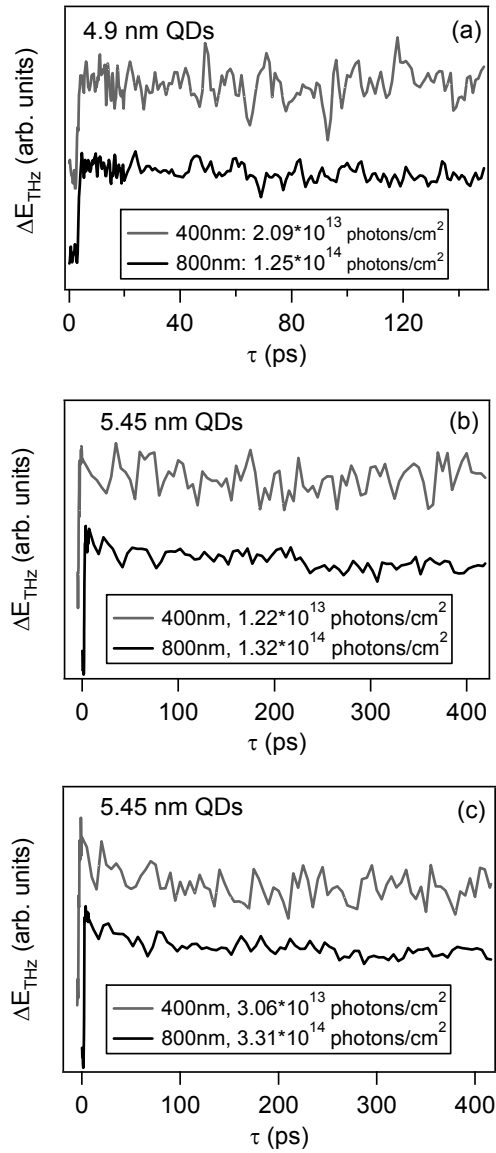
Figure 4.5 Comparison of transient THz data for 400 nm (grey line) and 800 nm (black line) excitation for 4.9 nm QDs (a) and 5.45 nm QDs (b and c). In all three comparisons, the 400 and 800 nm fluences are roughly equivalent, i.e. the average number of absorbed photons per QD is similar, taking into account that $\sigma_{400nm}/\sigma_{800nm} = 10$ for both 4.9 nm and 5.45 nm InAs QDs. The amplitude of the 400 nm data is ~ 10 times lower than that of the 800 nm data, but for clarity, all data is normalized to the signal at t_0.

both excitation fluences in a proportional manner for the 5.45 nm QDs (see Fig. 4.5(c)), there is a clear decay of the signal that can be attributed to bi-exciton recombination. Because of the equivalent fluences (~ average number of absorbed photons per QD is similar for 400 nm and 800 nm excitation), it is evident that the bi-excitons in case of 400 nm excitation are formed by sequential-photon absorption and not by CM. The observation of no or negligible CM in InAs QDs is in disagreement with the CM factor of 1.6 concluded in our initial experiments for the 4.9 nm QDs[24] and also with the CM factors reported in Ref. 25 under similar conditions.

4.5 Challenges in assessment CM in QDs

In the previous section, we demonstrated that the CM factor is small or negligible in InAs QDs, which is in agreement with Ref. 27 but in disagreement with our initial measurements[24], and with Ref. 25. There is a similar controversy on the occurrence of CM in different materials like PbSe[17,28], PbS[15,28], and CdSe[21,26]. In this section, we will argue that CM factors in initial studies may have been overestimated due to several experimental complications, including too high excitation fluences (generating multiple carriers by sequential photon absorption), lack of stirring of QD suspensions (causing photo induced charging) and sample-to-sample variability[37]. These effects, possibly explaining the contradictory observations in the CM literature, are discussed in more detail below:

- Besides CM, an alternative way of generating multiple excitons in QDs is by the sequential absorption of multiple photons in the same excitation pulse. The decay of multiple excitons generated by multi-photon absorption is indistinguishable from those generated by CM. Hence, in the experiments aimed at elucidating CM, one has to ensure that the excitation density is sufficiently low so that multi-photon absorption is negligible. To meet this criterion requires that the average initial excitation density per quantum dot, $\langle N_0 \rangle$ is sufficiently small, *at all positions within the sample.* This latter boundary condition is important, as for samples of large optical density, an excitation gradient occurs along the propagation direction of the excitation pulse. To a first approximation, for a given $\langle N_0 \rangle$ at low excitation fluence the relative populations of exciton, bi-exciton, and tri-exciton states can be described by a Poisson distribution[6,7,36]. In Poisson statistics, the probability of generating a particular number (m) of 1,2…N excitons per QD is given by[6,7]:

$$p(m) = \frac{\langle N_0 \rangle^m}{m!} \exp^{-N_0} \qquad (4.5)$$

In initial CM reports, the value of the required low excitation fluence was calculated by $F = \langle N_0 \rangle / \sigma$, in which σ is the absorption cross section. In these initial reports[13,15], however, values for $\langle N_0 \rangle$ of 0.25 - 0.6 were used, but as can be seen in Fig. 4.6, there is a significant fraction of bi- and even tri-excitons for $\langle N_0 \rangle = 0.6$. Hence, it is likely that the use of too high pump fluences in early reports has resulted in sequential-photon absorption and the corresponding multi-exciton

Figure 4.6 Poisson distribution for $\langle N_0 \rangle$ = 0.1 and 0.6, where $\langle N_0 \rangle$ is the average excitation density per QD

decay signatures[37]. Since the absorption cross section increases strongly for shorter wavelengths (see Fig. 4.2), the 400 nm excitation fluence for which there is no multi-photon absorption is at least 10 times lower than the 800 nm fluence that corresponds to $\langle N_0 \rangle \sim 0.1$. Such 400 nm fluences are associated with very low excitation densities, resulting in very small signals in spectroscopic measurements. Small signals require the use of experimental setups with excellent signal-to-noise characteristics. Even though the THz-TDS setup has good signal-to-noise characteristics, the data traces for 400 nm excitation in Fig. 4.5 were obtained after more than 12 hours of data acquisition, which was necessary to reduce the noise to acceptable levels.

- Spatial inhomogeneities in the excitation beam (so-called 'hotspots'), may lead to multi-photon absorption, locally in the excitation beam. If this occurs, bi-excitons may be formed in the sample, despite the fact that the average number of excitons remains low. The experimental results at 400 nm excitation presented in Fig. 4.5 have been measured with a so-called 'diffuser' in the excitation beam. The use of the diffuser resulted in a homogeneous beam profile, which was verified by recording the beam profile with a camera.

- Additionally, it is not evident that the CM factor is reliably determined by assessing the ratio of S_1/S_2 (see Fig. 4.1(b)) in transient ultrafast measurements. As we have demonstrated in section 4.3, the THz signal does not scale linearly with the number excitons per QD as a result of which the CM factor may be underestimated. Also in Transient Absorption measurements, the signal does not necessarily scale linearly with exciton population, because of the twofold degeneracy of the $1S_e$ level in e.g. InAs and CdSe QDs. On the other hand, the CM factor may be overestimated if the assumption that all multi-excitons decay to the single exciton state (represented by the level of S_2)
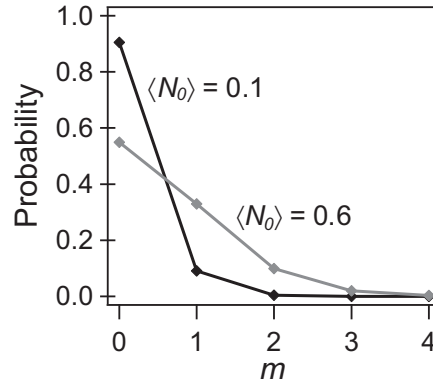
75

is wrong. It is conceivable that the QDs are heated by the pump pulses to such extent that thermally induced ionization takes place, leading to an underestimation of S_2 and hence an overestimation of the CM factor.

- Another experimental concern in experimental studies of CM using (high-intensity) ultrafast spectroscopy is the occurrence of "CM-like" decay signatures resulting from pump-induced effects such as degradation of surface passivation or QD photo-ionization leading to QD charging[37]. The degradation of surface passivation can result in new decay pathways in the form of trapping at surface defects, while QD photo-ionization can result in extraneous "CM-like" decay signatures due to e.g. Auger recombination of charged excitons (trions). In some (but not all) experiments, stirring the QD solutions resulted in a lower measured CM factor than in the case of measuring on static (non-stirred) samples[37].

- Finally, the QDs studied in the various CM reports are synthesized under different experimental conditions. It is possible that the resulting sample-to-sample variability results in different (surface) properties, which might explain the spread of the reported CM factors. However, the QD synthesis has become more sophisticated in recent years and the latest experimental reports consistently show that the CM factors are much lower than reported in initial CM studies.

4.6 Conclusions

To conclude, we have investigated the dynamics of multi-exciton recombination (MER) in colloidal InAs QDs using THz-TDS. The time constant associated with the recombination of a bi-exciton to the single exciton state was found to be ~10 – 40 ps, depending on the QD size. We also demonstrated that it is challenging to draw conclusions on the MER mechanism from THz-TDS data, primarily because the THz signal does not scale linearly with the number of excitons in a QD. The presence of bi-exciton recombination in the limit of low excitation fluence is a signature for the occurrence of Carrier Multiplication, the process in which multiple excitons are generated in QDs after the absorption of a single photon. In our studies, we find that the Carrier Multiplication factor (i.e. number of generated excitons per absorbed photon) is small or negligible in InAs QDs, in contrast to previous reports. Several experimental pitfalls in the determination of Carrier Multiplication were identified that may lead to an overestimation of the CM factor, including the use of too high excitation fluences and the presence of local hotspots in the excitation beam, both leading to the generation of multi-excitons via sequential-photon absorption.

References

(1)   van Driel, A. F.; Allan, G.; Delerue, C.; Lodahl, P.; Vos, W. L.; Vanmaekelbergh, D. *Phys. Rev. Lett.* **2005**, *95*, 236804.
(2)   Klimov, V. I.; McBranch, D. W. *Phys. Rev. Lett.* **1998**, *80*, 4028-4031.
(3)   Klimov, V. I.; McBranch, D. W.; Leatherdale, C. A.; Bawendi, M. G. *Phys. Rev. B* **1999**, *60*, 13740-13749.
(4)   Guyot-Sionnest, P.; Shim, M.; Matranga, C.; Hines, M. *Phys. Rev. B* **1999**, *60*, R2181-R2184.
(5)   Hendry, E.; Koeberg, M.; Wang, F.; Zhang, H.; Donega, C. d. M.; Vanmaekelbergh, D.; Bonn, M. *Phys. Rev. Lett.* **2006**, *96*, 057408-057404.
(6)   Klimov, V. I.; Mikhailovsky, A. A.; McBranch, D. W.; Leatherdale, C. A.; Bawendi, M. G. *Science* **2000**, *287*, 1011-1013.
(7)   Fisher, B.; Caruge, J. M.; Chan, Y. T.; Halpert, J.; Bawendi, M. G. *Chem. Phys.* **2005**, *318*, 71-81.
(8)   Pandey, A.; Guyot-Sionnest, P. *J. Chem. Phys.* **2007**, *127*, 4.
(9)   Klimov, V. I.; McGuire, J. A.; Schaller, R. D.; Rupasov, V. I. *Phys. Rev. B* **2008**, *77*, 195324-195335.
(10)   Nozik, A. J. *Physica E* **2002**, *14*, 115-120.
(11)   Kolodinski, S.; Werner, J. H.; Wittchen, T.; Queisser, H. J. *Appl. Phys. Lett.* **1993**, *63*, 2405-2407.
(12)   Koc, S. *Czech. J. Phys.* **1957**, *7*, 91-95.
(13)   Schaller, R. D.; Klimov, V. I. *Phys. Rev. Lett.* **2004**, *92*.
(14)   Klimov, V. I. *Ann. Rev. Phys. Chem.* **2007**, *58*, 635-673.
(15)   Ellingson, R. J.; Beard, M. C.; Johnson, J. C.; Yu, P. R.; Micic, O. I.; Nozik, A. J.; Shabaev, A.; Efros, A. L. *Nano Lett.* **2005**, *5*, 865-871.
(16)   Schaller, R. D.; Agranovich, V. M.; Klimov, V. I. *Nature Phys.* **2005**, *1*, 189-194.
(17)   Schaller, R. D.; Sykora, M.; Pietryga, J. M.; Klimov, V. I. *Nano Lett.* **2006**, *6*, 424-429.
(18)   Trinh, M. T.; Houtepen, A. J.; Schins, J. M.; Hanrath, T.; Piris, J.; Knulst, W.; Goossens, A.; Siebbeles, L. D. A. *Nano Lett.* **2008**, *8*, 1713-1718.
(19)   Ji, M.; Park, S.; Connor, S. T.; Mokari, T.; Cui, Y.; Gaffney, K. J. *Nano Lett.* **2009**, *9*, 1217-1222.
(20)   Murphy, J. E.; Beard, M. C.; Norman, A. G.; Ahrenkiel, S. P.; Johnson, J. C.; Yu, P. R.; Micic, O. I.; Ellingson, R. J.; Nozik, A. J. *J. Am. Chem. Soc.* **2006**, *128*, 3241-3247.
(21)   Schaller, R. D.; Petruska, M. A.; Klimov, V. I. *Appl. Phys. Lett.* **2005**, *87*, 253102.
(22)   Beard, M. C.; Knutsen, K. P.; Yu, P.; Luther, J. M.; Song, Q.; Metzger, W. K.; Ellingson, R. J.; Nozik, A. J. *Nano Lett.* **2007**, *7*, 2506-2512.
(23)   Timmerman, D.; Izeddin, I.; Stallinga, P.; Yassievich, I. N.; Gregorkiewicz, T. *Nat Photon* **2008**, *2*, 105-109.
(24)   Pijpers, J. J. H.; Hendry, E.; Milder, M. T. W.; Fanciulli, R.; Savolainen, J.; Herek, J. L.; Vanmaekelbergh, D.; Ruhman, S.; Mocatta, D.; Oron, D.; Aharoni, A.; Banin, U.; Bonn, M. *J. Phys. Chem. C* **2007**, *111*, 4146-4152.
(25)   Schaller, R. D.; Pietryga, J. M.; Klimov, V. I. *Nano Lett.* **2007**, *7*, 3469-3476.
(26)   Nair, G.; Bawendi, M. G. *Phys. Rev. B* **2007**, *76*, 4.
(27)   Ben-Lulu, M.; Mocatta, D.; Bonn, M.; Banin, U.; Ruhman, S. *Nano Lett.* **2008**, *8*, 1207-1211.
(28)   Nair, G.; Geyer, S. M.; Chang, L.-Y.; Bawendi, M. G. *Phys. Rev. B)* **2008**, *78*, 125325-125310.
(29)   Hendry, E.; Koeberg, M.; Pijpers, J.; Bonn, M. *Phys. Rev. B* **2007**, *75*, 233202.

(30)   Pijpers, J. J. H.; Hendry, E.; Milder, M. T. W.; Fanciulli, R.; Savolainen, J.; Herek, J. L.; Vanmaekelbergh, D.; Ruhman, S.; Mocatta, D.; Oron, D.; Aharoni, A.; Banin, U.; Bonn, M. *J. Phys. Chem. C* **2008**, *112*, 4783-4784.
(31)   Atkins, P. W. *Physical Chemistry*, 4th ed.; Oxford University Press: Oxford, 1990.
(32)   Landsberg, P. T. *Recombination in Semiconductors*; Cambridge University Press, 2003.
(33)   Banin, U.; Cao, Y. W.; Katz, D.; Millo, O. *Nature* **1999**, *400*, 542-544.
(34)   Wang, F.; Shan, J.; Islam, M. A.; Herman, I. P.; Bonn, M.; Heinz, T. F. *Nature Mater.* **2006**, *5*, 861-864.
(35)   Born, M.; Wolf, E. *Principles of Optics*, Second ed.; Pergamon Press: Oxford, 1964.
(36)   Huxter, V. M.; Scholes, G. D. *J. Chem. Phys.* **2006**, *125*.
(37)   McGuire, J. A.; Joo, J.; Pietryga, J. M.; Schaller, R. D.; Klimov, V. I. *Acc. Chem. Res.* **2008**, *41*, 1810-1819.

Chapter 5
Carrier Multiplication in bulk PbSe and PbS

5.1 Background

One of the important factors limiting solar cell efficiencies is that incident photons generate one electron-hole pair, irrespective of the photon energy. Any excess photon energy is lost as heat. The possible utilization of the excess energy of hot carriers is therefore of great interest for future solar cells[1]. One promising approach to achieve this goal is Carrier Multiplication (CM), the process in which the absorption of a single, high-energy photon results in the generation of 2 or more electron-hole pairs. The excess energy of the initially excited electron is employed to excite a second electron over the bandgap, rather than being converted into heat via sequential phonon emission. In bulk semiconductors, CM proceeds via 'impact ionization', an Auger process in which the excess kinetic energy of a hot carrier is transferred to a valence electron via Coulomb interactions, thereby promoting a valence electron to the conduction band[2]. The CM factor (number of photo-generated electron-hole pairs per absorbed photon) in bulk semiconductors is determined by two competitive processes via which the initially generated hot carriers can relax: relaxation via sequential emission of phonons and relaxation via impact ionization. Unfortunately, phonon-mediated relaxation is the dominant relaxation pathway in most bulk materials explaining why CM factors in bulk are low for excitation with visible frequencies. As a result, relaxation of hot carriers via phonon emission is a common loss mechanism in bulk semiconductor solar cells.

In this context, semiconductor Quantum Dots (QDs) might be promising building blocks for future solar cells[1]. CM has been argued to be more efficient in nanostructured semiconductors due to quantum-confinement effects causing (i) a slowing of the phonon-mediated relaxation channel[1] and (ii) enhanced Coulomb interactions[3], resulting from forced overlap between wave functions and reduced dielectric screening at the QD surface[4]. In recent years, several femtosecond spectroscopy studies have revealed considerable CM in PbS and PbSe[3,5,6,7,8,9], PbTe[10], CdSe[11], Si[12], and InAs[13,14] QDs. Besides the conventional models based on impact ionization[15-17], new mechanisms were proposed to describe CM in QDs including the coherent superposition of single and multi-exciton wavefunctions[4] and the occurrence of virtual single exciton states[5].

Nearly concurrently, however, a controversy has emerged following reports of appreciably less efficient CM in CdSe[18], InAs[19,20], PbS[21] and PbSe[21,22] QDs. The authors of

these reports argued that CM factors may have been overestimated in initial studies due to several experimental complications, including too high excitation fluences (generating multiple carriers by sequential absorption of multiple photons), lack of stirring of QD suspensions (causing photo induced charging) and sample-to-sample variability[22], as elaborated in the previous chapter. Furthermore, recent tight binding calculations[15] suggest that CM in QDs is not only not enhanced relative to bulk, but is actually lower. Answering the key question in the controversy -whether the CM factor increases due to quantum-confinement effects- requires a reliable comparison between CM factors in bulk and QDs. Remarkably, reliable numbers for CM factors in bulk materials are limited. PbSe and PbS are arguably the most important materials in the CM discussion, since their small bulk bandgap values result in an optimal energy gap for QDs of these materials to utilize the excess energy of visible photons of the solar spectrum. However, reports of bulk CM factors in PbSe and PbS are, respectively, absent or dated[23]. For PbS, there is only one report available from 1958 on CM in a PbS photovoltaic device[23]. In a device measurement, multiplication factors are determined on long timescales, relying on photocurrent measurements, which require charges to move over large distances. For the bulk-QD comparison, Ref. 23 is of limited use because of a number of potential uncertainties in this work, as first pointed out by Nair et al.[21] Two of the most important uncertainties of the PbS device measurement[23] are given below:

1. The (commercial) PbS film used by Smith[23] was not characterized. As a result, severe oxidation of the sample surface will have taken place at the sample surface. The presence of a thin layer of PbO at the surface might influence the results of CM device measurements (see section 5.2).

2. At high photon energy, carriers are generated in the proximity of the sample surface where the greatest concentration of trap sites is expected to reside. Trapped carriers do not contribute to the macroscopic photo-current, hence trapping can lead to an underestimation of the CM factor.

Whereas CM in bulk materials is usually determined in photocurrent device measurements, i.e. by collecting the carriers, CM in QDs is studied with (optical) spectroscopic measurements, in which the orbital occupation of the QDs is probed on ultrafast (picosecond) time scales. Hence, the commonly used experimental procedures to determine CM in QDs (ultrafast spectroscopy) and in bulk (device measurements) are rather different. While time-resolved optical and IR spectroscopies are ideally suited to probe carrier populations in colloidal QDs[3,5,7,8,10,11,14,18,20-22,24-26], light of TeraHertz (THz) frequencies interacts strongly with free carriers in bulk material, and allows for the direct characterization of carrier density and mobility[27-29] (see Chapter 2). From THz-TDS experiments, one can quantitatively assess the number of photogenerated carriers

picoseconds after the light is absorbed. Additionally, as a result of the contact-free nature of the THz probe, it is possible to determine the CM factor in isolated samples of bulk semiconductors without the need of applying contacts, which is necessary in the device measurements.

In this chapter, we quantify CM in bulk PbSe and PbS on ultrafast timescales using THz time-domain spectroscopy (THz-TDS)[28]. We directly determine the number of photo-generated electron-hole pairs per absorbed photon, η, for various photon energies from the UV to the IR. As illustrated in Fig. 5.1, the photo-induced THz modulation, which is related to the photoconductivity and hence to the number photo-generated carriers (see Chapter 2), can be measured with picosecond time-resolution, allowing for a direct comparison with previous QD results. Our results show that, for a given photon energy, an equal amount or more electron-hole pairs per photon are generated in bulk than in QDs. Hence, if QDs are claimed to exhibit more efficient CM, this claim is related to the ratio of the exciton energy and the photon energy that is indeed larger for QDs than for bulk systems, as we will argue in section 5.6.
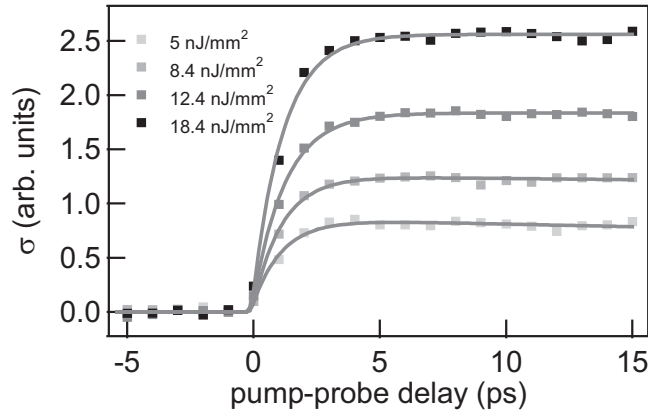

Figure 5.1 THz conductivity as a function of pump-probe delay for the PbS film for various 800 nm fluences. The increase of $\Delta E(t)$ with fluence is directly related to the higher carrier density, as explained in the text.

5.2 Samples

Epitaxial single crystalline films of PbSe and PbS were grown using chemical solution deposition on GaAs(100) and GaAs(111) substrates respectively and showed a well-defined orientation relationship with the substrate[30,31,32,33]. Transmission Electron Microscopy (TEM) and Scanning Electron Microscopy (SEM) were used to determine the thickness of the films (~ 1 μm) and the flatness of the surface. Optimizing deposition parameters

resulted in high quality surface flatness. X-ray and electron diffraction indicated the presence of single-crystalline PbSe and PbS films. We experienced that the presence of a native oxide layer consisting of PbO or more likely, of Pb(O,Se) at the PbSe surface had a significant effect on the magnitude of the THz modulation. Possible explanations for the different THz results are (i) different reflectivity of pump photons from a PbO surface compared to a PbSe surface (ii) absorption of pump photons by the oxide layer (the bandgap of PbO varies from 2.07 – 3.36 eV, depending on the crystallographic phase[34]), and (iii) different mobility in PbSe that was exposed to oxygen[35,36], leading to different magnitudes of the THz signals. To determine the CM yields in the absence of the PbO layer, we etched the PbSe sample with a 10% HCl solution to remove the oxygen before doing all THz measurements. The removal of oxygen is monitored by energy-dispersive X-ray spectroscopy (EDX), as demonstrated in Fig. 5.2. Clearly, the O-peak at 0.5 keV has disappeared after the etching procedure. Oxidation occurred to a lesser extent at the PbS sample. A comparison between the oxidized sample and a sample where the native oxide had been removed by etching did not change the results of the THz measurements for PbS.
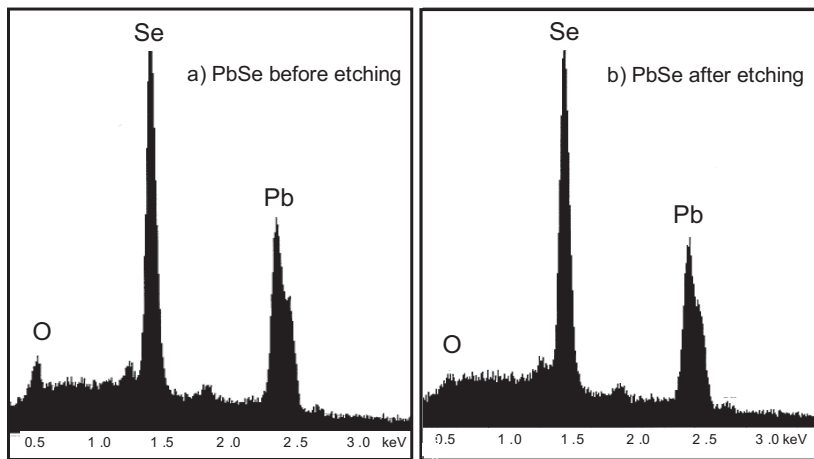

Figure 5.2. EDX spectra of the PbSe film (a) before etching and (b) after etching with a 10% HCl solution

5.3 Experimental considerations in assessment of the CM factor

The reliable determination of CM factors in single crystalline PbSe and PbS films requires the accurate determination of 2 parameters: the number of absorbed photons per unit area and the number of generated carriers. First, we achieve a homogeneous photon flux using a diffuser and determine the fluence at the sample position with ~ 3% accuracy using five calibrated pinholes with increasing area. For the calculation of the number of *absorbed*

photons per mm^2, the reflective losses at the sample surface have been taken into account by using the frequency-dependent optical properties of bulk PbS and PbSe from Refs. 37 and 38, respectively. Secondly, the amount of generated electron-hole pairs is determined using THz-TDS measurements[28]. This technique has been used extensively to determine carrier dynamics in semiconductors, as it provides the frequency-dependent complex conductivity $\sigma(\omega)$ of charge carriers[27,29]. We measure in the time domain the electric field of picosecond THz pulses transmitted through the unexcited sample $E(t)$. The changes therein, $\Delta E(t)$, following photo-injection of charge carriers using femtosecond laser pulses directly reflect the charge carrier density. Fig. 5.3 shows the complex conductivities $\sigma(\omega)$ for PbS (E_{gap} = 0.42 eV) following excitation with two different 266 nm (4.66 eV) fluences, as inferred from the Fourier transforms of the time-domain fields[29]. We follow prior authors[28,29] and fit the data in Fig. 5.3 with the Drude model of free carriers, $\sigma(\omega) = (\varepsilon_0 \, \omega_p^2 \, \tau_r) / (1 - \omega\tau_r)$, where ω_p is the plasma frequency, ε_0 the vacuum permittivity and τ_r the carrier scattering time[29] (as also described in Chapter 2). The plasma frequency is defined as $\omega_p^2 = (e^2 N)/(\varepsilon_0 m^*)$, where m^* is the carrier effective mass, e is the electron elementary charge, and N is the carrier density.
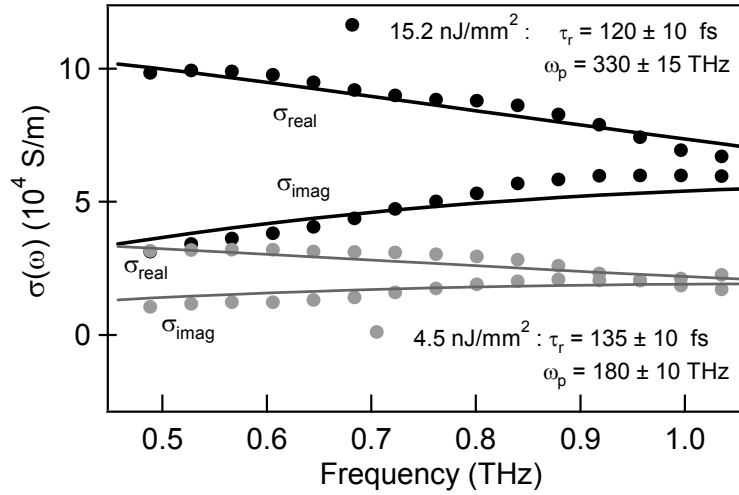

Figure 5.3. Complex, frequency dependent conductivities for PbS measured 10 ps after photo-excitation for two different 266 nm excitation fluences (black and grey dots). The data is described well by the Drude expression (solid lines) yielding the plasma frequency (directly related to density) and the carrier scattering time.

The black dots in Fig. 5.3 represent the photoconductivity that was measured at an excitation fluence of 15.2 nJ/mm^2 266 nm light. This fluence corresponds to 9.56·10^9 absorbed photons/mm^2, taking the 266 nm reflectance at the PbS surface into account. The

data in Fig. 5.3 (measured at a pump-probe delay of 10 ps) was fitted with the Drude expression, yielding a plasma frequency of $\omega_p = 3.30 \cdot 10^{14}$ Hz. From the value of ω_p, a carrier density of $6.85 \cdot 10^{24}$ m^{-3} is calculated, given the electron and hole effective masses ($m_e \sim m_h \sim 0.20$ at room temperature)[39]. Using the 266 nm penetration depth of PbS, the carrier density is converted into a sheet density of $2.92 \cdot 10^{10}$ electron-hole pairs per mm^2. Here, we also took into account that in PbS, both electrons and holes make comparable contributions to $\Delta E(t)$ because of their similar effective masses. Dividing the sheet density by the number of absorbed photons per mm^2 yields η, the number of electron-hole pairs per absorbed photon. For the 15.2 nJ/mm^2 data in Fig. 5.3, η was found to be 3.05 ± 0.15 electron-hole pairs per absorbed photon. This value clearly demonstrates the occurrence of CM in bulk PbS for excitation with 266 nm photons (having 11 times the energy of the PbS band gap). Performing the same procedure for the 4.5 nJ/mm^2 fluence data (grey dots in Fig. 5.3), one finds a value for η of 3.06 ± 0.15 electron-hole pairs per absorbed photon. The good agreement between the found CM factors illustrates the validity of our procedure for a range of fluences. The same analysis for 800 nm excitation results in an average of 1.02 ± 0.05 generated electron-hole pairs for each absorbed photon, indicating that CM does not occur significantly for 800 nm excitation (3.7 times the bandgap energy).

As can be seen from Fig. 5.3, the scattering time does not change significantly as a result of a threefold increase of the excitation fluence. This observation is important, since it implies that the linear increase of the THz signal with fluence is not caused by variations in τ_r, but is directly related to higher values of ω_p (hence, linear increase of carrier density). The obtained scattering times from our Drude fits are largely consistent with reported room-temperature electron and hole mobilities[40] of ~ 600 cm^2/V·s. Such mobilities correspond to scattering times of ~ 70 fs, whereas we find values of ~ 120 fs. It is intuitive that THz spectroscopy provides somewhat larger values for scattering time (and, accordingly, mobilities)[27]. The reason for this is that THz spectroscopy probes the mobility over very short length scales ($\sim$ nm), since the field is only 'switched on' for a $\sim$ ps. As a result, mobilities inferred from THz measurements are not affected by the presence of defects such as grain boundaries, which may act to reduce the mobility in conventional measurements that require motion over longer length scales. Indeed, conventionally measured mobilities in multicrystalline PbS films are 1-2 orders of magnitude lower than mobilities reported for single crystalline material[41].

When calculating the carrier density from the plasma frequency, we assumed that the carrier effective mass remained constant for the different excitation fluences. In principle however, high excitation fluences in femtosecond experiments might lead to changes in the carrier effective mass due to either non-parabolicities induced by high carrier densities and/or through band-filling[42]. We have previously[29] investigated the effect of band filling in

silicon and TiO_2. For silicon, we found a linear dependence of the plasma frequency on carrier density over a wide range of excitation fluences, which indicates that the effective mass is not varying with increasing density[29]. This is expected, since silicon has a multivalley band minimum and band filling requires extremely high carrier densities and associated excitation fluences. The band structure of TiO_2, in contrast, is non-degenerate. At high excitation fluences, we found indeed a non-linear dependence of the plasma frequency with carrier density in TiO_2, which was attributed to band filling[13]. This non-linearity was only observed at carrier densities exceeding 10^{25} m^{-3}). In the THz experiments reported here, the carrier densities were much lower (typically $\sim 10^{23}$ m^{-3}), so that effects due to band filling are not expected. Furthermore, PbS and PbSe have a multi-degenerate energy structure as a result of which band filling is not expected to take place until very high excitation fluences; in the experiment reported here, care was taken to remain in the low-fluence excitation limit. That band filling does not play a role for the experiment reported here, is confirmed by the experimental observation that the THz modulation (which is proportional to the plasma frequency) simply scaled linearly with the excitation fluence (see Fig. 5.1). This means that we are measuring in a carrier density regime where band filling is not important and that the effective carrier mass does not vary over the investigated fluence range.

5.4 CM factors in bulk PbSe and PbS

In this section, we will determine the CM factors in PbSe and PbS by comparing the magnitude of $\Delta E(t)$ per absorbed photon for various excitation wavelengths. This procedure is less elaborate than determining η via Drude fits of the photoconductivity, but gives the same results, as we will show below. Fig. 5.4(a) shows $\Delta E(t)$ for PbS as a function of fluence for various photon energies. Since $\Delta E(t)$ is proportional to the number of carriers (see justification in previous section and Fig. 5.1), the slopes of the lines in Fig. 5.4(a) directly represent the number of carriers generated per absorbed photon, i.e. the CM factor η. After normalizing to the 800 nm slope, for which we have verified by a Drude fit of the photoconductivity that $\eta = 1$, one finds η for the different photon energies.

Normalization of the 266 nm slope to the 800 nm slope in Fig. 5.4(a) yields a value for η of 3.04, in perfect agreement with determination of η via ω_p^2. This procedure is justified when changes in $\sigma(\omega)$ occur only through a change in ω_p^2, and not by variations in τ_r. For PbS, we have verified that τ_r is indeed constant for a wide range of excitation wavelengths
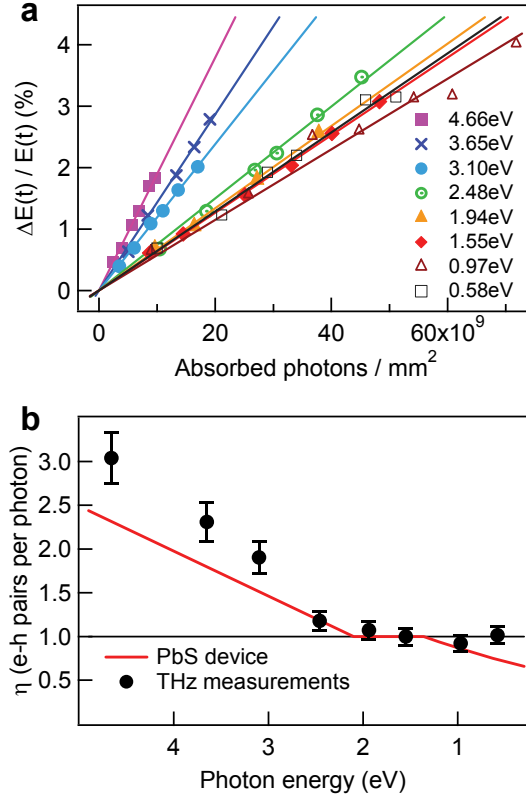
85

Figure 5.4. Determination of the CM factor. a) $\Delta E(t)$ as a function of absorbed photons per unit area for various photon energies for bulk PbS. The slopes of the lines are proportional to the electron-hole pair yield per absorbed photon. b) average electron-hole pair generated per photon for varying photon energies, inferred from (a), compared to a PbS photovoltaic cell[23]. Error bars indicate 95% confidence level.

and excitation fluences. This means that carrier-carrier interactions do not play a significant role, owing to an efficient screening of carrier-carrier interactions, which is consistent with the large dielectric constant of PbS ($\varepsilon = 169$)[34]. Similar results were found for TiO_2, another high dielectric constant material ($\varepsilon = 120$)[29]. For PbSe, the extraction of the photoconductivity spectrum was complicated by the presence of a phonon at 1.25 THz, which is within the spectrum of our THz probe[43]. Therefore, the verification that changes in $\sigma(\omega)$ occur only through a change in ω_p^2 could not be made. However, effects due to carrier-carrier interactions are expected to be smaller for PbSe compared to PbS, given its exceptionally high dielectric constant ($\varepsilon = 210$)[34]. It was assumed that at 1.5 eV (800 nm)

excitation $\eta = 1$ for PbSe. In the case of low dielectric constant materials (e.g. silicon), carrier-carrier interactions are expected to have a large effect on τ_r[29]. For such materials, the CM factor cannot be determined directly from the magnitude of $\Delta E(t)$ per absorbed photon, but should be obtained from the Drude fit of $\sigma(\omega)$.

Fig. 5.4(b) shows η vs. photon energy for PbS, as inferred from our THz measurements, together with the reported values for a PbS photovoltaic cell[23]. The number of additional carriers created by CM is over 1.5 times larger than concluded in Ref. 23. We report a electron-hole pair yield of 3.05 at 4.66eV photon energy for PbS (2.05 additional e-h pairs), whereas Smith et al. report a value of 2.3 for the same photon energy (1.3 additional e-h pairs). The relative change in additional e-h pairs therefore amounts to (2.05-1.3)/1.3= 0.58: The true number of additional carriers created by CM is over 50% larger than determined by Smith. The differences in experimental approach between our work and that of Smith et al. presumably explain the discrepancy between the results. We therefore conclude that to make a definitive comparison between QDs and bulk, the experiments reported here are essential. While the data of Smith reflects the right trend, it underestimates the actual CM factor in bulk PbS presumably due to both details of the sample and the employed approach.

5.5 Comparison between bulk and QDs

The values of η for bulk PbS and PbSe along with literature QD values are given in Fig. 5.5(a) and 5.5(b), respectively. Fig. 5.5 contains a selection of the literature that was published on CM in QDs over the past years. Not all QD reports were included in Fig. 5.5, since it was recently identified that several challenges are associated with reliably measuring CM in QD colloidal suspensions[20,19,22]. These challenges include QD photo-charging (which can be prevented by stirring the sample) and good control over the excitation fluence to prevent multi-photon excitation. Both effects lead to an overestimation of CM factors in QDs. From 2006 onwards, the community became aware of many of these effects. Therefore, we decided to omit early QD reports, since they would not be appropriate for the QD–bulk comparison. From the selected QD references in Fig. 5.5, Refs. 7, 8, 17, and 18 were reported by four different groups after 2006. It is evident in Fig. 5.5 that the CM factors observed in these recent QD reports are lower than or at most equal to our bulk values. This observation indicates that quantum-confinement effects do not result in enhancement of the CM factor. In fact, the CM factor seems to be significantly higher in bulk than in QD suspensions stirred to prevent photo-charging, as reported by Nair et al (2008)[21] and McGuire et al. (2008)[22].
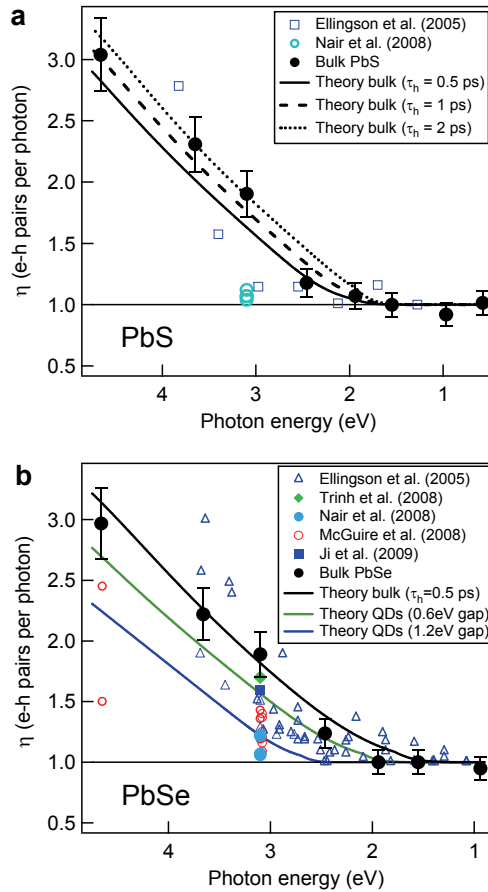
87

Figure 5.5. Comparison of CM in bulk and QDs. Values of η for QDs reported in literature (markers of different colors) compared with bulk results from this work (black dots) for PbS (a) and PbSe (b). Most values of η for QDs lie at or below the bulk factors. Tight binding calculations based on Impact Ionization for a range of phonon-assisted relaxation times (τ_h, dotted lines) yield CM factors that are in good agreement with our experimental results. Colored solid lines represent tight binding calculations for PbSe QDs with 0.6 and 1.2 eV energy gap, for $\tau_h = 0.5$ ps. Error bars indicate 95% confidence level.

In Fig. 5.5, there is significant scatter in the reported CM factors, possibly making a QD-bulk comparison difficult. Surface defects have been invoked to explain the variations in reported QD CM values[21,22]. Within the scatter that surface effects introduce in reported values of CM in QDs, it is important to note for the conclusion of this chapter, that all QD measurements (reported in four papers from four different groups) from 2008 onwards have reported CM factors below the bulk values.

5.6 Mechanism of CM in QDs

To gain insight in the mechanism of CM in bulk and QDs, we collaborated with Christophe Delerue and Guy Allan from the University of Lille who performed tight-binding calculations for CM in bulk material and in QDs. The following model was used in the calculations: the absorption of a high-energy photon in a QD results in the generation of hot carriers (either electrons or holes). The relaxation of these hot carriers to the ground state is modeled as a competition between two relaxation processes, i.e. relaxation via impact ionization and relaxation via 'heat generation'[15,44,45]. In bulk material, the relaxation via 'heat generation' proceeds via sequential emission of phonons, but in QDs heat generation can occur via phonon emission (at high energies), Auger relaxation (see Chapter 3), or energy transfer to ligand vibrations[46], all occurring on an ultrafast (typically sub-picosecond) time scale. In the following discussion, we will refer to these combined relaxation pathways in QDs as 'relaxation via heat generation', characterized by a time constant τ_h. The relative rates of relaxation via impact ionization and relaxation via heat generation determine the final CM factor, which is defined as the number of generated electron-hole pairs (excitons) per absorbed photon.

First, the electronic structure of bulk PbSe and PbSe QDs is calculated using a tight binding approach. For electrons (holes) excited in the conduction (valence) band, the rate of relaxation by impact ionization can be obtained from Fermi's golden rule, requiring the density of initial and final (or bi-exciton states) as input. For varying carrier energies, the calculated density of initial and final states as a function of carrier energy is given in Fig. 5.6. As can be seen in Fig. 5.6, the density of initial states to which carriers can be excited is relatively independent of the energy, whereas the density of final states increases strongly with energy of the hot carrier. The strongly increasing density of final states with carrier energy originates from the fact that there is a much larger number of relaxation pathways via which impact ionization can proceed for carriers at high energies. The fine structure in the QD densities of states arises from the discrete nature of the energy levels at low carrier energies. After having determined the density of initial and final states, the impact ionization rates were calculated using Fermi's golden rule. For higher electron energies, the impact ionization rate increases steeply because of the increased density of final states[15-17]. The impact ionization rate, when summed over all possible final states after relaxation, is observed to strongly depend on the initial energy of the carrier and vanishes when the carrier excess energy (the energy of the carrier with respect to the band edge) is equal to, or less than, the QD gap. Finally, the CM factor was calculated, by modeling the relaxation of hot carriers as a competition between impact ionization (characterized by the above-mentioned energy-dependent rate) and relaxation via heat generation, characterized by a fixed time constant τ_h.
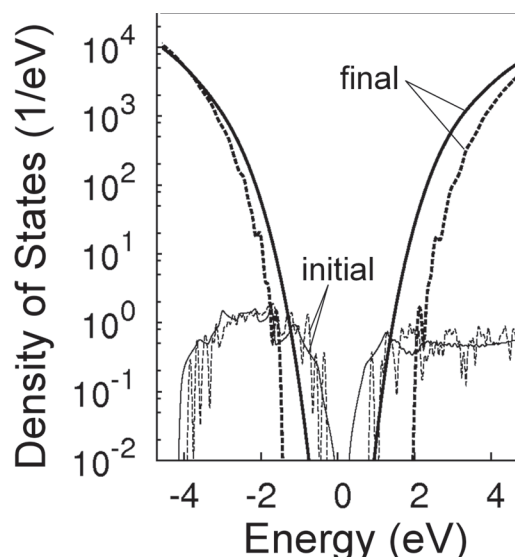
Figure 5.6 Density of States (DOS) per atom versus the energy of the excited carrier for bulk PbSe (solid lines) and PbSe QDs with an energy gap of 1.2 eV (dashed lines). The thin lines represent the DOS of initial states and the thick lines correspond to the DOS of final (bi-exciton) states. The zero of energy corresponds to the top of the bulk valence band.

The results of the calculations for bulk material are given in Fig. 5.5(a) for PbS for different values of τ_h. It is evident that the calculations describe the bulk data accurately for reasonable values of τ_h. In Fig. 5.5(b), the results of the calculations are given for bulk PbSe (black line, $\tau_h = 0.5$ ps) and for two sizes of PbSe QDs (blue and green lines). Also for bulk PbSe, the calculations are in agreement with the experimental values and furthermore, the impact ionization based model can reproduce most of the reports of CM in PbSe QDs. Combining the experimental results of the THz-TDS measurements on bulk PbSe and PbS with the theoretical efforts, we can quantitatively account for CM in both bulk and QDs with impact ionization, without invoking mechanisms such as the coherent superposition of single and multi-exciton wavefunctions[4] or the occurrence of virtual single exciton states[5]. Furthermore, it is evident that the CM factors are at least equal but presumably higher in bulk than in QDs. This observation can be explained by the reduced density of final states in QDs (see Fig. 5.6) leading to lower impact ionization rates in QDs compared to bulk. The conclusion that quantum-confinement does not lead to CM enhancement, in contrast to previous expectations[1,3], can be understood in the light of the present knowledge of three key aspects of dynamic processes and carrier-carrier interactions in bulk and QDs:

- Firstly, the process of CM must compete with alternative intraband relaxation pathways in QDs. Although intraband relaxation was predicted to be slower in quantum-confined QDs than in bulk[1] (phonon-bottleneck), sub-picosecond relaxation can still occur by the transfer of excess energy to ligand vibrations or via an Auger process[24,25]. Recently, it has been demonstrated that these alternative relaxation pathways can be slowed down considerably, potentially making CM much more favorable, for electrons in the 1P level by carefully engineering the QDs[26]. However, the excess energy of 1P electrons is typically insufficient to excite an additional electron over the bandgap. Since the density of states in QDs increases rapidly for higher lying energy levels, the intraband relaxation from these levels is expected to be fast because of the availability of phonon-mediated relaxation channels. Hence, fast phonon relaxation will always compete effectively with CM in QDs.

- Secondly, it has been proposed that the enhanced Coulomb interaction in QDs would lead to higher impact ionization rates[3,22]. However, the impact ionization rate depends on both Coulomb interaction *and* the density of final (or bi-exciton) states[15,21]. In QDs, the density of final states in QDs is reduced because of a discretization of the states. As a result, calculated impact ionization rates are smaller in PbSe QDs than in bulk[15]. Apparently, the increase of Coulomb interactions in QDs is more than neutralized by the lower density of states. This theoretical prediction is confirmed experimentally in Fig. 5.5, where the QD data from 2008 onwards lie clearly below the bulk values.

- Finally, the presence of large amounts of surface defects in QDs might provide an additional competing relaxation channel for hot carriers, possibly reducing the CM factor with respect to bulk. Differences in surface quality may also explain the sample-to-sample variability in CM factors[22] as observed in Fig. 5.5, even for QDs of the same energy gap. We note that, despite the scatter in QD data points, these lie below the bulk values.

The above argumentation on how phonon-relaxation, Coulomb interaction, and surface defects in QDs influence the CM factor is not strictly limited to PbSe and PbS QDs. Intraband relaxation is also known to proceed on ultrafast timescales in other QD materials[24,25]. Additionally, we performed calculations on Si and InAs QDs (not shown in this thesis) and for these materials as well, the increase in Coulombic interaction is more than compensated by the decrease of the Density of States. This indicates that the above argumentation can be extended to other materials beyond PbSe and PbS.

This section will end with a brief discussion on the validity of the chosen graphical representation of the CM factors in Fig. 5.5, i.e. plotting η versus *absolute* photon energy.

In literature, CM yields in QDs have been reported as a function of the ratio of the photon energy and the energy gap ($h\nu/E_{gap}$) to account for variation of the QD energy gap. Indeed, it is true that plotting the number of generated excitons versus the absolute photon energy does not take into account the variations in the bandgap occurring for QDs. However, when considering the physics underlying the CM process for PbSe QDs, i.e. if one is interested in the mechanism of CM and the resulting number of electron-hole pairs, there are two reasons to justify the representation on an absolute energy scale. Firstly, given the bulk mechanism of CM as a competition between phonon emission and impact ionization, one would expect the initial excess energy of the carrier (and the associated density of initial and final states) to be the key parameter determining the CM factor, and not how many times this energy fits the band gap. Secondly, and closely related, it is evident that for the relevant photon energies >3 eV where significant CM occurs, the variation in excess energy of generated hot carriers for QDs of varying sizes is relatively small for a given photon energy, and the CM factor is therefore not limited by limitations due to energy conservation, but rather by variation in the DOS. Such a conclusion would not be apparent from inspection of the CM factor on a relative energy scale. A similar argumentation for using an absolute energy scale has previously been put forward by Nair and Bawendi[18,21].

5.7 Discussion and implications for solar cells

Although the number of generated excitons is smaller in QDs than in the corresponding bulk semiconductor at a given photon energy, this does not directly imply that there is no motivation to use QDs in solar cells for their CM abilities. For photovoltaic applications, the CM factor is not the quantity of interest because the energy of the excitons is not the same in QDs and in the bulk. Rather, a more relevant quantity is the energy efficiency, $\Phi(h\nu)$, defined as the ratio between the total excitonic energy (the number of excitons times the energy gap) and the photon energy $h\nu$. As such, the energy efficiency corresponds to the fraction of the photon energy that is transformed into excitons, i.e. chemical energy, instead of heat after relaxation of the carriers. In Fig. 5.7, we plot the energy efficiency (by definition valued between 0 and 1) including (solid lines) and omitting (dashed lines) CM effects. At the gap energy, the energy efficiency is 1 since no energy is lost via 'heat generation'. For increasing photon energies, the energy efficiency decreases until CM sets in, so that energy efficiency increases again at higher energies. Interestingly, the energy efficiency above the gap is much larger in small QDs than in the bulk. For PbSe QDs with a gap of 1.2 eV, we predict for $\tau_h = 0.5$ ps that the energy efficiency is always larger than 50%. Also, the contribution of CM to the energy efficiency is largest for the smallest QDs.
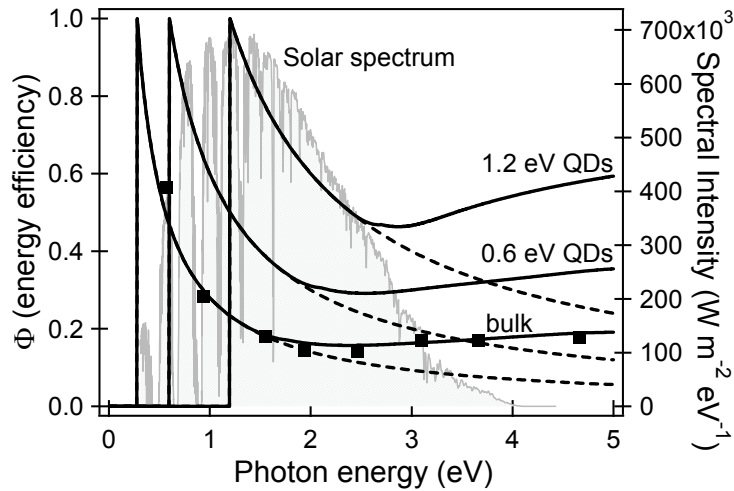
Figure 5.7. Energy efficiency of light absorption versus photon energy hv. Thick solid lines: simulations (τ_h = 0.5 ps) for bulk PbSe (ε_g = 0.28 eV) and for two QDs (ε_g = 0.6 eV and ε_g = 1.2 eV). Dashed lines: simulations in absence of CM, i.e. when excited carriers can only relax by emission of phonons. Black squares: experimental results for bulk PbSe. The grey shaded region corresponds to the ASTM G-173-3 solar spectrum[49].

Even if the number of generated excitons is smaller in QDs than in the bulk, this is more than compensated by the increase of the excitonic energy due to the larger gap in QDs. Therefore strongly confined QDs are energetically relatively efficient for photons with energy above their gap. This conclusion is further confirmed by comparing the CM factor in bulk silicon with PbSe QDs of approximately the same gap (ε_g = 1.2 eV). Figure 5.8 shows that the absolute CM factor of PbSe QDs is clearly superior, the threshold for impact ionization being more than 1 eV lower in energy. Similar results were obtained for comparing bulk silicon with PbS QDs (not shown in this thesis). It is likely a general conclusion that QDs made of a small bandgap semiconductor have a higher CM factor than a bulk semiconductor with the same gap as the QDs. The general reason is that the density of states increases similarly with (photon) energy for different semiconductor materials, but from differently positioned starting points, i.e. the conduction and valence band edge. For a given carrier energy, the density of initial and final states is furthermore larger in bulk PbSe than in bulk silicon because of the eightfold degeneracy of the valence and conduction band extrema[47]. Since the density of final states for impact ionization is similar for QDs and bulk of the same material for photon energies above the energy conservation threshold[15], it can hence be concluded that the density of states at a given energy is always larger in PbSe QDs than in bulk silicon, despite quantum confinement effects. Furthermore, Fig. 5.8 shows that also for bulk silicon the calculations are in excellent agreement with the experimental
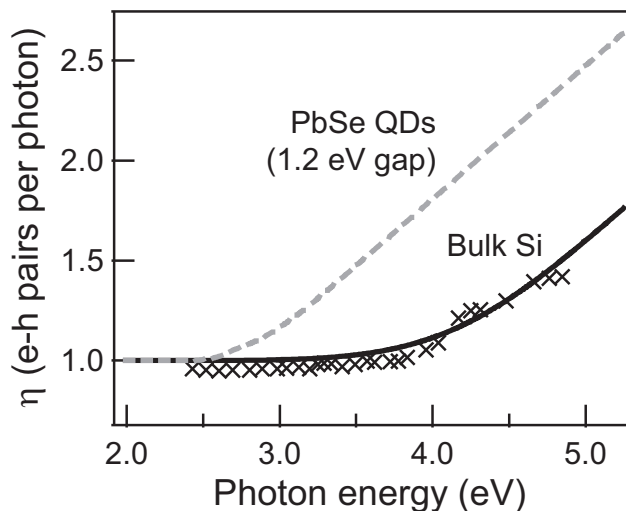
93

Figure 5.8. Number of excitons generated by impact ionization after the absorption of a photon of energy hv. Solid line: simulations for bulk silicon (gap = 1.2 eV). Crosses: experimental values from Ref. 25. Dashed line: simulations for a PbSe QD characterized by a diameter of 3.1 nm and a gap of 1.2 eV. All calculations are performed with τ_h = 0.5 ps.

results[48] for a reasonable value τ_h = 0.5 ps, once more confirming the validity of the methodology of the calculations.

From the above, it is evident that our theoretical considerations can fully account for the higher energy efficiency in QDs compared to bulk (despite the lower CM factor) by means of density of states arguments[15]: In bulk materials, for energy regions relatively close to the band gap, impact ionization is energetically allowed but has a very low probability. This region of reduced impact ionization is smaller in QDs because of the quantum confinement that opens the gap: for QDs the density of states increases sharply above the bandgap towards bulk values (see Fig. 2 in Ref. [15]). Above the threshold for impact ionization, the variation of the impact ionization rate is very large in the case of QDs, and it quickly reaches the bulk values, because the density of states at high energies increasingly resembles that of the bulk. This explains *both* why the absolute CM factor is lower in QDs compared to bulk, but also why the energy efficiency is enhanced for QDs: as soon as carriers in QDs have an energy slightly above the threshold, they have the same probability to relax by impact ionization as in bulk, but the energy of the additionally generated exciton is larger than in bulk, because of opening of the gap due to quantum confinement.

94

Finally, we discuss the implications of our findings on the benefits of CM in QDs for QD solar cells. Despite the observation that 1.2 eV PbSe QDs have a higher CM factor than bulk silicon, the added value of CM for photovoltaics seems limited. This is demonstrated in Table 5.1, where the calculated energy efficiency is averaged for the solar spectrum. The values for the averaged energy efficiency, Φ^*, are obtained by multiplying the energy-dependent energy efficiencies in Fig. 5.7 with the unconcentrated ASTM G-173-3 reference solar spectrum[49] via the following formula:

$$\Phi^* = \frac{\int I(h\nu) \cdot \Phi(h\nu) \cdot d(h\nu)}{\int I(h\nu) \cdot d(h\nu)} \tag{5.1}$$

where $I(h\nu)$ is the energy-dependent spectral intensity of solar light. We assume that each photon with energy above the gap is absorbed, and that each generated carrier contributes to the photocurrent at the maximum voltage (not true for an operating solar cell). The absolute increase in the averaged energy efficiency induced by CM is 9% for bulk PbSe (last column in Table 5.1), but such small gap devices are inherently inefficient. For a realistic gap of a photovoltaic device (~ 1.2 eV), the absolute CM-related gain in the light to current conversion efficiency is limited to 2% when using PbSe QDs. This relatively small value is due to the fact that most of the photon flux in the solar spectrum is below the CM threshold (see Fig. 5.7) which is, for example, positioned at 2.5 eV for 1.2 eV PbSe QDs (Fig. 5.8). Furthermore, it might be challenging to harvest the additional carriers from the 1.2 eV PbSe QDs because of the short lifetime (~ 50 -100 ps) of the bi-exciton state in QDs[50]. Therefore, the benefit of CM in QD based photovoltaics seems minor, in spite of the relatively high energy efficiency of CM in PbSe QDs.

Gap (eV)	Without CM	With CM	Ratio
0.28	0.199	0.217	1.09
0.60	0.381	0.400	1.05
1.20	0.476	0.485	1.02

Table 5.1: Energy efficiency integrated over, and weighted with, the solar spectrum. This calculation ($\tau_h = 0.5$ ps) was done for bulk PbSe ($\varepsilon_g = 0.28$ eV) and for two QDs ($\varepsilon_g = 0.6$ eV and $\varepsilon_g = 1.2$ eV) under solar illumination, in presence or in absence of CM. The last column is the ratio between the third and second column, representing the increase of the averaged energy efficiency due to CM.

5.8 Conclusions

In conclusion, we have determined the CM factors (number of generated excitons per absorbed photon) in bulk PbSe and PbS for a range of excitation wavelengths using THz-TDS measurements. Our experimental efforts demonstrate that the CM factor in the bulk semiconductor is at least equal to but presumably larger than the CM factor in QDs. This observation is corroborated by tight-binding calculations. Our experimental and theoretical observations are consistent with a scenario where in both QDs and bulk, CM is governed by impact ionization, the rate of which is reduced by quantum confinement due to a reduction of the density of states. Although quantum-confinement effects do not result in higher CM factors, the energy efficiency (relative fraction of the photon energy that is converted into excitons) is higher in QDs. In spite of the higher energy efficiency in QDs, the gain in efficiency for QD-based solar cells resulting from CM is small: the benefit of CM is significant only for photons of UV frequencies, which constitute a small fraction of the solar spectrum.

References

(1)   Nozik, A. J. *Physica E* **2002**, *14*, 115-120.
(2)   Landsberg, P. T. *Recombination in Semiconductors*; Cambridge University Press, 2003.
(3)   Schaller, R. D.; Klimov, V. I. *Phys. Rev. Lett.* **2004**, *92*.
(4)   Klimov, V. I. *Ann. Rev. Phys. Chem.* **2007**, *58*, 635-673.
(5)   Ellingson, R. J.; Beard, M. C.; Johnson, J. C.; Yu, P. R.; Micic, O. I.; Nozik, A. J.; Shabaev, A.; Efros, A. L. *Nano Lett.* **2005**, *5*, 865-871.
(6)   Schaller, R. D.; Agranovich, V. M.; Klimov, V. I. *Nature Phys.* **2005**, *1*, 189-194.
(7)   Schaller, R. D.; Sykora, M.; Pietryga, J. M.; Klimov, V. I. *Nano Lett.* **2006**, *6*, 424-429.
(8)   Trinh, M. T.; Houtepen, A. J.; Schins, J. M.; Hanrath, T.; Piris, J.; Knulst, W.; Goossens, A.; Siebbeles, L. D. A. *Nano Lett.* **2008**, *8*, 1713-1718.
(9)   Ji, M.; Park, S.; Connor, S. T.; Mokari, T.; Cui, Y.; Gaffney, K. J. *Nano Lett.* **2009**, *9*, 1217-1222.
(10)   Murphy, J. E.; Beard, M. C.; Norman, A. G.; Ahrenkiel, S. P.; Johnson, J. C.; Yu, P. R.; Micic, O. I.; Ellingson, R. J.; Nozik, A. J. *J. Am. Chem. Soc.* **2006**, *128*, 3241-3247.
(11)   Schaller, R. D.; Petruska, M. A.; Klimov, V. I. *Appl. Phys. Lett.* **2005**, *87*, 253102.
(12)   Beard, M. C.; Knutsen, K. P.; Yu, P.; Luther, J. M.; Song, Q.; Metzger, W. K.; Ellingson, R. J.; Nozik, A. J. *Nano Lett.* **2007**, *7*, 2506-2512.
(13)   Pijpers, J. J. H.; Hendry, E.; Milder, M. T. W.; Fanciulli, R.; Savolainen, J.; Herek, J. L.; Vanmaekelbergh, D.; Ruhman, S.; Mocatta, D.; Oron, D.; Aharoni, A.; Banin, U.; Bonn, M. *J. Phys. Chem. C* **2007**, *111*, 4146-4152.
(14)   Schaller, R. D.; Pietryga, J. M.; Klimov, V. I. *Nano Lett.* **2007**, *7*, 3469-3476.
(15)   Allan, G.; Delerue, C. *Phys. Rev. B* **2006**, *73*, 205423-205425.
(16)   Franceschetti, A.; An, J. M.; Zunger, A. *Nano Lett.* **2006**, *6*, 2191-2195.
(17)   Rabani, E.; Baer, R. *Nano Lett.* **2008**, *8*, 4488-4492.
(18)   Nair, G.; Bawendi, M. G. *Phys. Rev. B* **2007**, *76*, 4.

(19)   Pijpers, J. J. H.; Hendry, E.; Milder, M. T. W.; Fanciulli, R.; Savolainen, J.; Herek, J. L.; Vanmaekelbergh, D.; Ruhman, S.; Mocatta, D.; Oron, D.; Aharoni, A.; Banin, U.; Bonn, M. *J. Phys. Chem. C* **2008**, *112*, 4783-4784.

(20)   Ben-Lulu, M.; Mocatta, D.; Bonn, M.; Banin, U.; Ruhman, S. *Nano Lett.* **2008**, *8*, 1207-1211.

(21)   Nair, G.; Geyer, S. M.; Chang, L.-Y.; Bawendi, M. G. *Phys. Ver. B* **2008**, *78*, 125325-125310.

(22)   McGuire, J. A.; Joo, J.; Pietryga, J. M.; Schaller, R. D.; Klimov, V. I. *Acc. Chem.Res.* **2008**, *41*, 1810-1819.

(23)   Smith, A.; Dutton, D. *J. Opt. Soc. Am.* **1958**, *48*, 1007-1009.

(24)   Klimov, V. I.; McBranch, D. W. *Phys. Rev. Lett.* **1998**, *80*, 4028-4031.

(25)   Guyot-Sionnest, P.; Shim, M.; Matranga, C.; Hines, M. *Phys. Rev. B* **1999**, *60*, R2181-R2184.

(26)   Pandey, A.; Guyot-Sionnest, P. *Science* **2008**, *322*, 929-932.

(27)   Jeon, T.-I.; Grischkowsky, D. *Phys. Rev. Lett.* **1997**, *78*, 1106.

(28)   Beard, M. C.; Turner, G. M.; Schmuttenmaer, C. A. *J. Phys. Chem. B* **2002**, *106*, 7146-7159.

(29)   Hendry, E.; Koeberg, M.; Pijpers, J.; Bonn, M. *Phys. Rev. B* **2007**, *75*, 233202.

(30)   Shandalov, M.; Golan, Y. *The European Physical Journal Appl. Phys.* **2003**, *24*, 13-20.

(31)   Osherov, A.; Ezersky, V.; Golan, Y. *J. Crystal Growth* **2007**, *308*, 334-339.

(32)   Osherov, A.; Ezersky, V.; Golan, Y. *Eur. Phys. J. Appl. Phys.* **2007**, *37*, 39-47.

(33)   Osherov, A.; Shandalov, M.; Ezersky, V.; Golan, Y. *J.Crystal Growth* **2007**, *304*, 169-178.

(34)   Madelung, O. *Semiconductors: Data Handbook*, 3rd ed.; Springer Verlag: New York, 2003; Vol. 17.

(35)   Das, V. D.; Bhat, K. S. *Phys. Rev. B* **1989**, *40*, 7696.

(36)   Bube, R. H. *Photoelectronic Properties of Semiconductors*; Cambridge University Press: Cambridge, England, 1992.

(37)   Kanazawa, H.; Adachi, S. *J. Appl. Phys.* **1998**, *83*, 5997-6001.

(38)   Suzuki, N.; Sawai, K.; Adachi, S. *J. Appl. Phys.* **1995**, *77*, 1249-1255.

(39)   Barton, C. F. *J. Appl. Phys.* **1971**, *42*, 445-450.

(40)   Allgaier, R. S.; Scanlon, W. W. *Phys. Rev.* **1958**, *111*, 1029.

(41)   George, J.; Palson, T. I.; Joseph, K. S. *Solid State Comm.* **1986**, *58*, 605-608.

(42)   Spitzer, W. G.; Fan, H. Y. *Phys. Rev.* **1957**, *106*, 882.

(43)   Burkhard, H.; Geick, P.; Kästner, R.; Unkelbach, K. H. *Phys. Stat. Sol. (b)* **1974**, *63*, 89-96.

(44)   Allan, G.; Delerue, C. *Phys. Rev. B* **2008**, 77, 125340.

(45)   Pijpers, J. J. H.; Ulbricht, R.; Tielrooij, K. J.; Osherov, A.; Golan, Y.; Delerue, C.; Allan, G.; Bonn, M. *Nat. Phys.* **2009**, *5*, 811-814.

(46)   Guyot-Sionnest, P.; Wehrenberg, B.; Yu, D. *J. Chem. Phys.* **2005**, *123*.

(47)   Allan, G.; Delerue, C. *Physical Review B* **2004**, *70*.

(48)   Wolf, M.; Brendel, R.; Werner, J. H.; Queisser, H. J. *J. Appl. Phys.* **1998**, *83*, 4213-4221.

(49)   The ASTM G-173-3 Reference Solar Spectra can be found at http://rredc.nrel.gov/solar/spectra/am1.5/.

(50)   Klimov, V. I.; McGuire, J. A.; Schaller, R. D.; Rupasov, V. I. *Phys. Rev. B* **2008**, *77*, 195324-195335.

Chapter 6: Carrier extraction from QDs

6.1 Background

As discussed in the previous chapters, QDs are promising as light-absorbing materials in future solar cells, because of their excellent optical properties (high extinction coefficients, size-tunable energy gap, etc.) and their special carrier recombination and relaxation characteristics. At present, QD-based solar cells are far from being employed on a large scale, because of several technical and scientific challenges. One particular issue regarding the use of QDs as light absorbing materials is that photo-generated carriers are confined in the small QD volume, in contrast to bulk material where carriers can move freely towards external circuits after photo-generation. Therefore, QD solar cells will only work if extraction of carriers from the QDs into an external circuit can be achieved with minimum losses, both in terms of the fraction of injected carriers and the energetic efficiency of the injection process. A widely studied approach to extract carriers from QDs is to attach the QDs to a mesoporous oxide matrix that is immersed in an electrolyte solution[1-4]. In this concept, light is selectively absorbed by the QDs and electrons are injected from the QDs into the oxide matrix, which serves as photoanode, and the remaining positively charged QD is reduced by a suitable redox couple in the electrolyte. The oxidized redox species migrates towards the photocathode, where it is reduced by the electrons that re-enter the system via the external circuit. This configuration is analogous to the so-called Grätzel cell[5], the only difference being that the dye molecules are replaced by QDs. The schematic layout of a QD-sensitized Grätzel cell is given in Fig. 6.1.
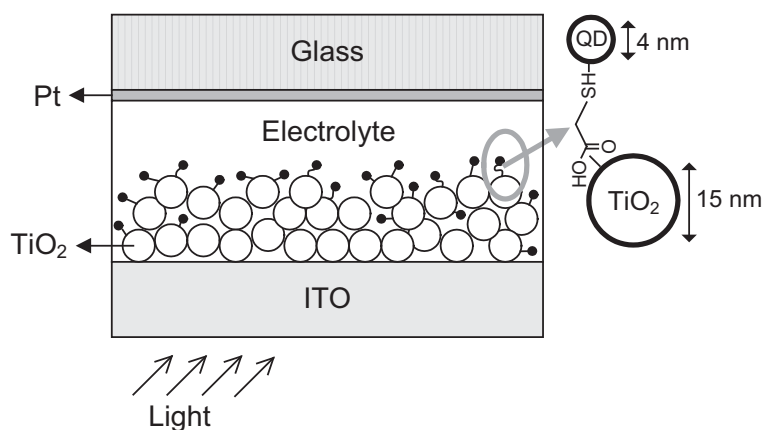

Figure 6.1 Schematic layout of a QD sensitized solar cell based on a TiO_2 anode

For efficient extraction of charges from QDs, it is obvious that the dynamics of charge extraction should be faster than e.g. radiative recombination. Several factors influence the dynamics of charge extraction within a QD-sensitized Solar Cell (QDSSC). First of all, electron injection from the QDs into the oxide is only possible when the conduction energy levels of the QDs have higher energies than the conduction band edge of the electron-accepting oxide material[6]. Energy alignment considerations are also crucial for the reduction reaction of the positively charged QDs by the electrolyte: the Fermi level of the redox species should have higher energy than the valence energy levels of the QD. However, the amount of excess energy should be minimized to keep the voltage maximized. Secondly, the dielectric constant of the electrolyte solvent has been demonstrated to strongly influence charge transfer dynamics from QDs to ligand molecules[7]. Thirdly, linking of QDs to the oxide matrix should not be accompanied by the introduction of defect sites that can act as recombination centers[8,9].

Two methods are commonly used to link QDs to oxide films: QDs can be prepared in-situ on the oxide film by Chemical Bath (CB) deposition[3,10-13] or colloidal QDs can be synthesized in a separate synthesis, after which the QDs are attached to the oxide using bifunctional molecules[1,2,14,15]. In this chapter, we investigate (ultrafast) carrier dynamics in PbSe QDs that are coupled to mesoporous TiO_2 and SnO_2 films with the bifunctional molecule Mercapto Propionic Acid (MPA). Using a range of spectroscopic techniques (including TeraHertz time-domain spectroscopy, femtosecond Transient Absorption, and time-resolved luminescence), combined with electron microscopy and current-voltage measurements, we have gained insight on the presence or the absence of electron injection. New insights are obtained on the requirements for (i) energy level alignment for PbSe sensitized oxide anodes and (ii) surface recombination in QD sensitized oxide films, which are of crucial importance for understanding and optimization QD-sensitized solar cells.

6.2 Sample preparation

The PbSe QDs were synthesized inside a nitrogen-purged schlenk line following Ref 16. All chemicals were stored inside a nitrogen-purged glovebox. In a typical synthesis, a stock solution of lead acetate trihydrate (1.95 g) in 6 ml diphenyl ether, 4.5 ml oleic acid, and 24 ml trioctyl phosphine (TOP) was prepared. The lead oleate precursor was prepared by heating the above mixture to > 70°C under vacuum ($<10^{-3}$ mbar) for > 1 h to remove trace amounts of water and acetate; this is crucial for obtaining monodisperse spherical QDs[16]. The solution was allowed to cool to room temperature. Then 11.5 ml of this solution was mixed with a 1.7 ml solution of selenium (1M) in TOP and rapidly injected into diphenyl ether (10 ml) that was preheated to the desired injection temperature. Typically, the

injection temperature was 190°C, but the temperature dropped upon injection to 130°C and quickly reached the growth temperature of 140°C. The size of the spherical QDs was controlled by the growth time. After a specific growth time the reaction was quenched with a mixture of butanol (20 ml) and methanol (10 ml). The crude products were cleaned by centrifugation and redissolution in toluene, were washed once more using a small volume of methanol and were finally dispersed in toluene. The TEM images of 5.65 nm PbSe QDs in Fig. 6.2 illustrate that the size dispersion of the synthesized QDs was excellent.
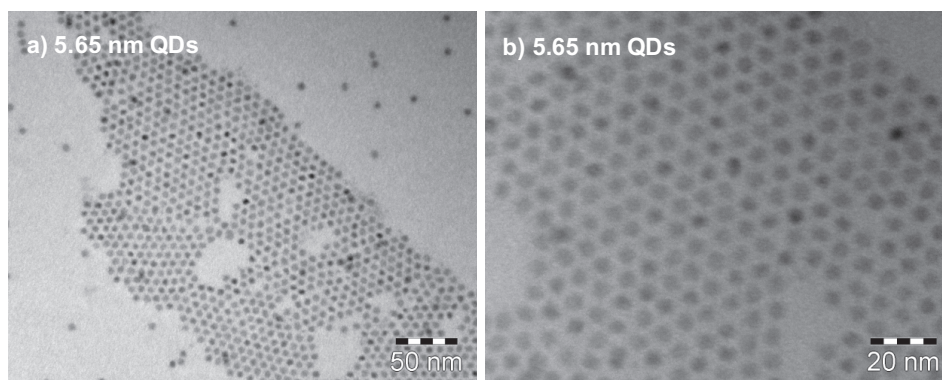

Figure 6.2 Transmission electron micrographs of 5.65 ± 0.47 nm PbSe QDs.

Mesoporous TiO_2 and SnO_2 films were prepared by spreading out viscous dispersions of colloidal TiO_2 and SnO_2 particles on a substrate. The films were deposited on substrates of fused silica (LG Optical Ltd.) for ultrafast spectroscopy studies and on indium-doped tin oxide (ITO) for the fabrication of solar cells. For preparation of the TiO_2 film, an ethanol based paste containing 15 nm TiO_2 particles was purchased from Solaronix (T-LALT). SnO_2 pastes were prepared by dispersing SnO_2 powder (Aldrich, average particle size < 100 nm) in an ethanol solution containing NH_4OH (added to stabilize the colloidal suspension of SnO_2 particles). After spreading out the paste, the film was dried at 115°C for 30 minutes and subsequently annealed in air at 450°C for 2 hours. The annealed films were stored at 70°C and subsequently dipped in a solution of acetonitrile containing MPA for ~ 5 hours. The carboxylic acid group of the MPA interacts strongly with the positively charged surface of TiO_2, resulting in a hydrolysis-condensation reaction[14]. As a result of functionalization with MPA, the thiol groups of the MPA capped TiO_2 nanoparticles are oriented outwards for coupling with the PbSe QDs. After immersion in the MPA-solution, the films were washed thoroughly with acetonitrile and toluene to remove the excess MPA and immersed in a suspension of PbSe QDs in toluene.

6.3 TEM characterization of QD-sensitized TiO_2

Before doing spectroscopic measurements on QD-sensitized oxide films, we first prepared PbSe-sensitized colloidal TiO_2 nanoparticles to visualize QD-linking with TEM imaging. For the preparation of sensitized colloidal TiO_2, 0.05 g of TiO_2 paste was dissolved in 2 ml ethanol, after which 100 μl of MPA was added into the TiO_2 suspension. The excess MPA and the ethanol were removed after centrifugation of the suspension, and the resulting powder was resuspended in toluene. Finally, PbSe QDs were added to the functionalized TiO_2 suspension and the solution was stirred for several hours. After dipping a TEM grid briefly in the suspension, the resulting product was studied by transmission electron microscopy (TEM, Fei Tecnai 12 FEG).
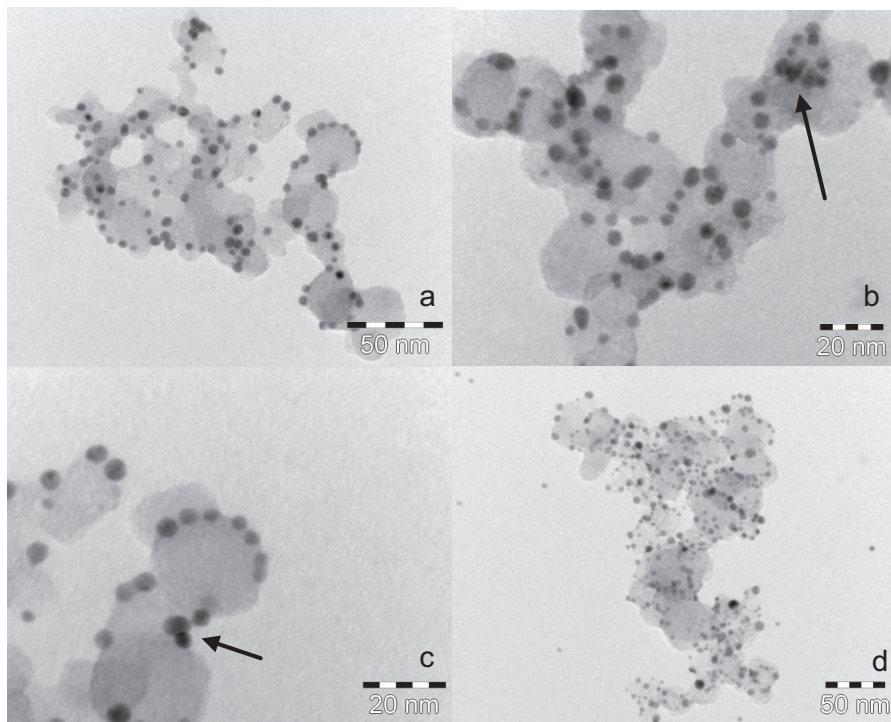

Figure 6.3 Transmission electron micrographs of colloidal TiO_2 particles to which PbSe QDs are linked using MPA. Most QDs are attached on isolated locations at the TiO_2 surface, but clustering of QDs is also occurring, as indicated by the arrows.

Fig. 6.3 shows transmission electron micrographs of colloidal TiO_2 particles that are sensitized with 5.65 nm PbSe QDs (energy gap of 0.77 eV). Clearly, the QDs are in close contact with the TiO_2 particles. As a result of the linking procedure, the QD size dispersion

has become broader, as can be concluded from a comparison with TEM images of isolated QDs (see Fig. 6.1). This broadening of the size dispersion of linked PbSe QDs is probably caused by partial dissolution of the QDs resulting from interaction with MPA. Nonetheless, the shape of the QDs remained spherical. The TEM images in Figure 6.3 indicate that, although the majority of the QDs are isolated on the TiO_2 surface, clustering of QDs also occurs (indicated by the arrows). These clustered QDs can act as centers of carrier recombination, as will be argued in the discussion of the THz-TDS data.

6.4 Optical measurements

First, we characterized the optical properties of TiO_2-MPA-PbSe films. Optical absorption spectra were recorded on a Perkin–Elmer Lambda 950 UV/Vis spectrophotometer and emission spectra were acquired on a Edinburgh Instruments F900 spectrofluorometer, using a 450 W xenon lamp as the excitation source. The emitted light was detected by a fast Hamamatsu photomultiplier tube (R5509-72). Fig. 6.4(a) shows the absorption spectrum (black solid line) and luminescence spectrum (dashed line) of a TiO_2-MPA-PbSe sample, together with the absorption spectrum of isolated PbSe QDs in toluene (grey solid line). In the example of Fig. 6.4(a), the size of the used PbSe QDs was 4.2 nm (as determined from TEM images of unlinked QDs). The distinct 1S absorption peak at 1475 nm in Fig. 6.4(a) is similar (although slightly redshifted) to the absorption characteristics of a QD suspension in toluene, indicating that quantum confinement is preserved after linking to TiO_2. The background in the TiO_2-MPA-PbSe absorption spectrum in Fig. 6.4(a) is caused by light scattered from the nanoporous TiO_2 film.

To achieve electron injection from QDs into oxide materials, the energy of photo-excited electrons in the $1S_e$ QD level should exceed the energy of the oxide conduction band edge. This condition is fulfilled for the TiO_2-CdSe system, where multiple experimental reports have demonstrated efficient electron injection[1,15,17,18]. Theoretical modeling of the position of PbSe QD energy levels versus the TiO_2 conduction band edge predicts that the $1S_e$ level for a wide range of PbSe QD sizes always lies below the TiO_2 conduction band edge[14], making electron injection from PbSe QDs into TiO_2 energetically unfavorable. However, predicting the absolute values of QD energy levels is challenging, since it has been shown that dipole moments on the QDs, induced by local effects like molecular surroundings, can strongly shift the QD energy levels[12]. Furthermore, a recent experimental report has claimed slow injection from PbSe QDs into TiO_2 nanorods on a nanosecond timescale, based on time-resolved luminescence measurements[19].
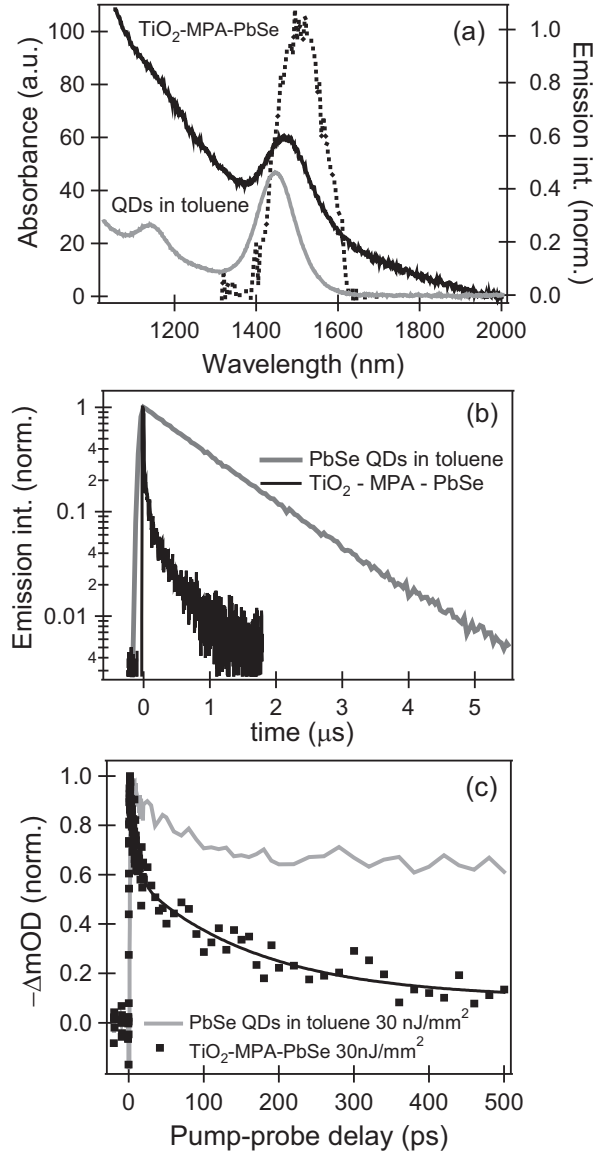
Figure 6.4 a). Absorption spectrum of 4.2 nm PbSe QDs in toluene (grey solid line) and a TiO$_2$-MPA-PbSe sample (black solid line) The dashed line is the luminescence spectrum of the TiO$_2$-MPA-PbSe sample. b). Decay of the luminescence for the same PbSe QDs in toluene (grey line), which can be fitted with an exponential decay using a time constant of ~ 1.0 µs. The black line corresponds to the luminescence decay of the TiO$_2$-MPA-PbSe sample. c) Normalized decay dynamics of TA measurements for 4.2 nm PbSe QDs in toluene (grey solid line) and for the TiO$_2$-MPA-PbSe sample (black dots). For both experiments, an 800 nm excitation fluence of 30 nJ/mm^2 was used and the photo-induced bleaching of the 1S transition was probed using 1500 nm pulses.

104

To determine whether electron injection from PbSe QDs into TiO_2 occurs, luminescence decay curves were obtained in the same Edinburgh set-up by using a LPD300 tunable dye laser as the excitation source (λ_{ex} = 720 nm, 10 ns pulse width, 10 Hz repetition rate, a LPX100 excimer laser was used as the pump laser) and analyzing the decay of the PMT signal with a Tektronix 2430 Digital Oscilloscope. Fig. 6.4(b) shows the decay of the luminescence for the 4.2 nm PbSe QDs in toluene (grey line), which can be fitted with an exponential decay using a time constant of $\sim$ 1.0 μs. The black line in Fig. 6.4(b) corresponds to the luminescence decay of the TiO_2-MPA-PbSe sample: clearly, the luminescence is strongly quenched as a result of linking. In some reports, quenching of the QD luminescence in QD-sensitized oxide films has been attributed to carrier injection[19,20]. If this interpretation would be correct, the data in Fig. 6.4(b) suggests that electron injection occurs on a nanosecond timescale.

Next, we performed TA measurements to monitor carrier population dynamics within the attached 4.2 nm PbSe QDs in a TiO_2-MPA-PbSe sample. For this purpose, we selectively excited the QDs with an 800 nm (1.55 eV) pump beam (the bandgap of TiO_2 is $\sim$ 3.2 eV) and we measured the pump-induced bleaching of the lowest-energy 1S absorption feature using a 1500 nm probe beam. We used a low 800 nm excitation fluence (30 nJ/mm^2) to ensure that no more than one photon is absorbed per QD. Fig. 6.4(c) gives a comparison between the decay of the pump-induced bleach for PbSe QDs in toluene (grey solid line) and the TiO_2-MPA-PbSe sample (black dots). Clearly, there is a fast decay component in the TiO_2-MPA-PbSe data that is absent for the QDs in toluene. The presence of such fast (picosecond) decay component in TA data of linked QDs has been attributed to electron injection in several reports, which was corroborated by the measurements of photo-currents[1,17].

From the fast decay components in Figs. 6.4(b) and 6.4(c), one might be tempted to conclude that there is electron injection from PbSe QDs into TiO_2. However, the different timescales that one might associate with injection observed in TA and time-resolved luminescence measurements on the same TiO_2-MPA-PbSe sample are not consistent with a simple injection process. Also in literature, there is a discrepancy in reported timescales of injection from TA measurements (picosecond timescale)[1,10,17] and time-resolved luminescence measurements (nanosecond timescale)[14,19]. An explanation for these inconsistent observations is that fast decay components in time-resolved optical measurements on QD-sensitized oxide films can also be fully explained by recombination in defect centers at the oxide-QD interface. This means that the fast decay components in the time-resolved optical measurements on TiO_2-MPA-PbSe films in Figs. 6.4(b) and 6.4(c) can be attributed to both carrier injection *and* to recombination in defect centers. Hence, optical measurements alone do not give definitive proof of electron injection.

6.5 THz-TDS measurements

To gain more insight in the carrier dynamics at the oxide-QD interface, we performed complementary THz measurements on the same TiO_2-MPA-PbSe samples. Similar to the TA experiment, we used THz-TDS in the pump-probe configuration, in which 800 nm pulses were used for selective excitation of the PbSe QDs in the TiO_2-MPA-PbSe samples. The probe beam, however, comprised a frequency domain of 0.2 – 2 THz[21]. A frequency of 1 THz corresponds to a photon energy of 4 meV, which is well below the electronic transitions of bulk and quantum-confined semiconductors. Rather, the oscillating electric field of the THz probe interacts strongly with free charge carriers. Firstly, changes in the amplitude of the transmitted THz transmission are related to *real* conductivity, associated with the absorption of THz light. The real conductivity gives information about the number and mobility of free carriers in semiconductors, since THz light is strongly absorbed by free carriers. Absorption of THz light occurs since the THz field accelerates free carriers in a material, as a result of which part of the energy of the THz pulse is converted into kinetic energy of carriers. In addition, the phase-shift of the transmitted THz pulse through a sample is related to the *imaginary* conductivity, which is related to the (photo-induced) refractive index of a material. Furthermore, the shape of the complex frequency dependent conductivity in the THz window gives information about the nature of carrier conductivity in a material. As such, THz-TDS has been widely used to probe the carrier density and carrier mobility in bulk semiconductors[22,23], mesoporous semiconducting oxides[24,25], semiconductor QDs[26-28], and QD solids[29].
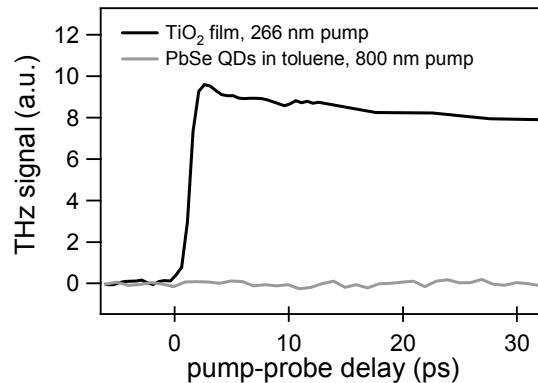
Figure 6.5 Comparison of the imaginary THz response for isolated PbSe QDs in toluene (grey line) and the real THz response for a directly excited unloaded TiO_2 film (black line). The unloaded film was directly excited with 266 nm pulses and the PbSe QDs sample was excited with comparable 800 nm fluences. Clearly, the (imaginary) THz signal arising from isolated QDs is negligible compared to the (real) signal from carriers in the TiO_2 film.

For the TiO_2-MPA-PbSe sample, the THz probe can interact with two types of carriers: immediately after (selective) photoexcitation of the QDs, excitons are present in the PbSe QDs. While the THz field cannot accelerate neutrally charged excitons (no absorption of THz light), the THz field will only experience a phase-shift owing to the presence of polarizable excitons[26,28]: the real conductivity is zero (no absorption of THz light) and the imaginary conductivity is negative and decreasing with frequency[26,28] (see also Chapter 2). The other possible response is due to free carriers in the TiO_2-MPA-PbSe film. Although the microscopic conductivity of free carriers in nanostructured semiconductors has a Drude-like behavior, the macroscopic conductivity at THz frequencies deviates significantly from the Drude behavior because of local field effects. The macroscopic conductivity of mesoporous films can be described using effective medium theory[24], and is characterized by a positive real conductivity (increasing with frequency) and a negative imaginary conductivity (decreasing with frequency)[24]. Given the fact that exciton polarizability in PbSe is exceptionally low[28] due to the high dielectric constant of PbSe ($\varepsilon = 215$)[30], the THz response is expected to be dominated by real conductivity resulting from free carriers in the TiO_2-MPA-PbSe film. This expectation was confirmed by comparing the imaginary THz response for isolated PbSe QDs, and the real THz response for an unloaded TiO_2 film under similar excitation densities (see Fig. 6.5): the (imaginary) THz signal resulting from PbSe QDs is negligible compared to (real) response of free carriers in TiO_2. Hence, the THz dynamics were assumed to directly reflect the dynamics of mobile carriers in the oxide films.

Fig. 6.6 shows $\Delta E(t)$, which is the change in the transmission of the THz field due to photo-excitation (E_{trans} - E_{trans}^{exc}, corresponding to the real conductivity), for the TiO_2-MPA-PbSe sample, following photo-excitation with 800 nm pulses. As in the TA experiment, 4.2 nm PbSe QDs were used but the 800 nm excitation fluence was ~ 500 nJ/mm^2. This fluence was higher than used in the TA measurements of Fig. 6.4(c), but we verified that the general shape of the THz response remained the same for lower excitation fluences (85 nJ/mm^2 trace in Fig. 6.6). To characterize the nature of the carrier conductivity in the TiO_2-MPA-PbSe film, we inferred the complex conductivity from the time-domain traces of the transmitted THz field through the unexcited sample (reference trace) and the excited sample, following the procedure in Reference[31]. The complex conductivity, measured 30 ps after photo-excitation, is given in Fig. 6.7. The shape of the extracted conductivity is indicative of the conductivity of free carriers in nanostructured semiconducting materials[24,32], as indicated by positive real conductivity (increasing with frequency) *and* the negative imaginary conductivity. Therefore, Fig. 6.7 confirms that the real THz conductivity signal in Fig. 6.6 originates from free carriers in the nanostructured TiO_2-MPA-PbSe film.
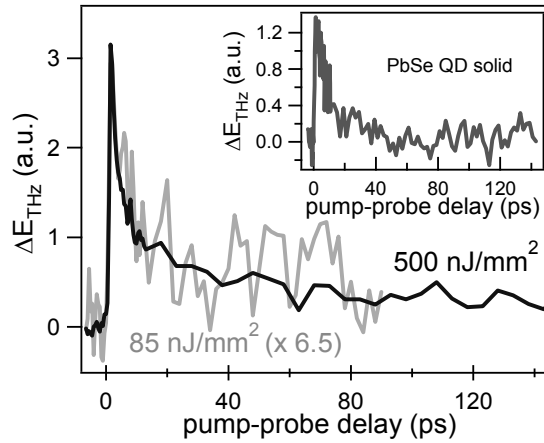
Figure 6.6 THz-TDS signals for the TiO_2-MPA-PbSe sample (4.2 nm PbSe QDs), following photo-excitation with 800 nm pulses. The similarity between results at different fluences (black trace: 500 nJ/mm^2 and grey trace: 85 nJ/mm^2), apart from a scaling factor, reveals that effects due to multi-photon absorption are negligible. The real conductivity represented by the THz signals does not originate from free carriers in TiO_2 but is likely due to mobile carriers in QD clusters at the TiO_2 surface, as explained in the text. The inset shows the THz signal of a PbSe QD solid on fused silica for an 800 nm excitation fluence of 500 nJ/mm^2.
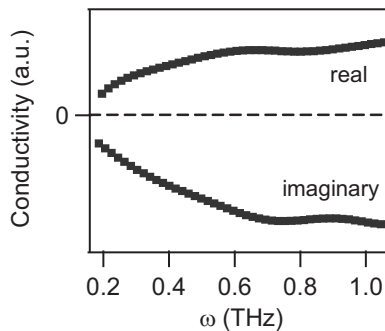

Figure 6.7 Complex conductivity of the TiO_2-MPA-PbSe film, measured 30 ps after photo-excitation with 800 nm light. The shape of the conductivity is characteristic for the presence of free carriers in nanostructured semiconducting materials[24,32].

Despite the clear observation of real conductivity, the THz signal in Fig. 6.6 is not indicative of electron injection in TiO_2. The reason is that, in case the THz signal in Fig. 6.6 would represent the population of free carriers in TiO_2, the fast risetime of the THz signal (~ 1 ps) would be a measure for timescale of injection. However, such fast injection is not in agreement with the TA and time-resolved fluorescence results presented in section 6.4, nor with reports on injection from CdSe[1,17] or PbS[14] QDs. Furthermore, the rise of the THz

signal was similarly fast for TiO_2 films that were sensitized with PbSe QD of sizes ranging from 3.2 – 7 nm, in contrast to the observation of size-dependent injection dynamics for the TiO_2-MPA-CdSe system[17]. Another indication that the THz signal in Fig. 6.6 does not originate from electrons in TiO_2 is that the THz signal decays within tens of picoseconds, whereas the lifetime of injected carriers in mesoporous oxides is usually much longer (>100's ps), as demonstrated by THz measurements on dye-sensitized TiO_2 films, where electrons are injected from excited dyes into the TiO_2 (see Fig. 6.8).
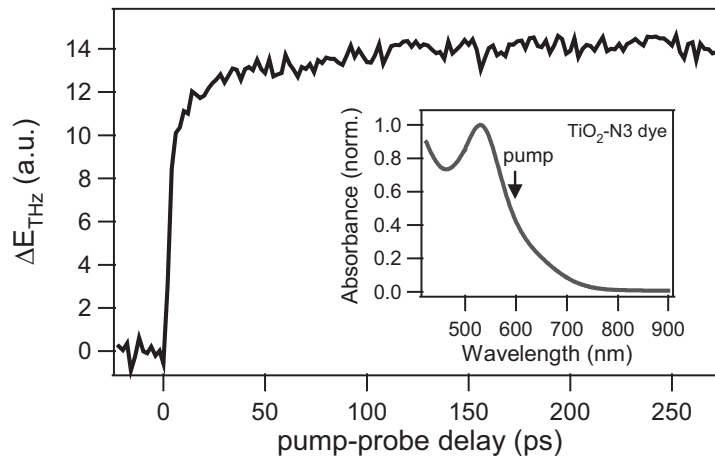

Figure 6.8 Real THz conductivity for a mesoporous TiO_2 film, sensitized with ruthenium based dyes (N3-dye, purchased from Solaronix). The inset shows the absorption spectrum of the dye-sensitized TiO_2 film. The dyes were selectively excited with 590 nm light (2 μJ/mm² fluence) and probed with THz light. The THz signal corresponds to the amount of injected electrons from the dye into the TiO_2 conduction band edge and hence reflects injection dynamics. Clearly, the lifetime of injected electrons in TiO_2 is longer than the timescale of the measurement.

Summarizing, one might be tempted to conclude from separate optical measurements on TiO_2-MPA-PbSe that injection from PbSe QDs into TiO_2 takes place, but the timescales of injection concluded from TA and time-resolved luminescence measurements are not consistent. THz measurements indicate the presence of real conductivity in the TiO_2-MPA-PbSe sample, but the rise *and* decay of the THz signal are not consistent with injection. These seemingly conflicting observations can be explained by the presence of QD clusters at the oxide-QD interface, as it is known that carriers in coupled QDs can give rise to real conductivity, provided that dot-to-dot coupling is sufficiently strong[33,34]. The presence of such clusters is apparent from the TEM images in Fig. 6.3, and we therefore attribute the THz signal in Fig. 6.6 to hopping of carriers in QD clusters at the TiO_2 surface: as can be seen in Fig. 6.3, most of the PbSe QDs are present at isolated locations on the TiO_2 surface, but some QDs form clusters, in which the dot-to-dot distance is small. It is conceivable that

the presence of mobile carriers in QD clusters at the TiO_2 surface can explain the THz response in Fig. 6.6: such free carriers would be present directly after photo-excitation, explaining the fast rise of the THz signal, and the risetime would not depend on the size of the PbSe QDs. The decay of the THz signal is likely caused by recombination of carriers in defect centers within the QD clusters, which typically occurs within tens of picoseconds. The time scale of the decay of the THz signal is similar to that of the decay in the TA measurements in Fig. 6.4(c), suggesting that the decay of the TA signal also originates from trapping in QD clusters. The luminescence signal decays on much longer timescales (Fig. 6.4(b)) and we suggest that this decay is both caused by trapping at the QD-oxide interface and by energy transfer between QDs in the QD clusters[35,36].

To verify the hypothesis that the real conductivity in Fig. 6.6 is caused by carriers in QD clusters, and not by injection, we dropcasted a QD solid film on a fused silica substrate and measured the THz response (inset Fig. 6.6). The wide bandgap of fused silica (~ 9 eV) ensures that charge injection from PbSe QDs into fused silica is energetically not allowed; hence any THz signal will originate directly from carriers within the QD solid. Clearly the THz response from the QD solid closely resembles that of the TiO_2-MPA-PbSe sample. This indicates once more that the THz data of the TiO_2-MPA-PbSe sample in Fig. 6.6 does not originate from mobile electrons in TiO_2, but from mobile carriers in PbSe QD clusters.

A control experiment to verify the QD cluster hypothesis is to do THz measurements on a sample where electron injection is expected. Therefore, we did THz measurements on a SnO_2-MPA-PbSe film, because charge injection from small PbSe QDs into SnO_2 should
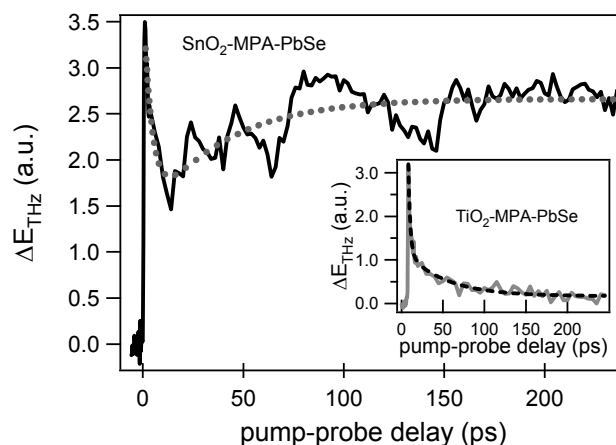
Figure 6.9. THz-TDS signal for the SnO_2-MPA-PbSe sample (4.2 nm PbSe QDs), following photo-excitation with 800 nm pulses (500 nJ/mm^2). As for the TiO_2-MPA-PbSe sample (inset), there is a quasi-instantaneous rise of the signal and a subsequent decay within tens of picoseconds. For the SnO_2-MPA-PbSe sample, there is an additional long-lived ingrowth of the THz signal, which originates from injected electrons in SnO_2. The dashed lines are fits to the data, yielding a timescale for electron injection of 40 ± 10 ps.

110

be possible since the energy of the SnO_2 conduction band edge is roughly 0.5 eV lower than the TiO_2 band edge[14,37]. Fig. 6.9 shows the THz signal for a SnO_2- MPA-PbSe sample (using 4.2 nm PbSe QDs), following excitation with 500 nJ/mm^2 800 nm pulses. For clarity, the THz response of the TiO_2-MPA-PbSe sample is given once more in the inset of Fig. 6.9 (similar as data in Fig. 6.6). Clearly, both data traces in Figs. 6.6 and 6.9 have a quasi-instantaneous rise of the signal that decays within tens of picoseconds, which we attribute to carrier recombination in QD clusters, as discussed before. For the SnO_2-MPA-PbSe sample, however, there is also an ingrowth of the THz signal on longer timescales, which we attribute to carrier injection. It must be noted that the ingrowth of the signal could not always be reproduced for different SnO_2-PbSe samples, which is possibly due to sample-to-sample variations in surface chemistry that might affect electron injection. However, the difference between the TiO_2- and SnO_2-based samples is another confirmation that charge injection does not occur in the TiO_2-MPA-PbSe system: for this system, the THz signal originates only from mobile carriers in QD clusters and no long-lived signal due to carriers in TiO_2 is observed.

To quantify the timescale of electron injection, we first fitted the TiO_2-MPA-PbSe data in the inset of Fig. 6.9 by a double exponential decay with time constants of 2.5 ± 0.3 ps and 48 ± 5 ps. The SnO_2-MPA-PbSe data was fitted with a fit function that included a double exponential decay and an exponential ingrowth describing the injection process $(A*(1-\exp(-t/\tau_{inj})))$. Fitting the data in Fig. 6.9 with this equation, we found a time constant describing the injection process into SnO_2 of 40 ± 10 ps. These injection dynamics have the same order of magnitude as concluded from TA measurements on the TiO_2-MPA-CdSe system[1,17], but is orders of magnitude faster than concluded from time-resolved luminescence measurements on TiO_2-MPA-PbS[14] and PbSe QDs on TiO_2 nanorods[19].

6.6 A QD-sensitized solar cell

To obtain conclusive evidence for the presence of electron injection in SnO_2-MPA-PbSe films (and the absence of injection in TiO_2-based systems), we performed photocurrent measurements on QD-sensitized solar cells (QDSSC's). The layout of these QDSSC's is shown in Fig. 6.1 and is analogous to a dye-sensitized solar cell[5] (or Grätzel cell). The QD sensitized solar cells were made by preparing functionalized oxide films (similar procedure as above) on a conducting ITO substrate (1 x 1 cm) instead of using fused silica substrates. The QD-sensitized oxide electrode and a Pt-coated counter-electrode were sandwiched in an open cell configuration. The electrolyte is a methoxypropionitrile-based solution containing I^-/I_2 as a redox couple. The cells were investigated in a solar simulator (Wacom) using a 5 kW Xe-lamp (type WXS-300S-50, AM1.5G). We measured the photocurrents of

cells that consisted of a TiO_2 anode (not evident that charge injection is energetically allowed) and compared the response with SnO_2-based solar cell. Fig. 6.10 confirms our interpretation of the THz data in Figs. 6.6 and 6.9: there is a significant short circuit current I_{sc} of ~ 80 μA for the SnO_2-based QDSSC, while I_{sc} for the TiO_2-based cell is zero within the noise of the measurement. This observation confirms the interpretation presented above that there is no injection from PbSe QDs into TiO_2 and that all spectroscopic measurements on the TiO_2-MPA-PbSe system in Figs. 6.4 and 6.6 can be interpreted by carrier migration and recombination within QD clusters.
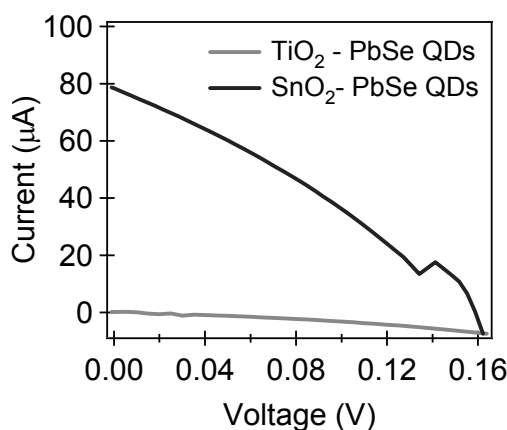

Figure 6.10 Current-Voltage characteristics for PbSe QD-sensitized solar cells based on a SnO_2 anode (black line) and a TiO_2 anode (grey line). There is a significant I_{sc} of ~ 80 μA for the SnO_2-based QDSSC, while the I_{sc} for the TiO_2-based cell is negligible.

6.7 Conclusions

Electron injection from PbSe QDs into mesoporous SnO_2 films has been demonstrated to occur within tens of picoseconds. TeraHertz measurements are excellently suited to directly probe electron injection into oxide materials, since light of THz frequencies probes free carriers in the oxide. Complementary time-resolved luminescence, transient absorption, TeraHertz spectroscopy, and IV-measurements demonstrate conclusively that charge injection from PbSe QDs into TiO_2 does not take place within the range of sizes investigated here (3.2 – 7 nm diameter). Clearly, the alignment of QD conduction levels and the oxide conduction band edge is a crucial factor determining the occurrence of charge injection. Our results illustrate the challenges in the interpretation of spectroscopic data in terms of charge injection, since the signature of charge injection for various spectroscopic techniques is similar to non-radiative recombination at the QD-oxide interface and to

energy transfer within QD clusters. More specific, THz measurements together with TEM imaging demonstrate that there is formation of QD clusters at the oxide surface, in which mobile carriers are formed after photo-excitation. Such QD clusters might lower the QD solar cell efficiency since such mobile carriers can 'find' recombination centers in QD clusters on a timescale of ~ 10 ps.

References

(1)   Robel, I.; Subramanian, V.; Kuno, M.; Kamat, P. V. *J. Am. Chem. Soc.* **2006**, *128*, 2385-2393.
(2)   Leschkies, K. S.; Divakar, R.; Basu, J.; Enache-Pommer, E.; Boercker, J. E.; Carter, C. B.; Kortshagen, U. R.; Norris, D. J.; Aydil, E. S. *Nano Lett.* **2007**, *7*, 1793-1798.
(3)   HyoJoong, L.; Henry, C. L.; Soo-Jin, M.; Peter, C.; Seigo, I.; Saif, A. H.; Tomas, T.; Frank, N.; Thomas, G.; Shaik, M. Z.; Michael, G.; Md. Khaja, N. *Adv. Functional Mater.* **2009**, *19*, 2735-2742.
(4)   Lee, H. J.; Chen, P.; Moon, S.-J.; Sauvage, F. d. r.; Sivula, K.; Bessho, T.; Gamelin, D. R.; Comte, P.; Zakeeruddin, S. M.; Seok, S. I.; Grätzel, M.; Nazeeruddin, M. K. *Langmuir* **2009**, *25*, 7602-7608.
(5)   O'Regan, B.; Gratzel, M. *Nature* **1991**, *353*, 737-740.
(6)   Tachibana, Y.; Akiyama, H. Y.; Ohtsuka, Y.; Torimoto, T.; Kuwabata, S. *Chem. Lett.* **2007**, *36*, 88-89.
(7)   Hyun, B.-R.; Bartnik, A. C.; Lee, J.-K.; Imoto, H.; Sun, L.; Choi, J. J.; Chujo, Y.; Hanrath, T.; Ober, C. K.; Wise, F. W. *Nano Lett.* **2009**, *10*, 318-323.
(8)   Loef, R.; Houtepen, A. J.; Talgorn, E.; Schoonman, J.; Goossens, A. *Nano Lett.* **2009**, *9*, 856-859.
(9)   Tachibana, Y.; Umekita, K.; Otsuka, Y.; Kuwabata, S. *J. Phys. Chem. C* **2009**, *113*, 6852-6858.
(10)   Blackburn, J. L.; Selmarten, D. C.; Nozik, A. J. *J. Phys. Chem. B* **2003**, *107*, 14154-14157.
(11)   Plass, R.; Pelet, S.; Krueger, J.; Gratzel, M.; Bach, U. *J. Phys. Chem.B* **2002**, *106*, 7578-7580.
(12)   Shalom, M.; Ruȉhle, S.; Hod, I.; Yahav, S.; Zaban, A. *J. Am. Chem. Soc.* **2009**, *131*, 9876-9877.
(13)   Yu, P. R.; Zhu, K.; Norman, A. G.; Ferrere, S.; Frank, A. J.; Nozik, A. J. *J. Phys. Chem. B* **2006**, *110*, 25451-25454.
(14)   Hyun, B.-R.; Zhong, Y.-W.; Bartnik, A. C.; Sun, L.; Abruña, H. D.; Wise, F. W.; Goodreau, J. D.; Matthews, J. R.; Leslie, T. M.; Borrelli, N. F. *ACS Nano* **2008**, *2*, 2206-2212.
(15)   Bang, J. H.; Kamat, P. V. *ACS Nano* **2009**, *3*, 1467-1476.
(16)   Houtepen, A. J.; Koole, R.; Vanmaekelbergh, D. L.; Meeldijk, J.; Hickey, S. G. *J. Am. Chem. Soc.* **2006**, *128*, 6792-6793.
(17)   Robel, I.; Kuno, M.; Kamat, P. V. *J. Am. Chem. Soc.* **2007**, *129*, 4136-4137.
(18)   Lee, H. J.; Yum, J.-H.; Leventis, H. C.; Zakeeruddin, S. M.; Haque, S. A.; Chen, P.; Seok, S. I.; Grätzel, M.; Nazeeruddin, M. K. *J. Phys. Chem C* **2008**, *112*, 11600-11608.
(19)   Acharya, K. P.; Alabi, T. R.; Schmall, N.; Hewa-Kasakarage, N. N.; Kirsanova, M.; Nemchinov, A.; Khon, E.; Zamkov, M. *J. Phys. Chem. C* **2009**, *113*, 19531-19535.
(20)   Dibbell, R. S.; Youker, D. G.; Watson, D. F. *J. Phys. Chem. C* **2009**, *113*, 18643-18651.

(21)   Beard, M. C.; Turner, G. M.; Schmuttenmaer, C. A. *J. Phys. Chem. B* **2002**, *106*, 7146-7159.

(22)   Jeon, T.-I.; Grischkowsky, D. *Phys. Rev. Lett.* **1997**, *78*, 1106.

(23)   Pijpers, J. J. H.; Ulbricht, R.; Tielrooij, K. J.; Osherov, A.; Golan, Y.; Delerue, C.; Allan, G.; Bonn, M. *Nat Phys* **2009**, *5*, 811-814.

(24)   Hendry, E.; Koeberg, M.; O'Regan, B.; Bonn, M. *Nano Lett.* **2006**, *6*, 755-759.

(25)   Hendry, E.; Wang, F.; Shan, J.; Heinz, T. F.; Bonn, M. *Phys. Rev. B* **2004**, *69*.

(26)   Wang, F.; Shan, J.; Islam, M. A.; Herman, I. P.; Bonn, M.; Heinz, T. F. *Nature Mater.* **2006**, *5*, 861-864.

(27)   Hendry, E.; Koeberg, M.; Wang, F.; Zhang, H.; Donega, C. d. M.; Vanmaekelbergh, D.; Bonn, M. *Phys. Rev. Lett.* **2006**, *96*, 057408-057404.

(28)   Dakovski, G. L.; Lan, S.; Xia, C.; Shan, J. *J. Phys. Chem. C* **2007**, *111*, 5904-5908.

(29)   Beard, M. C.; Turner, G. M.; Murphy, J. E.; Micic, O. I.; Hanna, M. C.; Nozik, A. J.; Schmuttenmaer, C. A. *Nano Lett.* **2003**, *3*, 1695-1699.

(30)   Madelung, O. *Semiconductors: Data Handbook*, 3rd ed.; Springer Verlag: New York, 2003; Vol. 17.

(31)   Knoesel, E.; Bonn, M.; Shan, J.; Wang, F.; Heinz, T. F. *J. Chem. Phys.* **2004**, *121*, 394-404.

(32)   Nienhuys, H. K.; Sundstrom, V. *Appl. Phys. Lett.* **2005**, *87*.

(33)   Yu, D.; Wang, C. J.; Guyot-Sionnest, P. *Science* **2003**, *300*, 1277-1280.

(34)   Houtepen, A. J.; Kockmann, D.; Vanmaekelbergh, D. l. *Nano Letters* **2008**, *8*, 3516-3520.

(35)   Wuister, S. F.; Koole, R.; Donega, C. D.; Meijerink, A. *J. Phys. Chem. B* **2005**, *109*, 5504-5508.

(36)   Koole, R.; Liljeroth, P.; Donega, C. D.; Vanmaekelbergh, D.; Meijerink, A. *J. Am. Chem. Soc.* **2006**, *128*, 10436-10441.

(37)   Gratzel, M. *Nature* **2001**, *414*, 338-344.

Chapter 7: Charge extraction in complete dye-sensitized solar cells

7.1 Motivation

In many fundamental studies on novel solar cell concepts, model systems are investigated that represent a specific sub-unit of the solar cell. For instance, to gain fundamental insight in Carrier Multiplication in QDs, ultrafast spectroscopic measurements are performed on suspensions of isolated QDs in a solvent (see chapter 4) instead of on QDs embedded in a real solar cell configuration. The reason is that in devices, many physical processes occur that can obscure the process of interest. In model systems, undesired physical processes can – in principle – be suppressed allowing one to focus on the physical process of interest. However, there is always the possibility that when the model system (e.g. the QD) is incorporated in an operating device, fundamental physical processes change as a result of interactions with the device environment.

In the final chapter of this thesis, the effect of the device environment on charge injection is investigated. As explained in Chapter 6, photo-generated carriers can be extracted from QDs by sensitizing mesoporous oxide films with QDs: in this approach, light is selectively absorbed by QDs and electrons are injected from the QDs into the oxide matrix, which serves as photoanode, and the remaining positively charged QDs are reduced by a suitable redox couple in the electrolyte. The oxidized redox species migrates towards the photocathode, where it is reduced by the electrons that re-enter the system via the external circuit. This configuration is analogous to the so-called Grätzel cell[1], the only difference being that the dye molecules are replaced by QDs. In chapter 6, we studied the dynamics of electron injection into a QD-sensitized oxide film that was embedded in an inert environment (N_2, toluene). In this chapter, we will investigate how the dynamics of charge extraction are altered when a *dye*-sensitized film is embedded in an electrolyte solution. The reason for sensitization with dyes instead of QDs is that dye-electrolyte combinations are known that are relatively stable against photo-oxidation: these combinations were optimized during years of research on dye-sensitized solar cells. In most Grätzel cells, ruthenium-based dyes are used in combination with an iodine/iodide redox couple (I_2/I^-), but unfortunately, this redox couple causes severe photo-corrosion of QDs[2]. In general, the photo-stability of QDs in the presence of an electrolyte redox couple is much less established, because the research on QD-sensitized solar cells started relatively recently[3] and investigated QD-electrolyte combinations are still sub-optimal. In the search for non-corrosive electrolytes, several alternatives for the iodine/iodide couple are being

explored including spiro-OMeTAD[3], a sulfide/polysulfide couple (S_2-/S_n^{2-})[2,4,5], and a cobalt based complex[6] $([Co(o\text{-phen})_3]^{2+/3+})$. Nonetheless, the effect of these various electrolytes on the QD stability is not yet well-established. Therefore, it is a logical choice to use dyes as light absorbers when studying the influence of the electrolyte on injection dynamics, since any perturbations of dynamical processes caused by photo-corrosion can be excluded. Here, we present a systematic study on the influence of the presence of an electrolyte on the dynamics of electron injection from two dye molecules, N3 and N719, into mesoporous oxide films.

7.2 Samples

Mesoporous TiO_2 and SnO_2 films were prepared by spreading out viscous dispersions of colloidal TiO_2 and SnO_2 particles on a microscope slide. For the TiO_2 film, an ethanol based paste containing 15 nm TiO_2 particles was purchased from Solaronix (T-LALT). A SnO_2 paste was obtained by dispersing SnO_2 powder (Aldrich, average particle size < 100 nm) in an ethanol solution containing NH_4OH (added to stabilize the colloidal suspension of SnO_2 particles). After deposition of the paste, the films were dried at 115°C for 30 minutes and subsequently annealed in air at 450°C for 2 hours. Two commonly used ruthenium-based dye molecules were used to sensitize the oxide. The chemical formula of these dyes, usually denoted as N3 and N719, is given in Fig. 7.1. In both dye molecules, the central ruthenium atom is coordinated by two bipyridine and two thiocyanide ligands. The carboxylate groups result in strong binding of the dye molecules to the oxide surface. The difference between the dyes is that all four carboxylate groups in N3 are protonated, whereas two of the four carboxylate groups in N719 are deprotonated and stabilized with a tetrabutylammonium (TBA) group.
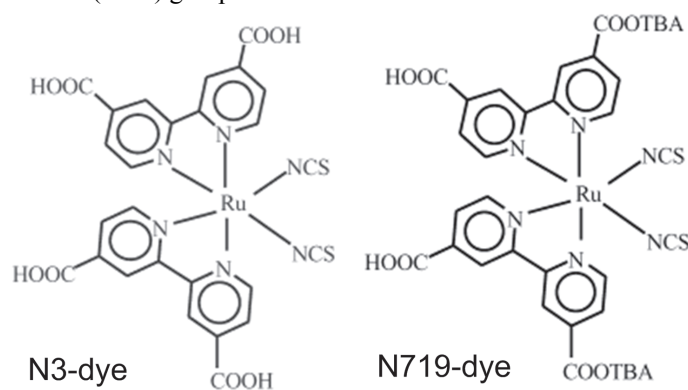

Figure 7.1 Molecular structures of the N3 and N719 dye.

Sensitization was achieved by immersing the oxide films (stored at 90°C to remove the hydroxyl groups terminating the oxide surface) in a 0.1 mM dye solution in anhydrous methanol for several hours. The absorption spectra of TiO_2 films sensitized with N3 and N719 are given in Fig. 7.2(a) and (b), respectively. Clearly, the absorption spectrum of the dye-sensitized films (solid lines) is similar to that of a dye solution in methanol (dashed lines). The broad absorption band at ~ 535 nm originates from a metal-to-ligand charge-transfer (MLCT) transition from a ruthenium d-orbital to the π*-orbital of the bipyridine ligands[7]. Exciting the dye with visible photons in the 400-650 nm range brings the molecule in its singlet (^{1}MLCT) state, after which it will relax to the triplet (^{3}MLCT) state with a characteristic singlet-to-triplet intersystem crossing time of < 100 fs[8,9]. This triplet state has been shown to be weakly luminescent with a ~nanosecond radiative lifetime[10]. The tail in the absorption spectrum at longer wavelength has been attributed to direct excitation of this luminescent state[10].
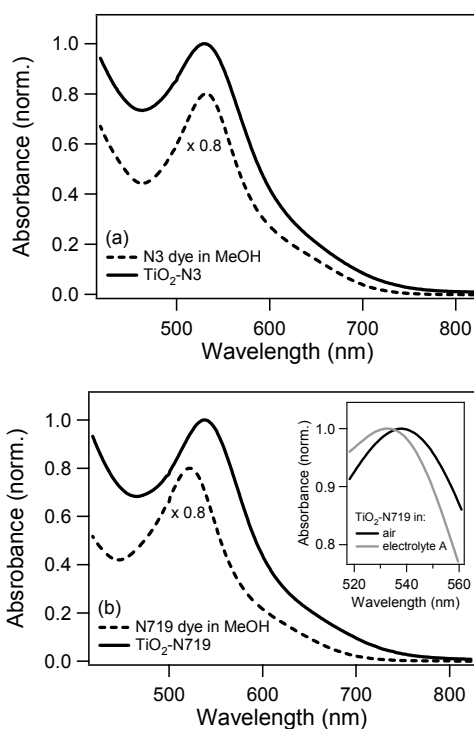

Figure 7.2 Absorption spectra for the N3 (a) and N719 (b) dye. The solid lines correspond to spectra for dye-sensitized TiO_2 films and the dashed lines are the spectra for the dyes dissolved in methanol. The inset in (b) shows that the absorption band at ~ 535 nm experiences a small blue-shift upon addition of electrolyte.

In this chapter, we use an I_2/I^- redox couple dissolved in acetonitrile as electrolyte, which is commonly used in Grätzel solar cells. It has been reported that additives like lithium ions and 4-*tert*-butyl pyridine (TBP) lead to an enhancement of the solar cell performance[11,12]. While the addition of lithium-salts leads to an increase of the short circuit current, the addition of TBP has been shown to result in larger open circuit voltages. To account for the effect of the various electrolyte components on injection dynamics, we investigated a number of electrolyte compositions, following Ref. 12:

- Electrolyte A: 0.6 M tetrabutylammonium iodide, 0.1 M lithium iodide, 0.5 M TBP, and 100 mM iodine dissolved in acetonitrile.
- Electrolyte B: similar as electrolyte A, but without the LiI.
- Electrolyte C: similar as electrolyte A, but without TBP

All chemicals were electrochemical or HPLC grade and were purchased from Fluka. To immerse the dye-sensitized film in the electrolyte, the microscope slide on which the oxide film was deposited was covered with a second microscope slide. Subsequently, the oxide matrix between the two microscope slides was interpenetrated with the electrolyte solution using capillary forces, resulting in a very thin electrolyte phase in the sample. This short path length was essential for the THz-TDS measurements, since THz light is strongly absorbed by polar solvents (like acetonitrile) that are commonly used for electrolyte solutions. We estimate that the thickness of the electrolyte phase amounted to ~ 10 μm, which was thin enough to have considerable transmission of THz light. After addition of electrolyte A, the absorption band of the dye sensitized film at 535 nm shifted slightly to shorter wavelengths, as can be seen in the inset of Fig. 7.2(b).

To demonstrate that dye-sensitized oxide films can be used to convert light into electrical current, we constructed a dye-sensitized solar cell with the same schematic layout as given in Fig. 6.1. Briefly, a TiO_2 film was deposited on conducting glass (indium-doped tin oxide, ITO) and sensitized with the N719 dye. The film was interpenetrated with electrolyte A and platinum was used as counter-electrode. Figure 7.3 shows the photocurrent action spectrum and the I-V characteristics for the fabricated dye-sensitized solar cell. Clearly, the spectral response from the photocurrent action spectrum closely matches the absorption spectrum in Fig. 7.2(b). The I-V characteristics of the solar cell are shown in Fig. 7.3(b) and indicate a short circuit current of 4.42 mA/cm^2, an open circuit voltage of 0.64 V, and a fill factor of 0.39.
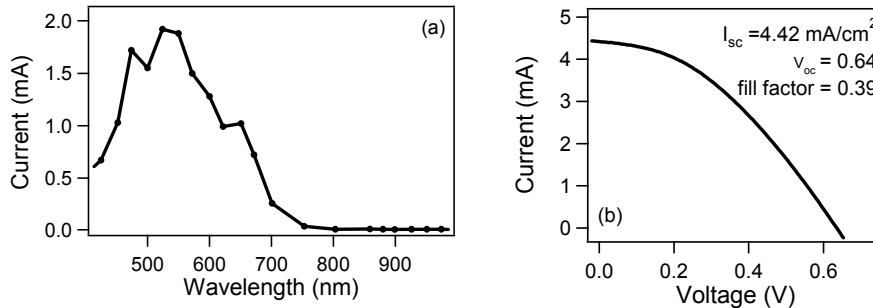
Figure 7.3 Photocurrent action spectrum (a) and I-V characteristics (b) of a N719-sensitized solar cell.

7.3 Why THz-TDS measurements?

The dynamics of electron injection from ruthenium-based dyes into mesoporous oxide materials has been studied with a number of experimental techniques. In all experiments the absorbed dyes were excited with visible (femto-second) pump pulses with wavelengths ranging from 400 – 630 nm. In Refs. 10 and 13 the injection of electrons from excited dyes into oxides was monitored by probing the emergence of the spectral signature of the cationic dye (concurrently produced with injection) at near-infrared frequencies. Alternatively, mid-infrared frequencies (~ 5 μm wavelength) were used to probe the transient population of injected electrons in the oxide films directly[8,14,15]. In all these transient absorption studies, the dye-sensitized oxide films were measured in inert solvents without the electrolyte components being present. Recently, TA measurements (near-infrared probe) in combination with time-resolved single photon counting measurements were performed on complete dye-sensitized solar cells including the electrolyte[12,16]. These measurements indicated that the timescale of electron injection is retarded with a factor of 20 resulting from the influence of the electrolyte on conduction band energetics of the oxide. In this chapter, we employ THz-TDS to study the effect of the electrolyte on electron injection dynamics. THz-TDS measurements have been performed previously[17-20] on dye-sensitized TiO$_2$ films, indicating sub-picosecond injection dynamics in inert solvents. Analogous to TA measurements with a mid-infrared probe[8,14,15], THz-TDS is a provides direct evidence of injected electrons, in contrast to TA measurements with a near-infrared probe or photon-counting experiments, in which injection timescales are inferred from transient signatures originating from the absorbed dye molecule[10,12,13,16]. The THz response to electrons in nanostructured oxide films has been discussed in section 2.4. In all THz measurements, we excited the sample with 590 nm light and recorded ΔE_{THz} (corresponding to the real conductivity) as a function of pump-probe delay.

7.4 Charge injection in dye-sensitized TiO$_2$

Photo-physical processes in (absorbed) ruthenium-based dye molecules have previously been intensely investigated[9,21,22]. An illustration of the different dynamic processes in a dye-sensitized oxide film after photo-excitation is given in Fig. 7.4. As a result of absorption of a visible photon by the dye, an electron is promoted from the ground state (D) to the singlet excited state (^{1}MLCT). The population of electrons in the ^{1}MLCT state can decay via injection into TiO$_2$ (characterized by τ_1). In parallel, the ^{1}MLCT state can undergo intersystem crossing to the excited manifold of the triplet ^{3}MLCT state, followed by intramolecular vibrational relaxation to the ^{3}MLCT ground state. (characterized by τ_2). Significant injection from the singlet state into TiO$_2$ will only occur when τ_1 is small compared to τ_2. In the situation where $\tau_1 > \tau_2$, the majority of the excited molecules in the ^{1}MLCT state will decay to the ^{3}MLCT state. From here, electrons can either be injected into TiO$_2$ or recombine to the ground state (characterized by τ_3 and τ_4, respectively). The injected electrons in TiO$_2$ will thermalize to the conduction band edge, from which they can recombine with the absorbed cationic dye molecule (D$^+$) or with the redox couple in the electrolyte (characterized by τ_5 and τ_6, respectively). The general theory to predict the rate of electron transfer between two chemical species was developed in the 1960's by Marcus[23], amongst others. As discussed in Ref. 14, this theory can be adapted to describe electron transfer between dyes and bulk semiconducting oxides. Three parameters that in principle determine the rate of electron injection are given below[14]:

Figure 7.4 Schematic diagram of the energy levels in a dye molecule with respect to the conduction band of the TiO$_2$ to which the dye is absorbed. All possible dynamic processes after photo-excitation of the dye are indicated by arrows (see explanation in text).

1. electronic coupling between the electron-donating orbital of the absorbed dye and the electron-accepting orbitals of the semiconductor
2. the Density of States (DOS) in the conduction band of the electron-accepting semiconductor
3. the free energy gain for injection, i.e. the potential energy difference between the dye excited state and the conduction band edge of the oxide
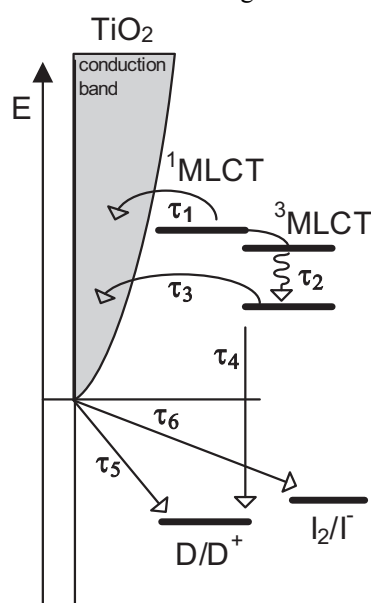
The dependence of the dye-semiconductor electron transfer rate on these parameters for the case of weak coupling (non-adiabatic limit) is given by the following expression[8,14]:

$$ K_{ET} = \frac{2\pi}{h} \int_{-\infty}^{\infty} dE \rho(E) |H(E)|^2 \frac{1}{\sqrt{4\pi\lambda k_b T}} \exp\left[-\frac{(\lambda + \Delta G_0 - E)^2}{4\lambda k_b T} \right] \qquad (7.1) $$

In equation 7.1, ΔG_0 is the energy difference between the conduction band edge and the redox potential of the dye excited state, $\rho(E)$ is the density of semiconductor states at energy E from the conduction band edge, $H(E)$ is the average electronic coupling between excited dye state and the different states in the semiconductor at energy E, and λ is the reorganization energy. Equation 7.1 clearly illustrates that the injection rate increases for higher density of acceptor states, stronger electronic coupling, and a larger free energy gain ΔG_0. Indeed, experimental reports show that injection from the dye singlet state into TiO_2 is faster than injection from the dye triplet state[8,12-14]: this observation has been be explained by the larger density of accepting states at the (higher) energy of the ^{1}MLCT state[8]. The effect of electronic coupling has been investigated by introducing a varying number of CH_2 units between the carboxylate linking group and the electron-donating bipyridine ligand. For increasing distance between the electron-donating ligand and the electron-accepting TiO_2 (less electronic coupling), the rate of electron injection has been demonstrated to slow down considerably[14]. Finally, the expected influence of ΔG_0 on injection dynamics was confirmed by a systematic study of a series of dyes with different excited state potentials (but comparable electronic coupling properties)[14].

It must be noted, however, that it is difficult to predict which of the three parameters in equation 7.1 is the rate-determining factor for electron injection from dyes into oxides. Recently, it has been argued that the DOS effect dominates over the effect of electronic coupling[15]. This was concluded by comparing the timescale of electron injection from Rhodamine with injection from the N3-dye. Despite large structural and electronic differences between Rhodamine and N3 (hence different electronic coupling), both dyes exhibited a similar semiconductor dependence, suggesting that DOS effects dominate[15]. As will be shown in section 7.5, a comparison between electron injection in N3-TiO_2 and N3-SnO_2 indicates that DOS arguments are also more important than the magnitude of ΔG_0.

Figure 7.5 shows the THz modulation for TiO_2 films sensitized with N719- and N3-dye that were immersed in acetonitrile. The THz signal represents the population of injected electrons in TiO_2. The data in Fig. 7.5 was obtained after exciting the films with 2 $\mu J/mm^2$ 590 nm pulses. We verified that the shape of the THz signal remained the same for lower excitation fluences. Also, we checked that the high excitation fluence did not cause any photo-corrosion, by verifying that the amplitude and the shape of the THz signal remained the same during ~one hour of data acquisition. When the sensitized films were measured in

121

air, however, the amplitude of the THz signal strongly decreased as a function of data acquisition time. This observed photo-degradation has been explained previously by oxygen induced desulfurization of the thiocyanide (SCN) ligands[10].
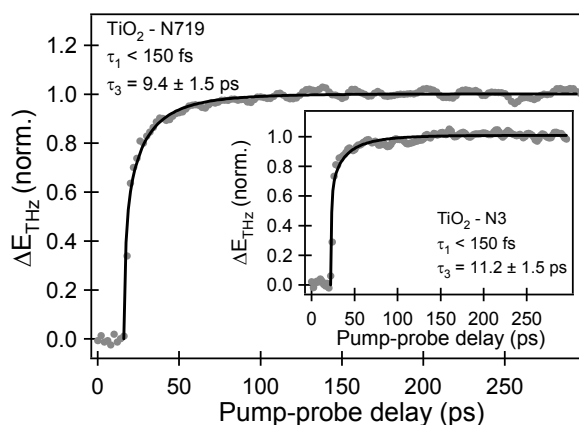

Figure 7.5 THz modulation for nanostructured TiO$_2$ films sensitized with N719 and N3 (inset), following excitation with 590 nm pulses. The data can be described with biphasic injection kinetics (solid lines), as explained in the text.

Clearly, the data in Fig. 7.5 exhibits a fast rise of the THz signal, followed by an ingrowth of the signal at longer timescale. This 'biphasic' injection kinetics is typical for TiO$_2$ sensitized with ruthenium-based dyes[8,10,12-14,20]. The fast component has been attributed to injection from the ^{1}MLCT state (characterized by τ_1 in Fig. 7.4), and the slower component was assigned to injection from the ^{3}MLCT state (characterized by τ_3)[8]. Injection from the high-energy singlet state is only possible if it occurs on faster or equally fast timescales as intersystem crossing from the singlet to the triplet state (characterized by τ_2 in Fig. 7.4). In literature, ultrafast injection from the singlet state in N3-TiO$_2$ was indeed reported with a time constant of $\sim$ 25 - 50 fs[24], while intersystem crossing from the singlet to the triplet state was found to occur within 30 or 75 fs (for TiO$_2$-N3 in air and ethanol, respectively)[9]. The fast injection from the singlet state in Ru-TiO$_2$ systems can be explained by the very high electron effective mass in TiO$_2$ ($\sim$ 10·m$_e$)[25], resulting in an extraordinary high DOS in the TiO$_2$ conduction band. Additionally, the conduction band of TiO$_2$ is formed from empty 3d orbitals of Ti^{4+} ions, having π symmetry[14]. Since the electron-donating orbital of the dye is the π* orbital of the bipyridine ligand, there is strong overlap between the donating and accepting orbitals, resulting in strong electronic coupling. The amplitude of the fast component in the biphasic injection is determined by the ratio of τ_1 and τ_2. The data in Fig. 7.5 is fit with the following equation[8]:

$$N_e = A(1 - \exp(-t/\tau_1)) + B(1 - \exp(-t/\tau_3)^{\alpha}) \qquad (7.2)$$

In this equation, N_e corresponds to the population of injected electrons, A and B are the amplitudes of injection from the singlet and triplet state, respectively, and α is the so-called stretch parameter. The use of the latter parameter is required since injection from the triplet state is not mono-exponential because of local inhomogeneities in the sensitized film (leading to local shifts of the conduction band edge, electronic coupling, etc.). The multi-exponential nature of the slow injection component is usually described by a stretched exponential, characterized by the stretch parameter α[8,13,16]. For $\alpha = 1$, the stretched exponential is equal to a mono-exponential ingrowth. Fitting the data in Fig. 7.5 with equation 7.2 yields values for τ_3 of 11.2 ± 1.5 ps for TiO$_2$-N3 and 9.4 ± 1.5 ps for TiO$_2$-N719. For both samples, the value of α was fixed to 0.7: this value resulted in much better fits than for using $\alpha = 1$. An upper limit for the time constant τ_1 of 150 fs was obtained for both samples, which was determined by the instrument response function of the THz-TDS setup. Next we measured the transient THz modulation for dye-sensitized TiO$_2$ films immersed in electrolyte solution with three different compositions (specified in section 7.2). For both N3- and N719 sensitized films, the observed trends are similar, as can be seen in Fig. 7.6.
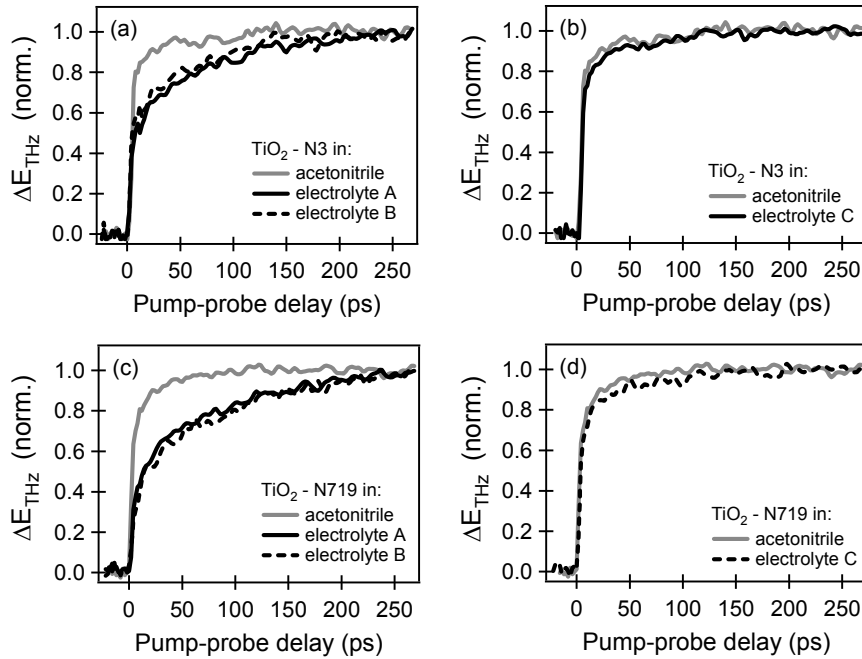

Figure 7.6 Transient THz modulation for TiO$_2$-N3 (a + b) and TiO$_2$-N719 (c + d) in different electrolytes. The composition of electrolytes A, B, and C is given in section 7.2.

When the films were immersed in electrolyte A (both Li^+ ions and TBP added) or in electrolyte B (only TBP added), the fast component of the biphasic kinetics in Fig. 7.5 is reduced markedly. However, when immersing the samples in electrolyte C (only Li^+ ions added), the injection dynamics were comparable to the dynamics observed for films immersed in (inert) acetonitrile. In the presence of electrolyte A, the value of τ_3 (obtained from fitting the data in Fig. 7.6) was found to be 50 ± 10 ps for TiO_2-N3 and 60 ± 10 ps for TiO_2-N719 for $\alpha = 0.7$. Since the injection was not completed at $\tau = 300$ ps, the error in the extracted time constants was larger than in Fig 7.5, but the data in Fig. 7.6 suggest clearly that the injection dynamics are strongly retarded in the presence of electrolyte A and B, compared to immersion in acetonitrile or electrolyte C where the majority of electrons is injected within ~ tens of picoseconds. The results in Fig. 7.6 are consistent with previous reports on the effect of electrolyte composition on injection dynamics[12,16]. In these reports, exactly the same electrolyte compositions were used, but electron dynamics were monitored by time-resolved single photon counting. In this technique, the emission from excited dye molecules absorbed to TiO_2 (injection possible) or ZrO_2 (control sample, injection energetically not allowed) is monitored for different electrolyte compositions. Since emission from the dyes is quenched when electron injection occurs, the amplitude and the dynamics of the emission from the TiO_2-dye sample (relative to the control sample) give information about the efficiency of electron injection and the corresponding dynamics. The trends observed in the time-resolved single photon counting experiments[12,16] are fully consistent with the THz-TDS measurements presented in Fig. 7.6. The authors in Refs. 12 and 16 have argued that the slower injection dynamics can be explained by the influence of the electrolyte additives (i.e. TBP and Li^+ ions) on the energetics of the TiO_2 conduction band. Briefly, spectro-electrochemical studies have indicated that the presence of TBP in the electrolyte leads to shifts of the TiO_2 conduction band to higher energies[11]. Similar studies have revealed that addition of Li^+ ions has the opposite effect: for increasing Li^+ concentration, the conduction band of TiO_2 shifts to lower energies. These shifts in the position of the conduction band cause variations in the density of TiO_2 acceptor states relative to the singlet and triplet dye excited state, as is visualized in Fig. 7.7. For the Li^+ and TBP concentrations used in this study, the induced shift of the conduction band can be as high as 300 meV[11,12], resulting in a 20-fold decrease or increase of the number of accepting TiO_2 states[12]. Hence, the addition of Li^+ (electrolyte C) facilitates fast electron injection, which is also corroborated by the presence of a fast injection component in Fig. 7.6(b) and (d). The fact that there is still a dispersive slow injection component in the presence of electrolyte C can be attributed to local variations of the Li^+ concentration in the homogeneous film[12,16]. Addition of TBP to the electrolyte strongly retards the injection dynamics, even in the case where Li^+ ions are present (electrolyte B). This observation can be explained by the higher concentration of TBP (0.5 M) than that of Li^+ (0.1 M).
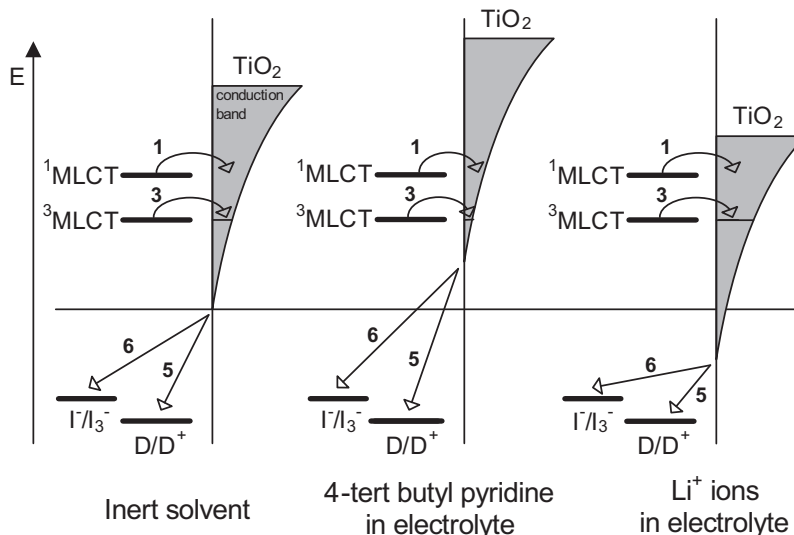
Figure 7.7 Schematic representation of shifts of the TiO_2 conduction band edge induced by addition of Li^+ ions or TBP. Clearly, these shifts lead to variation in the DOS of the TiO_2 at the position of the dye excited states (^1MLCT and ^3MLCT), hereby influencing injection dynamics.

In Fig 7.6(a) and 7.6(c), it can be seen that the fast injection component decreases in the presence of electrolyte A and B. This observation can also be explained by the reduction of the density of accepting states at the position of the ^1MLCT level, slowing down ultrafast injection from dye molecules in the ^1MLCT state. Hence, intersystem-crossing from the ^1MLCT to the ^3MLCT state (characterized by τ_2 in Fig. 7.4) is likely to become the dominating decay pathway for excited dye molecules in the singlet state, as was also argued in Ref. 16. Future studies should reveal that the fast injection component completely disappears upon increasing the TBP concentration.

At first sight, one might be tempted to conclude that the device performance of a dye-sensitized solar cell is sub-optimal in case of slower electron injection. The argumentation in this reasoning is that charge separation should occur as fast as possible to reduce any losses from recombination of excited dyes to the ground state (characterized by τ_4 in Fig. 7.4). However, it is known that the addition of TBP to the electrolyte solution significantly benefits the solar cell operation by increasing the V_{oc}, in spite of slower injection dynamics reported here and in Refs 12 and 16. This contradiction can be explained by the concept of 'kinetic redundancy'[12,16]: when the TiO_2 conduction band edge is shifted downwards, electron injection will occur on ultrafast (< 100 fs) time scale. However, for efficient charge separation, electron injection on a sub-picosecond time scale is not required, since the lifetime of excited dye is on the order of ~ 50 ns[12], indicating that the system is 'kinetically redundant'. The disadvantage of positioning the TiO_2 conduction band edge at lower energy

values is that the conduction band edge moves towards the Fermi level, as a result of which the occupancy of trapped states and conduction states increases[11]. This is important since recombination of electrons in TiO_2 with the cationic dye or the redox couple (characterized by τ_5 and τ_6 in Fig. 7.4, respectively) has been shown to depend strongly on the occupancy of trap and conduction states[11]. Hence ultrafast (< 100 fs) electron injection from dyes into TiO_2 is accompanied by increased recombination and does not automatically lead to higher solar cell efficiency. Addition of TBP, on the other hand, increases the time scale of electron injection from < 100 fs to ~ 100 ps, but this is still fast enough to extract the majority of the electrons from the excited dyes. Since the conduction band has shifted to higher energies (~ hundreds of meV, depending on the TBP concentration), hence moving away from the Fermi level, the time scale of recombination of electrons in the TiO_2 is reduced by orders of magnitude[11]. The above discussion illustrates that ultrafast electron injection is not a prerequisite for optimal solar cell efficiency, but that an optimal efficiency is obtained by achieving a balance between efficient charge separation and suppression of recombination of injected electrons: for optimal solar cell efficiency, 'kinetic redundancy' needs to be avoided.

7.5 Charge injection in dye-sensitized SnO_2

To further investigate the effect of the parameters determining electron transfer rates (density of accepting states in the oxide, electronic coupling, and the magnitude of ΔG_0), we studied electron injection dynamics in N3-sensitized SnO_2 films. Fig. 7.8 shows a comparison of the THz modulation for N3-sensitized SnO_2 and TiO_2 films. Although the energy of the SnO_2 conducting band edge is roughly 0.5 eV lower than the TiO_2 conduction band edge[26], electron injection into SnO_2 is slower compared to injection into TiO_2. This observation can be explained by the considerably lower electron effective mass in SnO_2 (~ $0.28 \cdot m_e$)[27], leading to a much lower DOS in the SnO_2 conduction band[8,14,15]. Furthermore, the conduction band of SnO_2 is formed by empty 5s orbitals of the Sn^{4+} ions. As a result, the overlap between the electron-donating π^* orbitals of the bipyridine ligands and the electron-accepting orbitals in the SnO_2 conduction band is not optimal and electronic coupling is relatively weak[14]. Apparently, DOS and electronic coupling arguments have a more pronounced influence on injection kinetics than the potential difference between the excited state dye and the conduction band edge.
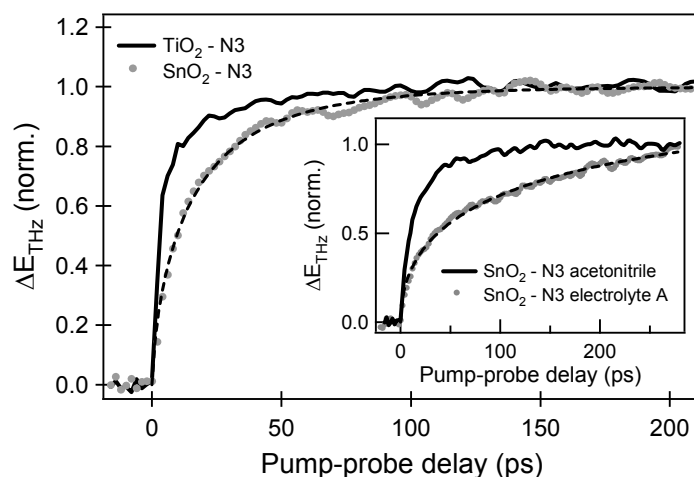
Figure 7.8 THz modulation for N3-sensitized SnO_2 (grey dots) and TiO_2 (black lines) following excitation with 590 nm pulses. In contrast with injection into TiO_2, electron injection into SnO_2 is not bi-phasic and can be fit with a stretched exponential ingrowth. The dynamics of the THz data are attributed to injection from the ^{3}MLCT state, as explained in the text. The inset shows a comparison of injection dynamics into SnO_2 in acetonitrile and electrolyte A.

The data in Fig. 7.8 can be fit with a single stretched exponential ingrowth ($N_e = B(1 - \exp(-t/\tau_3)^\alpha)$, fits represented by dashed black line in Fig. 7.8). This indicates that the kinetics of electron injection into SnO_2 is not bi-phasic, in contrast to injection in the Ru-TiO_2 system. The fit yields a time constant associated with electron injection of $\sim 16 \pm 1$ ps for $\alpha = 0.7$. We attribute this kinetics to injection from the ^{3}MLCT state, since the time constant is in good agreement with injection from the triplet state in the Ru-TiO_2 system. The absence of biphasic injection kinetics in the Ru-SnO_2 system indicates that injection from the ^{1}MLCT state is no longer fast enough to compete with relaxation to the ^{3}MLCT state ($\tau_1 \gg \tau_2$).

The inset of Fig. 7.8 shows a comparison of injection dynamics of the N3-sensitized SnO_2 immersed in acetonitrile (black solid line) and electrolyte A (grey dots). Clearly, electron injection in the presence of electrolyte A is slowed down significantly. Analogous to the Ru-TiO_2 system immersed in electrolyte A, this retardation of electron injection is likely caused by a positive shift of the SnO_2 conduction band edge, leading to reduced DOS of electron-accepting energy levels in SnO_2. The data in the inset of Fig. 7.8 is fit with the stretched exponential function yielding a time constant of electron injection of $\sim 160 \pm 20$ ps. The data in Fig. 7.8 indicates that the presence of electrolyte A reduces the rate of electron injection with at least one order of magnitude, which is in agreement with Ref. 12.

The similar trend for Ru-TiO$_2$ and Ru-SnO$_2$ when immersing the films in electrolyte indicates that the main effect of the electrolyte (shifting of the oxide conduction band edge, leading to changes of the DOS in the oxide at the position of the ^{1}MLCT and ^{3}MLCT states) can likely be generalized to other dye-oxide systems.

7.6 Discussion

In the previous sections, some essential parameters in charge transfer processes at the dye-semiconductor interface were discussed including electronic coupling between donating and accepting orbitals, density of accepting states, and the gain in free energy. These parameters are strongly influenced by several material characteristics such as the effective mass of the electron-accepting oxide (defining the density of states), the energies of the oxide conduction band edge and the excited states of the dye, and the dielectric constant of the solvent, amongst others. In many studies on dye-sensitized oxides, it has been suggested that density of states characteristics are dominating the rate of electron transfer, and electronic coupling to a lesser extent[12,14-16]. It is conceivable that similar arguments are important in charge transfer processes at QD-oxide interfaces. Presumably, electronic coupling at the QD-oxide interface is weaker than the coupling at the dye-oxide interface: in the excited dye, the electron is localized on the bipyridine ligand which is in intimate contact with the oxide via a carboxylate group, whereas the molecules used to link QDs to oxides typically span longer distances. The effect of the density of accepting states on injection dynamics from QDs has not been systematically addressed in literature. In one study, the injection dynamics were monitored for different QD sizes and faster injection was observed for smaller QDs[28]. This observation was explained by the larger value of $\varDelta G_0$ for smaller QDs (higher energy of 1S$_e$ level compared to the conduction band edge), but it is conceivable that higher density of accepting states at the energy of the 1S$_e$ level in small QDs also plays a role. This latter explanation is consistent with Fig. 7.8, where faster injection was observed in the TiO$_2$-N3 system than in SnO$_2$-N3, in spite of the higher value of $\varDelta G_0$ for SnO$_2$-N3, but in agreement with the higher density of states in TiO$_2$.

The observed changes of injection dynamics in dye-sensitized films in the presence of an electrolyte are also to be expected in a QD-sensitized system. There is no reason why additives like TBP or Li$^+$ would not lead to shift of the conduction band edge of QD-sensitized oxides. Of course, an optimal electrolyte composition has to be determined for QD-sensitized solar cells, hence it is currently not clear what the effect of the optimized electrolyte on injection dynamics from QDs will be. A possible retardation of injection dynamics in a QD-sensitized cell is not always detrimental for the overall cell efficiency. Slow injection dynamics will only reduce light-to-current conversion efficiencies if the

timescale of injection approaches the radiative lifetime of excitons in QDs. In future research, a systematic investigation of the parameters affecting electron injection in QD-sensitized oxides should be performed, as well as a correlation between injection dynamics, electrolyte composition, and device performance.

7.7 Conclusions

We have studied the dynamics of electron injection from ruthenium-based dyes into mesoporous oxide films. In an inert environment (air or acetonitrile), electron injection in dye-TiO_2 was found to occur with 'biphasic kinetics', in which the fast injection component (< 150 fs) corresponds to injection from the excited dye singlet state and the slow injection component (~ 10 ps) corresponds to injection from the excited triplet state of the dye. Electron injection into SnO_2 films is likely occurring from the triplet state only: although the energy difference between the dye excited state and the SnO_2 conduction band edge is larger than for dye-TiO_2, the density of accepting states is much lower in SnO_2, as a result of which injection from the singlet state is no longer fast enough to compete with intersystem crossing from the singlet to the triplet state.

For both the dye-TiO_2 and the dye-SnO_2 system, electron injection was significantly retarded when adding electrolyte solutions with compositions that have been reported to optimize solar cell efficiency[12]. By varying the electrolyte composition, we found that especially the addition of TBP (4-*tert*-butyl pyridine) causes slower injection. The explanation for this observation is that the addition of TBP shifts the oxide conduction band to higher energies, as a result of which the density of states at the energy position of the excited dye states decreases, leading to slower injection dynamics. Slower electron injection is not automatically detrimental for solar cell efficiency, since injection on ultrafast (< 100 fs) is 'kinetically redundant'[12] and is inherently associated with larger recombination of electrons in TiO_2 with the cationic dye or the redox couple. Positioning the conduction band at higher energies leads to slower electron injection (but still fast enough to extract the majority of photo-generated carriers), but significantly reduces recombination of electrons in TiO_2. It is conceivable that parameters like the density of states in the conduction band of the electron-accepting oxide and the composition of the electrolyte are also crucial in the design of efficient QD-sensitized solar cells.

References

(1)   O'Regan, B.; Gratzel, M. *Nature* **1991**, *353*, 737-740.
(2)   Tachibana, Y.; Akiyama, H. Y.; Ohtsuka, Y.; Torimoto, T.; Kuwabata, S. *Chem. Lett.* **2007**, *36*, 88-89.
(3)   Plass, R.; Pelet, S.; Krueger, J.; Grätzel, M.; Bach, U. *J. Phys.Chem.B* **2002**, *106*, 7578-7580.
(4)   Robel, I.; Subramanian, V.; Kuno, M.; Kamat, P. V. *J. Am. Chem. Soc.* **2006**, *128*, 2385-2393.
(5)   Bang, J. H.; Kamat, P. V. *ACS Nano* **2009**, *3*, 1467-1476.
(6)   Lee, H. J.; Chen, P.; Moon, S.-J.; Sauvage, F. d. r.; Sivula, K.; Bessho, T.; Gamelin, D. R.; Comte, P.; Zakeeruddin, S. M.; Seok, S. I.; Grätzel, M.; Nazeeruddin, M. K. *Langmuir* **2009**, *25*, 7602-7608.
(7)   Nazeeruddin, M. K.; Humphry-Baker, R.; Liska, P.; Gratzel, M. *J. Phys.Chem. B* **2003**, *107*, 8981-8987.
(8)   Asbury, J. B.; Anderson, N. A.; Hao, E.; Ai, X.; Lian, T. *J. Phys.Chem. B* **2003**, *107*, 7376-7386.
(9)   Benko, G.; Kallioinen, J.; Korppi-Tommola, J. E. I.; Yartsev, A. P.; Sundstrom, V. *J. Am. Chem. Soc.* **2001**, *124*, 489-493.
(10)   Tachibana, Y.; Moser, J. E.; Grätzel, M.; Klug, D. R.; Durrant, J. R. *J. Phys.Chem.* **1996**, *100*, 20056-20062.
(11)   Haque, S. A.; Tachibana, Y.; Willis, R. L.; Moser, J. E.; Gratzel, M.; Klug, D. R.; Durrant, J. R. *J. Phys.Chem. B* **1999**, *104*, 538-547.
(12)   Haque, S. A.; Palomares, E.; Cho, B. M.; Green, A. N. M.; Hirata, N.; Klug, D. R.; Durrant, J. R. *J. Am. Chem. Soc.* **2005**, *127*, 3456-3462.
(13)   Tachibana, Y.; Nazeeruddin, M. K.; Grätzel, M.; Klug, D. R.; Durrant, J. R. *Chemical Physics* **2002**, *285*, 127-132.
(14)   Asbury, J. B.; Hao, E.; Wang, Y.; Ghosh, H. N.; Lian, T. *J. Phys.Chem.B* **2001**, *105*, 4545-4557.
(15)   Huang, J.; Stockwell, D.; Boulesbaa, A.; Guo, J.; Lian, T. *J. Phys.Chem.C* **2008**, *112*, 5203-5212.
(16)   Koops, S. E.; O'Regan, B. C.; Barnes, P. R. F.; Durrant, J. R. *J. Am. Chem. Soc.* **2009**, *131*, 4808-4818.
(17)   Turner, G. M.; Beard, M. C.; Schmuttenmaer, C. A. *J. Phys.Chem. B* **2002**, *106*, 11716
(18)   Abuabara, S. G.; Cady, C. W.; Baxter, J. B.; Schmuttenmaer, C. A.; Crabtree, R. H.; Brudvig, G. W.; Batista, V. S. *J. Phys.Chem. C* **2007**, *111*, 11982-11990.
(19)   McNamara, W. R.; Snoeberger, R. C.; Li, G.; Schleicher, J. M.; Cady, C. W.; Poyatos, M.; Schmuttenmaer, C. A.; Crabtree, R. H.; Brudvig, G. W.; Batista, V. S. *J. Am. Chem. Soc.* **2008**, *130*, 14329-14338.
(20)   Tiwana, P.; Parkinson, P.; Johnston, M. B.; Snaith, H. J.; Herz, L. M. *J. Phys. Chem. C* **2009**, *114*, 1365-1371.
(21)   Damrauer, N. H.; Cerullo, G.; Yeh, A.; Boussie, T. R.; Shank, C. V.; McCusker, J. K. *Science* **1997**, *275*, 54-57.
(22)   Yeh, A. T.; Shank, C. V.; McCusker, J. K. *Science* **2000**, *289*, 935-938.
(23)   Marcus, R. A. *J. Chem. Phys.* **1965**, *43*, 679-701.
(24)   Hannappel, T.; Burfeindt, B.; Storck, W.; Willig, F. *J. Phys.Chem. B* **1997**, *101*, 6799-6802.
(25)   Enright, B.; Fitzmaurice, D. *J. Phys.Chem.* **1996**, *100*, 1027-1035.
(26)   Gratzel, M. *Nature* **2001**, *414*, 338-344.
(27)   Button, K. J.; Fonstad, C. G.; Dreybrodt, W. *Phys. Rev. B* **1971**, *4*, 4539.
(28)   Robel, I.; Kuno, M.; Kamat, P. V. *J. Am. Chem. Soc.* **2007**, *129*, 4136-4137.

Chapter 8: Conclusions

The goal of the research presented in this thesis was to evaluate the potential of QDs as light-absorbing materials in future solar cells. In chapter 1, two principles underlying the potentially more efficient light-to-energy conversion in QDs were discussed. These principles are briefly summarized below, together with a practical approach for a QD-based solar cell configuration.

1. 'Hot carrier' QD solar cell[1]: a configuration to utilize the energy of visible photons more effectively, by extracting carriers from 'hot' energy levels in QDs before intraband relaxation can take place. The utilization of hot carriers in solar cells is advantageous because it results in higher photo-voltages. Hot energy levels in QDs can be populated by direct absorption of high-energy photons, or by a combination of inter-band (near IR – visible) and intra-band (IR) transitions. In the 'hot' solar cell configuration, it is crucial that the hot electron is extracted sufficiently fast to prevent relaxation of hot carriers to cold energy levels.

2. QD solar cell based on Carrier Multiplication (CM): CM is an alternative approach to utilize the energy of visible photons more effectively. In the CM process, the excess energy of visible photons is used to excite additional electrons over the energy gap. In bulk materials, this process is relatively inefficient since hot carriers relax faster via thermalization than via CM[2], but it was predicted that CM would be more efficient in QDs because of reduced thermalization rates and increased Coulombic interaction between carriers[1,3]. The occurrence of efficient CM leads to multiple electron-hole pairs per absorbed photon, resulting in higher photo-currents for a given solar flux. To evaluate the potential of QD solar cells based on CM, it is essential to determine the mechanism of CM in QDs and the efficiency of the process.

3. QD-sensitized 'Grätzel' cell: after photo-excitation of QDs, carriers are confined in the small QD volume. In an operating solar cell, carriers need to be extracted from the QDs to generate photo-currents towards external contacts. Charge extraction can be achieved by chemical linking of QDs to a mesoporous oxide film[4,5]. In this configuration, electrons are injected from the QDs into the oxide film (serving as photo-anode) and holes can migrate to another external contact via an electrolyte that is interpenetrated in the mesoporous film. For efficient QD-sensitized solar cells, extraction of carriers needs to be faster than the lifetime of excitons in the QD.

From the above summary, it is clear that the dynamics of various carrier relaxation, recombination, and extraction processes are crucial factors that determine the light conversion efficiency in a QD-based solar cell. In this chapter, we will put our findings on carrier dynamics in nanostructured semiconductors in the context of other reports from literature and evaluate the potential of QDs as light absorbers in future solar cells, based on the current knowledge.

'Hot carrier' QD solar cell

Since slow intraband relaxation is crucial for the QD hot carrier concept, we examined in Chapter 3 the dynamics of intraband relaxation of electrons from the $1P_e \rightarrow 1S_e$ level in colloidal InAs. In spite of the predicted phonon-bottleneck[1], we observed that intraband relaxation was not slowed down significantly. We found that the phonon-bottleneck is circumvented by relaxation via an Auger mechanism, in which the excess energy of the $1P_e$ electron is transferred to a cold hole. This finding is consistent with previous reports on hot carrier relaxation in CdSe and InP QDs[6-9]. Suppressing this Auger relaxation pathway by trapping of the hole at the QD surface (resulting in reduced overlap between electron and hole wavefunctions) does not lead to a significant slowing of intraband relaxation, since hot electrons can relax by energy transfer to ligand vibrations[10]. Only recently[11], it has been demonstrated that intraband relaxation can be slowed down to the nanosecond time scale if all possible relaxation pathways are suppressed systematically. This result was achieved by separation of electron and hole wavefunctions in type II core-shell QDs, the use of special passivating molecules to which energy transfer was not possible, and by passivating the shell with another inorganic layer to reduce intraband relaxation via surface defects. In the core-shell QDs studied in Ref. 11, the electron was localized in the CdSe core, which was surrounded by 11 monolayers of shell material (corresponding to a shell thickness of ~ 3 nm). Although this demonstration of slow intraband relaxation of hot electrons is highly interesting from a fundamental scientific perspective, it is not obvious that the confined electrons in the core can be easily extracted, because of the high potential barrier imposed by the thick shell.

Summarizing, to achieve reduced intraband relaxation rates in QDs, 'normal' type I QDs (in which the electron and hole wavefunctions reside in the same volume) are not suitable since the phonon-bottleneck is bypassed by alternative relaxation mechanisms such as the Auger process. Separation of the electron and hole wavefunctions in a type II QD architecture is a promising approach, but only useful if both the electrons and the holes can be easily extracted, which is difficult in a core-shell geometry. Therefore, future research in QD hot solar cells should focus on the realization of new type II QD geometries, such as dumbbells, in which effective charge separation is combined with the possibility of charge extraction.

QD solar cell based on CM

In chapter 4, we have evaluated the efficiency of CM in InAs QDs. Although our initial measurements indicated the occurrence of efficient CM in InAs QDs, this result could not be reproduced under optimized experimental conditions. After having identified several experimental pitfalls that can lead to the overestimation of the CM factors in pump-probe experiments, we discarded our initial results of highly efficient CM, and concluded that CM does not occur with significant efficiency in InAs QDs.

The interest in CM in QDs was sparked by the publication of several reports claiming highly efficient CM in PbSe, InAs, and CdSe QDs[3,12-15]. From 2006 onwards, however, a number of reports[16-19] were published, in which low CM factors in QDs were reported. As a result, a strong controversy emerged, focusing on the question whether CM is enhanced in nanostructured materials (i.e. QDs) compared to bulk material. To answer this question, the reported CM factors for QDs had to be compared with reliable CM factors for bulk material. However, for the model materials in CM research, PbSe and PbS, no reliable data on the bulk CM factors was available. Therefore, we used THz-TDS (see Chapter 5) to quantify the number of photo-generated electron-hole pairs per absorbed photon (here defined as the CM factor) for these materials after excitation with wavelengths ranging from the ultraviolet to the infrared. Our results indicated that the CM factors were actually higher in bulk material than in the most recently reported QDs measurements (initial CM reports in QDs were not included in this comparison since these reported CM factors were probably overestimated, as indicated above). We could quantitatively account for the observed CM factors in both bulk and QDs by means of tight-binding calculations in which the relaxation of hot carriers was modeled as a competition between thermalization and impact ionization. From these calculations, it followed that the probability of impact ionization is lower in QDs compared to bulk because of the reduced density of final states in QDs owing to discretization of energy levels.

However, the CM factor in terms of number of electron-hole pairs per photon is not the sole parameter to assess the usefulness of CM in a QD solar cell, because of the larger energy gaps in QDs due to quantum confinement. As a result, the CM factor does not contain information about the fraction of the photon energy that is converted into excitons, and we therefore argued that the energy efficiency, i.e. the fraction of photon energy used to generate electron-hole pairs (defined as the ratio between the CM factor*E_g and the photon energy) is a more useful quantity. Our calculations reveal that, although the CM factors are lower in QDs than in bulk, the energy efficiency is higher in QDs. Despite this fact, we demonstrate in Chapter 5 that there is still little to no benefit of CM in QD solar cells, since the CM-related increase of the energy efficiency is only significant for excitation with ultraviolet light, which comprises a small fraction of the solar spectrum.

After having identified that the efficiency of CM in QDs is determined by the relative rates of hot carrier relaxation via thermalization and hot carrier relaxation via impact ionization, we can give directions for future research. It is unlikely that impact ionization can be made faster in QDs, since the rate of impact ionization is strongly determined by the density of *final* states, which is inherently lower in QDs compared to bulk. Hence, future research should focus on materials in which slower thermalization can be realized. In the context of CM in QDs, the realization of slow relaxation from the $1P_e \rightarrow 1S_e$ energy level (as demonstrated in Ref. 11) is not enough, since the energy associated with typical 1S-1P transitions is insufficient to excite additional electrons over the energy gap. To realize efficient CM at visible frequencies, (nano)materials should be synthesized in which slow thermalization of hot carriers at *large* excess energies ($> E_g$) is realized. This is very challenging.

Extraction of charges from photo-excited QDs:

To convert photo-generated excitons in QDs into an electrical current, electrons and holes need to be separated and directed towards different external contacts. In Chapter 6, we have investigated a possible 'charge extraction' configuration, in which QDs are chemically coupled to a mesoporous oxide film, facilitating electron injection from QDs into the oxide. This concept is analogous to the dye-sensitized 'Grätzel' cell, the only difference being that the dyes are replaced by QDs. Using a wide range of spectroscopic techniques (Transient Absorption, time-resolved luminescence, and THz-TDS) and device measurements, we have investigated injection of electrons from QDs into these oxide films. We did not observe electron injection in TiO_2 sensitized with PbSe QDs, which can be explained by an unfavorable energy alignment between the QD $1S_e$ level and the TiO_2 conduction band edge. In contrast, electron injection was observed in a PbSe-sensitized SnO_2 film, which can be explained by the lower energy of the SnO_2 conduction band edge. For both the SnO_2 and the TiO_2 sensitized films, TEM images indicated that QDs clusters were formed at the oxide surface. THz-TDS measurements indicated that, following photo-excitation of QD-sensitized films, mobile carriers were generated in these clusters that recombined within tens of picoseconds. Since the QD clusters act as recombination centers, their formation in QD solar cells should be avoided.

Another observation in Chapter 6 was that the interpretation of spectroscopic signals is sometimes challenging, since the QD-sensitized oxide films are by no means defect-free: for instance, quenching of the QD luminescence can readily be interpreted as electron injection but can also result from trapping at the QD-oxide interface or by energy transfer within QD clusters. Therefore, we argue in Chapter 6 that spectroscopic measurements should always be complemented with the measurement of macroscopic currents (e.g. measurement of I-V characteristics) to ensure that spectroscopic data is not falsely

interpreted as electron injection. In general, the understanding of electron extraction from QDs is rather limited at present. Much can be learned from the – analogous – research on electron injection from dyes into oxide films, since the parameters that influence injection kinetics are very similar for both systems. In future research, a systematic study is needed to asses the role of the density of accepting states in the oxide, electronic coupling between the QD and the oxide, and the energy alignment between QDs and the oxide in charge extraction dynamics. Also, suitable electrolytes should be developed for QD-sensitized solar cells, since the conventional electrolyte in dye-sensitized cells (based on an I^-/I_2 redox couple) causes photo-degradation of the QDs. In parallel, the effect of this new electrolyte (that is optimal for QD-sensitized solar cells) on electron injection dynamics needs to be investigated, since we have demonstrated in Chapter 7 that the electrolyte strongly affects the rate of electron injection in dye-sensitized solar cells.

Conclusion

In Chapter 1 of this thesis, QDs were pictured as promising building blocks for future solar cells, because of their special optical properties (high extinction coefficients, size-tunable energy gap) and because of their special carrier recombination and carrier relaxation characteristics. After four years of research, the promise of QDs for use in solar cells still holds, but several challenges associated with utilization of the special properties of QDs in photovoltaic applications have become apparent. It is more difficult than previously thought to slow down intraband relaxation of hot carriers in QDs and furthermore, the efficiency of Carrier Multiplication in QDs is not as high as previously reported. And although the optical properties of QDs may be excellent, the extraction of carriers from QDs towards external contacts is more complicated than in e.g. bulk silicon solar cells. Therefore, to fulfill the promise of QD solar cells remains a formidable challenge and considerably more research is needed to overcome the significant scientific and technological issues that currently prohibit the commercialization of QD solar cells.

References

(1) Nozik, A. J. *Physica E* **2002**, *14*, 115-120.
(2) Kolodinski, S.; Werner, J. H.; Wittchen, T.; Queisser, H. J. *Appl. Phys. Lett.* **1993**, *63*, 2405-2407.
(3) Schaller, R. D.; Klimov, V. I. *Phys. Rev. Lett.* **2004**, *92*.
(4) Robel, I.; Subramanian, V.; Kuno, M.; Kamat, P. V. *J. Am. Chem. Soc.* **2006**, *128*, 2385-2393.

(5)   HyoJoong, L.; Henry, C. L.; Soo-Jin, M.; Peter, C.; Seigo, I.; Saif, A. H.; Tomas, T.; Frank, N.; Thomas, G.; Shaik, M. Z.; Michael, G.; Md. Khaja, N. *Adv. Functional. Mater.* **2009**, *19*, 2735-2742.

(6)   Klimov, V. I.; McBranch, D. W. *Phys. Rev. Lett.* **1998**, *80*, 4028-4031.

(7)   Guyot-Sionnest, P.; Shim, M.; Matranga, C.; Hines, M. *Phys. Rev. B* **1999**, *60*, R2181-R2184.

(8)   Blackburn, J. L.; Ellingson, R. J.; Micic, O. I.; Nozik, A. J. *J. Phys. Chem. B* **2003**, *107*, 102-109.

(9)   Hendry, E.; Koeberg, M.; Wang, F.; Zhang, H.; Donega, C. d. M.; Vanmaekelbergh, D.; Bonn, M. *Phys. Rev. Lett.* **2006**, *96*, 057408-057404.

(10)   Guyot-Sionnest, P.; Wehrenberg, B.; Yu, D. *J. Chem. Phys.* **2005**, *123*.

(11)   Pandey, A.; Guyot-Sionnest, P. *Science* **2008**, *322*, 929-932.

(12)   Schaller, R. D.; Agranovich, V. M.; Klimov, V. I. *Nature Phys.* **2005**, *1*, 189-194.

(13)   Ellingson, R. J.; Beard, M. C.; Johnson, J. C.; Yu, P. R.; Micic, O. I.; Nozik, A. J.; Shabaev, A.; Efros, A. L. *Nano Lett.* **2005**, *5*, 865-871.

(14)   Schaller, R. D.; Sykora, M.; Pietryga, J. M.; Klimov, V. I. *Nano Lett.* **2006**, *6*, 424-429.

(15)   Schaller, R. D.; Pietryga, J. M.; Klimov, V. I. *Nano Lett.* **2007**, *7*, 3469-3476.

(16)   Nair, G.; Bawendi, M. G. *Phys. Rev. B* **2007**, *76*, 4.

(17)   Nair, G.; Geyer, S. M.; Chang, L.-Y.; Bawendi, M. G. *Phys. Rev. B* **2008**, *78*, 125325-125310.

(18)   Ben-Lulu, M.; Mocatta, D.; Bonn, M.; Banin, U.; Ruhman, S. *Nano Lett.* **2008**, *8*, 1207-1211.

(19)   Pijpers, J. J. H.; Hendry, E.; Milder, M. T. W.; Fanciulli, R.; Savolainen, J.; Herek, J. L.; Vanmaekelbergh, D.; Ruhman, S.; Mocatta, D.; Oron, D.; Aharoni, A.; Banin, U.; Bonn, M. *J. Phys. Chem. C* **2008**, *112*, 4783-4784.

Summary

The research presented in this thesis is aimed at evaluating the potential of nanostructured semiconductors (e.g. quantum dots) as light-absorbing materials in next generation solar cells. The search for novel light-absorbing materials that convert light more efficiently into electricity is motivated by the relatively low efficiency of conventional, single bandgap, solar cells. According to the theoretical Shockley-Queisser limit, no more than 30% of the energy of incident solar light can be converted into electrical energy by a silicon solar cell. This limited conversion efficiency is a result of two fundamental drawbacks of silicon solar cells: firstly, the infrared part of the solar spectrum is not absorbed by silicon, since the infrared photons do not have enough energy to excite electrons over the bandgap (1.1 eV for silicon, corresponding to a photon wavelength of $\lambda \sim 1100$ nm). Secondly, the absorption of photons with energy in excess of the bandgap results in generation of 'hot' electrons and holes. These 'hot charge carriers' relax to the band edges via sequential emission of phonons on ultrafast timescales. Via this so-called rapid 'thermalization' process, the excess energy of visible photons is converted into phonons (or heat).

Various strategies are being pursued to design solar cells that can overcome the Shockley-Queisser limit by harvesting the excess energy of visible photons. To prevent that the excess energy of visible light is lost as heat (via thermalization), control of the relaxation of hot carriers to the lowest excited state is required. QDs have been proposed as light absorbing materials for future solar cells because of potentially favorable relaxation characteristics of hot carriers. Two QD-based solar cell concepts are briefly discussed below:

- 'Hot carrier' QD solar cell: a configuration in which the excess energy of visible photons is utilized, by extracting carriers from 'hot' energy levels in QDs before intraband relaxation (thermalization) can take place. Thermalization via phonon emission was predicted to be slower in QDs due to the discrete nature of the energy levels: since the spacing between energy levels in QDs is much higher than typical phonon energies, thermalization can only occur via simultaneous emission of multiple phonons, which was thought to be a process with low probability (hence slow). The possibility of harvesting hot carriers in solar cells is advantageous because it results in higher photo-voltages. Hot energy levels in QDs can be populated by direct absorption of high-energy photons, or by a combination of inter-band (near IR – visible) and intra-band (IR) transitions.

- QD solar cell based on Carrier Multiplication (CM): CM is an alternative approach to utilize the energy of visible photons more effectively. In the CM process, the excess energy of visible photons is used to excite additional electrons over the energy gap. In

bulk materials, this process is relatively inefficient since hot carriers relax faster via thermalization than via CM, but it was predicted that CM would be more efficient in QDs because of reduced thermalization rates and increased Coulombic interaction between carriers. The occurrence of efficient CM leads to multiple electron-hole pairs per absorbed photon, resulting in higher photo-currents for a given solar flux.

From the above, it is clear that the dynamics of various carrier relaxation, recombination, and extraction processes are crucial factors that determine the light conversion efficiency in a QD-based solar cell. Throughout this thesis, we have employed various ultrafast spectroscopic techniques to gain insight in these dynamic processes. Especially, we used THz time-domain spectroscopy (THz-TDS) to monitor carrier dynamics in QDs and bulk semiconductors. In a typical THz experiment, the material under investigation is excited with a femtosecond (100 fs = 10^{-13} s) duration visible laser pulse. The transient behavior of the photo-generated carriers is probed with a second pulse of ~ picosecond (1 ps = 10^{-12} s) duration centered at THz frequencies (~ 0.2 – 2 THz). The oscillating electric field of the THz probe interacts strongly with charge carriers and the complex photoconductivity of a material can be extracted from the transmitted THz pulse. Changes in the amplitude of the transmitted THz transmission are related to *real* conductivity, associated with the absorption of THz light. The real conductivity gives information about the number and mobility of free carriers in semiconductors, since THz light is strongly absorbed by free carriers. In addition, the phase-shift of the transmitted THz pulse through a sample is related to the *imaginary* conductivity, which is related to the (photo-induced change in) refractive index of a material. The shape of the complex frequency dependent conductivity at THz frequencies gives information about the nature of carrier conductivity in a material. By recording the photoconductivity at various pump-probe delays, one can investigate various dynamic processes of carriers in quantum dots and bulk semiconductors. The most important results of these experiments are summarized below.

Since slow intraband relaxation is crucial for the QD hot carrier concept, we examined in Chapter 3 the dynamics of intraband relaxation of electrons from the $1P_e$ → $1S_e$ level in InAs QDs. However, we observed fast intraband (< 1 ps) relaxation dynamics that can be accounted for by an Auger mechanism, in which the excess energy of the $1P_e$ electron is transferred to a cold hole. This finding is consistent with previous reports on hot carrier relaxation in type I QDs (in which the electron and hole wavefunctions reside in the same volume) like CdSe and InP QDs. A prerequisite for slow intraband relaxation in QDs is that the Auger relaxation pathway is suppressed. This can be achieved by separating the electron and hole wavefunctions in a type II QD architecture, but this approach is useful only if both the electrons and the holes can be easily extracted, which is difficult in a core-shell

138

geometry. Therefore, future research in QD hot solar cells should focus on the realization of new type II QD geometries, such as dumbbells, in which effective charge separation is combined with the possibility of charge extraction.

In Chapter 4, we evaluated the CM factor (i.e. number of generated excitons per absorbed photon) in InAs QDs. Although initial measurements indicated the occurrence of efficient CM, this result could not be reproduced under optimized experimental conditions. After having identified several experimental pitfalls that can lead to the overestimation of the CM factors in pump-probe experiments, we discarded our initial results of highly efficient CM, and concluded that CM does not occur with significant efficiency in InAs QDs. The results in Chapter 4 are representative for the controversy in the CM community, where contradicting CM factors have been reported for various QD materials. The central question in this debate is whether CM is enhanced in nanostructured materials (i.e. QDs) compared to bulk material. To answer this question, the reported CM factors for QDs had to be compared with reliable CM factors for bulk material. However, for the model materials in CM research, PbSe and PbS, no reliable data on the bulk CM factors was available. Therefore, we used THz-TDS in Chapter 5 to quantify the CM factors for these materials after excitation with wavelengths ranging from the ultraviolet to the infrared. Our results indicated that the CM factors were actually higher in bulk material than in the majority of reported QDs measurements. We could quantitatively account for the observed CM factors in both bulk and QDs by means of tight-binding calculations in which the relaxation of hot carriers was modeled as a competition between thermalization and impact ionization. From these calculations, it follows that the probability of impact ionization is lower in QDs compared to bulk because of the reduced density of final states in QDs owing to discretization of energy levels. To assess the usefulness of CM in a QD solar cell, however, the value of the CM factor is not the most relevant parameter, because of the larger energy gaps in QDs due to quantum confinement. As a result, the CM factor does not contain information about the fraction of the photon energy that is converted into excitons, and therefore the energy efficiency, i.e. the fraction of photon energy used to generate electron-hole pairs (defined as the ratio between the CM factor*E_g and the photon energy) is a more useful quantity. Our calculations reveal that, although the CM factors are lower in QDs than in bulk, the energy efficiency is higher in QDs. Despite this fact, we demonstrate in Chapter 5 that there is still little to no benefit of CM in QD solar cells, since the CM-related increase of the energy efficiency is only significant for excitation with ultraviolet light, which comprises a small fraction of the solar spectrum. For future research on CM, the following considerations are important: it is unlikely that impact ionization can be made faster in QDs, since the rate of impact ionization is strongly determined by the density of *final* states, which is inherently lower in QDs compared to bulk. Hence, future research should focus on materials in which slower thermalization can be realized. In the context of CM in QDs, the

139

realization of slow relaxation from the $1P_e \rightarrow 1S_e$ energy level is not enough, since the energy associated with typical 1S-1P transitions is insufficient to excite additional electrons over the energy gap. To realize efficient CM at visible frequencies, (nano)materials should be synthesized in which slow thermalization of hot carriers at *large* excess energies ($> E_g$) is realized. This is very challenging.

To convert photo-generated excitons in QDs into an electrical current, electrons and holes need to be separated and directed towards different external contacts. In Chapter 6, we have investigated a possible 'charge extraction' configuration, in which QDs are chemically coupled to a mesoporous oxide film, facilitating electron injection from QDs into the oxide. This concept is analogous to the dye-sensitized 'Grätzel' cell, the only difference being that the dyes are replaced by QDs. Using a wide range of spectroscopic techniques (Transient Absorption, time-resolved luminescence, and THz-TDS) in conjunction with device measurements, we have investigated injection of electrons from QDs into these oxide films. We did not observe electron injection in TiO_2 sensitized with PbSe QDs, which can be explained by an unfavorable energy alignment between the QD $1S_e$ level and the TiO_2 conduction band edge. In contrast, electron injection was observed in a PbSe-sensitized SnO_2 film, which can be explained by the lower energy of the SnO_2 conduction band edge. For both the SnO_2 and the TiO_2 sensitized films, TEM images indicate that QDs clusters form at the oxide surface. THz-TDS measurements indicated that, following photo-excitation of QD-sensitized films, mobile carriers were generated in these clusters that recombined within tens of picoseconds. Since the QD clusters act as recombination centers, their formation in QD solar cells should be avoided. Another observation in Chapter 6 was that the interpretation of spectroscopic signals is sometimes challenging, since the QD-sensitized oxide films are by no means defect-free: for instance, quenching of the QD luminescence can readily be interpreted as electron injection but can also result from trapping at the QD-oxide interface or by energy transfer within QD clusters. To ensure that spectroscopic data is not wrongly interpreted as electron injection, spectroscopic measurements should always be complemented with the measurement of macroscopic currents (e.g. measurement of I-V characteristics). In general, the understanding of electron extraction from QDs is rather limited at present. Much can be learned from the – analogous – research on electron injection from dyes into oxide films, since the parameters that influence injection kinetics are very similar for both systems. In future research, a systematic study is needed to asses the effect of the density of accepting states in the oxide, electronic coupling between the QD and the oxide, and the energy alignment between QDs and the oxide on charge extraction dynamics. Also, suitable electrolytes should be developed for QD-sensitized solar cells, since the conventional electrolyte in dye-sensitized cells (based on an I^-/I_2 redox couple) causes photo-degradation of QDs. In parallel, the effect of this new electrolyte (that is optimal for QD-sensitized solar cells) on electron

injection dynamics needs to be investigated, since we have demonstrated in Chapter 7 that the electrolyte strongly affects the rate of electron injection in dye-sensitized solar cells.

Summarizing, QDs were pictured in Chapter 1 of this thesis as potentially promising building blocks for future solar cells, because of their special optical properties (high extinction coefficients, size-tunable energy gap) and because of their special carrier recombination and carrier relaxation characteristics. After four years of research, the promise of QDs for use in solar cells still holds, but several challenges associated with utilization of the special properties of QDs in photovoltaic applications have become apparent. It is more difficult than previously thought to slow down intraband relaxation of hot carriers in QDs and furthermore, the efficiency of Carrier Multiplication in QDs is not as high as previously reported. And although the optical properties of QDs may be excellent, the extraction of carriers from QDs towards external contacts is more complicated than in e.g. bulk silicon solar cells. Therefore, to fulfill the promise of QD solar cells remains a formidable challenge and considerably more research is needed to overcome the significant scientific and technological issues that currently prohibit the commercialization of QD solar cells.

Samenvatting

Het onderzoek in dit proefschrift had tot doel om het potentieel van nanogestructureerde halfgeleiders (zoals quantum dots) als licht-absorberende materialen voor toekomstige zonnecellen te evalueren. De motivatie voor de ontwikkeling van nieuwe zonnecel materialen wordt gegeven door het feit dat bestaande zonnecellen (die veelal op silicium gebaseerd zijn) slechts een beperkte efficiëntie hebben. De zogenaamde Shockley-Queisser limiet dicteert namelijk dat in een silicium zonnecel niet meer dan 30% van de energie van zonlicht kan worden omgezet in elektrische energie. Deze limiet aan de conversie efficiëntie wordt bepaald door twee fundamentele nadelen van silicium zonnecellen: ten eerste wordt het infrarode deel van het zonnespectrum niet geabsorbeerd door silicium, omdat infrarode fotonen niet genoeg energie hebben om een elektron over de bandgap te exciteren. Ten tweede leidt de absorptie van fotonen die meer energie dan de bandgap bezitten tot de generatie van zogenaamde 'hete' elektronen en gaten (ladingen met een overmaat aan energie). Deze hete ladingen relaxeren zeer snel naar de band minima via sequentiële emissie van fononen. Via dit zogenaamde 'thermalizatie' proces wordt de overmaat aan energie van zichtbare fotonen omgezet in fononen (warmte).

Verschillende strategieën worden gevolgd om zonnecellen te ontwerpen die de Shockley-Queisser limiet kunnen omzeilen door de overmaat aan energie van zichtbare fotonen om te zetten in elektrische energie. Om dit te bewerkstelligen is het noodzakelijk dat de relaxatie van hete ladingen onder controle wordt gebracht. Quantum Dots (QDs) worden vaak genoemd als mogelijke licht-absorberende materialen waarin de relaxatie van hete ladingen goed kan worden gecontroleerd. Twee zonnecel concepten die zijn gebaseerd op quantum dots worden hieronder kort besproken:

- 'Hete lading' zonnecel: in deze configuratie wordt de overmaat aan energie van zichtbare fotonen geëxtraheerd uit 'hete' QD energie niveaus voordat thermalizatie kan plaatsvinden. Uitgangspunt van dit concept is dat thermalizatie door middel van fonon emissie mogelijk langzamer verloopt in quantum dots vanwege de discrete aard van de energie niveaus: doordat de afstand tussen energie niveaus in quantum dots vele malen groter is dan typische fonon energieën zou thermalizatie alleen kunnen plaatsvinden door middel van gelijktijdige emissie van fononen, een proces met een lage waarschijnlijkheid (en dus relatief langzaam). De mogelijkheid om hete ladingen te extraheren is aantrekkelijk omdat dit gepaard gaat met hogere foto-voltages in zonnecellen. Hete energie niveaus in QDs kunnen worden gepopuleerd door directe absorptie van hoogenergetische fotonen, maar ook door een combinatie van inter-band (nabij-infrarood / zichtbaar) and intra-band (infrarood) overgangen.

- QD zonnecel gebaseerd op Carrier Multiplication (CM, ladingsvermenigvuldiging). CM is een alternatieve manier om de overmaat aan energie van hete ladingen efficiënter te gebruiken. In het CM proces wordt de overmaat aan energie aangewend om een extra elektron over de bandgap te exciteren. Dit proces is relatief inefficiënt in bulk halfgeleiders, omdat hete ladingen sneller relaxeren via sequentiële fonon emissie dan via CM. Het was echter voorspeld dat CM efficiënter zou kunnen optreden in QDs vanwege een gereduceerde snelheid van thermalizatie en een sterkere Coulomb interactie tussen ladingen. Efficiënte CM leidt tot de generatie van meerdere elektron-gat paren per geabsorbeerd foton, met hogere fotostromen tot gevolg.

Uit het bovenstaande blijkt dat de tijdsschaal van verschillende ladingsrelaxatie, recombinatie, en extractie processen een cruciale factor is die bepalend is voor de hoogte van de conversie efficiëntie in een QD-zonnecel. Deze dynamische processen zijn in het kader van dit proefschrift onderzocht met behulp van verschillende ultrasnelle spectroscopische technieken. In het bijzonder is tijdsopgeloste TeraHertz spectroscopie (THz-TDS) gebruikt om ladingsdynamica in QDs en bulk halfgeleiders te bestuderen. In een typisch THz experiment wordt een sample geëxciteerd met een femtoseconde (100 fs = 10^{-13} s) puls van zichtbaar licht. Het transiënte gedrag van de fotogegenereerde ladingsdragers wordt gedetecteerd met behulp van een tweede laser puls met een picoseconde (1 ps = 10^{-12} s) duur die bestaat uit THz frequenties ($\sim$ 0.2-2 THz). Het oscillerende elektrische veld van de THz puls interacteert sterk met ladingsdragers en uit de transmissie van de THz pulse door het geëxciteerde sample kan de complexe fotoconductiviteit van een materiaal worden bepaald. Veranderingen in de amplitude van de THz tranmissie zijn gerelateerd aan de *reële* conductiviteit, een grootheid die informatie bevat over het aantal en de mobiliteit van vrije ladingsdragers in halfgeleiders. Daarnaast is de fase-verschuiving van de THz puls een maat voor de *imaginaire* conductiviteit, die gerelateerd is aan de fotogeïnduceerde verandering van de refractieve index van een materiaal. De vorm van de complexe frequentie-afhankelijke conductiviteit geeft informatie over de aard van de conductiviteit van ladingen in een materiaal. Door de fotoconductiviteit te meten op verschillende momenten na absorptie van de excitatie puls, kunnen dynamische processen van ladingsdragers in halfgeleiders (zowel QDs als bulk) worden bestudeerd. De belangrijkste resultaten van deze experimenten worden hieronder besproken.

In hoofdstuk 3 is de snelheid van elektron relaxatie van het $1P_e$ naar het $1S_e$ niveau in InAs QDs bestudeerd, een proces waarvan de snelheid van belang is in het 'hete lading' zonnecel-concept. De geobserveerde tijdsschaal van intraband relaxatie was zeer snel (< 1 ps), wat kan worden verklaard door een Auger mechanisme waarin de overmaat aan energie van een $1P_e$ elektron wordt overgedragen aan een koud gat. Deze observatie is consistent met eerdere rapportages omtrent relaxatie van hete ladingen in type I QDs (waar de elektron

en gat golffuncties zijn gelokaliseerd in hetzelfde volume) zoals CdSe en InP QDs. Een voorwaarde voor de aanwezigheid van langzame intraband relaxatie is dat het Auger relaxatie kanaal wordt onderdrukt. Dit kan worden bewerkstelligd door de golffuncties van elektronen en gaten te scheiden in type II QDs, maar deze aanpak is alleen bruikbaar in een zonnecel wanneer zowel het elektron als het gat kan worden geëxtraheerd. Deze extractie is niet triviaal in een type II core-shell geometrie. Daarom zal toekomstig onderzoek op het gebied van hete lading zonnecellen zich moeten richten op de realisatie van nieuwe type II structuren, zoals bijvoorbeeld een halter geometrie ('dumbbell'), waarin effectieve ladingsscheiding kan worden gecombineerd met de mogelijkheid van ladingsextractie.

In hoofdstuk 4 is de CM factor (het aantal gegenereerde excitonen per geabsorbeerd foton) bepaald voor InAs QDs. Hoewel initiële experimenten leken te duiden op de aanwezigheid van efficiënte CM, was het niet mogelijk om deze resultaten te reproduceren onder geoptimaliseerde experimentele omstandigheden. Na meerdere experimentele valkuilen te hebben geïdentificeerd die kunnen leiden tot een overschatting van de CM factor in pomp-probe experimenten, hebben we onze aanvankelijke resultaten verworpen en geconcludeerd dat CM niet plaatsvindt met significante efficiëntie in InAs QDs. Het resultaat van hoofdstuk 4 is illustratief voor de controverse in het onderzoek naar CM in QDs, waar tegenstrijdige CM factors zijn gerapporteerd voor verschillende QD materialen. De centrale vraag in dit debat is of de CM factors hoger zijn is in nano-materialen (bijv. QDs) dan in bulk materialen. Voor het beantwoorden van deze vraag was het nodig om de CM factors voor QDs te vergelijken met betrouwbare waardes van CM factors voor bulk. Voor de meest bestudeerde materialen het CM-onderzoek, PbSe en PbS, waren er echter geen betrouwbare CM factors bekend. Daarom hebben we in hoofdstuk 5 THz-TDS gebruikt om de CM factors voor deze materialen te bepalen voor verschillende excitatie-golflengtes, variërend van het ultraviolet tot het infrarood. In tegenstelling tot de verwachting gaven onze resultaten aan dat de CM factors hoger waren voor bulk dan voor de meerderheid van de gerapporteerde QD-waarden. Het was mogelijk om de CM factors voor zowel QDs als bulk kwantitatief te beschrijven door middel van 'tight binding' berekeningen, waarin de relaxatie van hete ladingen is gemodelleerd als een competitie tussen thermalizatie en impact ionisatie. Deze berekeningen maakten duidelijk dat de waarschijnlijkheid van impact ionisatie lager is in QDs dan in bulk vanwege de gereduceerde Density of States (DOS, toestandsdichtheid) in QDs. Voor de evaluatie van het nut van CM voor QD-zonnecellen is de CM factor echter niet de relevante parameter omdat de energie 'gaps' in QDs groter zijn als gevolg van kwantum effecten. Het gevolg is dat de CM factor geen informatie bevat over de fractie van de foton energie die wordt omgezet in excitonen. Daarom is de energie efficiëntie (de fractie van de foton energie die gebruikt wordt om excitonen te genereren, gedefinieerd als de ratio tussen de CM factor*E_g en de foton energie) een meer bruikbare parameter. Onze berekeningen laten zien dat de

energie efficiëntie hoger is in QDs dan in bulk, ondanks de lagere waardes voor de CM factors. Desalniettemin wordt in hoofdstuk 5 aangetoond dat de winst door CM voor zonnecellen beperkt is, omdat de CM-gerelateerde toename van de energie efficiëntie alleen significant is voor excitatie met ultraviolette fotonen en dit licht maakt slecht een klein deel van het totale zonnespectrum uit. Voor toekomstig onderzoek naar CM in QDs zijn de volgende overwegingen van belang: het is onwaarschijnlijk dat impact ionisatie kan worden versneld in QDs, omdat de snelheid van impact ionisatie sterk afhangt van de Density of *final* States, die intrinsiek lager is in QDs in vergelijking met bulk. Daarom zal toekomstig onderzoek gericht moeten zijn op de ontwikkeling van materialen waarin thermalizatie significant kan worden vertraagd. In deze context is de realisatie van langzame relaxatie van het $1P_e$ naar het $1S_e$ niveau niet afdoende, omdat de energie verbonden aan 1S-1P overgangen onvoldoende is om een extra elektron over de energy gap te exciteren. Voor de realisatie van efficiënte CM bij excitatie met zichtbaar licht is het nodig om (nano)materialen te verkrijgen waarin thermalizatie van hete ladingen (die een grote overmaat aan energie hebben) langzaam verloopt. Dit is een grote uitdaging.

Om de foto-gegenereerde excitonen in QDs om te zetten in een elektrische stroom is het noodzakelijk om elektronen en gaten te scheiden en laten migreren naar verschillende externe elektrodes. Een mogelijke configuratie om deze 'ladingsextractie' te realiseren is besproken in hoofdstuk 6, waarin QDs chemisch gebonden zijn aan een mesoporeuze oxide film, waarbij elektronen vanuit de QDs worden geïnjecteerd in het oxide. Dit concept is analoog aan de kleurstof zonnecel ('dye-sensitized solar cell' of 'Grätzel cell'), met als verschil dat QDs worden gebruikt als licht-absorberend materiaal in plaats van kleurstoffen. Gebruik makend van een breed scala aan spectroscopische technieken (Transiente Absorptie, THz-TDS en tijdsopgeloste luminescentie) in combinatie met stroommetingen aan complete zonnecellen, hebben we onderzoek gedaan naar elektron injectie vanuit de QDs in de oxide films. Elektron injectie in TiO_2 films werd niet geobserveerd, wat verklaard kan worden door de ongunstige positionering van het QD $1S_e$ niveau ten opzichte van het conductie band minimum van TiO_2. Elektron injectie naar SnO_2 films vond wel plaats, wat verklaard kan worden door de lagere positie van het SnO_2 conductie band minimum. Uit TEM plaatjes bleek dat, naast geïsoleerde QDs, clusters van QDs aanwezig zijn op het oppervlak van de oxide films. THz metingen gaven aan dat excitatie van de films resulteerde in de generatie van mobiele ladingen in deze QD clusters. De mobiele ladingen in de clusters recombineren binnen tientallen picosecondes (voordat extractie mogelijk was) en het is dus belangrijk om de vorming van QD clusters in QD zonnecellen te voorkomen. Een andere conclusie in hoofdstuk 6 was dat de interpretatie van spectroscopische signalen bemoeilijkt kan worden door de aanwezigheid van defecten op het QD-oxide oppervlak. Zo kan bijvoorbeeld het verval van de luminescentie intensiteit worden geïnterpreteerd als elektron injectie, maar het kan net zo goed worden verklaard

door trapping van ladingen in defecten of door energie overdracht binnen QD clusters. Om uit te sluiten dat spectroscopische data niet ten onrechte als elektron injectie wordt geïnterpreteerd, moeten spectroscopische metingen altijd gecomplementeerd worden met stroommetingen aan zonnecellen: detectie van een macroscopische stroom toont immers aan dat elektron injectie heeft plaatsgevonden.

In het algemeen is de kennis over elektron extractie uit QDs relatief beperkt. Het is dan ook instructief om kennis te nemen van het –analoge- onderzoek naar elektron injectie vanuit kleurstoffen naar oxides, omdat de parameters die elektron injectie bepalen dezelfde zijn voor beide systemen. Een systematische studie zal moeten uitwijzen wat de invloed van de density of accepting states in het oxide, de elektronische koppeling tussen het QD en het oxide, en de relatieve positionering van QD en oxide energie niveaus is op de tijdsschaal van ladingsextractie. Daarnaast zal onderzoek moeten worden gedaan naar het vinden van geschikte elektrolyt-oplossingen, aangezien de gebruikelijke elektrolyt in kleurstofzonnecellen (gebaseerd op een I^-/I_2 koppel) leidt tot fotodegradatie van QDs. Tegelijkertijd is het belangrijk om het effect van deze nieuwe elektrolyt op de injectie dynamica in kaart te brengen, omdat de exacte samenstelling van de elektrolyt sterk van invloed kan zijn op de snelheid van elektron injectie (zie hoofdstuk 7).

Concluderend, QDs werden in hoofdstuk 1 geintroduceerd als veelbelovende bouwstenen voor toekomstige zonnecellen vanwege hun speciale optische eigenschappen (hoge extinctie coëfficiënten en makkelijk te variëren energie gap) en vanwege hun speciale ladingsrecombinatie en relaxatie eigenschappen. Na 4 jaar onderzoek zijn QDs nog steeds veelbelovend voor toepassing in zonnecellen, maar er zijn wel diverse uitdagingen geïdentificeerd. Zo is het moeilijker dan eerder gedacht om intraband relaxatie van hete ladingen significant te vertragen en ook bleek de efficiëntie van CM in QDs niet zo hoog te zijn als eerder gerapporteerd. En ondanks het feit dat QDs excellente optische eigenschappen hebben, is de extractie van ladingen uit QDs in de richting van externe contacten veel minder eenvoudig dan in bijvoorbeeld silicium zonnecellen. Voordat QDs hun belofte kunnen waarmaken dienen nog diverse barrières geslecht te worden en aanzienlijk meer onderzoek is nodig om de fundamentele en technologische vraagstukken op te lossen die op dit moment de commercialisatie van QD zonnecellen in de weg staan.

Acknowledgement / Dankwoord

Soms wordt wel eens gezegd: 'promoveren, c'est mourir un peu'. In deze uitspraak zit zeker een kern van waarheid, terugdenkende aan de talloze meetsessies tot diep in de nacht, het worstelen met ondoorgrondelijke data, en recalcitrante samples die degraderen, oxideren of simpelweg geen signaal willen geven. Maar dit is natuurlijk maar één kant van het promotietraject: de dalen zijn soms diep, maar de pieken zijn hierdoor des te hoger. Deze pieken waren er tijdens eureka-momenten in het lab, maar minstens zo waardevol waren de mensen om me heen tijdens de vier jaar van mijn promotie-onderzoek.

Hiervoor wil ik allereerst mijn promotor Mischa Bonn bedanken. Toen ik solliciteerde voor een promotie-plek binnen jouw groep had ik eigenlijk niet de goede achtergrond qua opleiding, maar toch had je er vertrouwen in dat ik me snel genoeg zou kunnen 'omscholen'. Dit vertrouwen was kenmerkend voor hoe ik mijn verdere promotie heb ervaren: jij liet me altijd vrij om plannen te maken voor nieuwe experimenten, samenwerking met groepen in binnen- en buitenland op te zetten, en zelfs drie maanden lang te stoppen met promoveren om mee te doen aan de Nationale Denktank. Deze vrijheid heb ik zeer gewaardeerd. Verder heb ik tijdens mijn 'opleiding' veel van je geleerd over het kritisch beoordelen van data, het geven van overtuigende presentaties, en van je enthousiasme voor de wetenschap. Al met al had ik me geen betere promotor kunnen voorstellen dan jij.

Wetenschap is steeds meer een multidisciplinaire aangelegenheid en met alleen maar 'goed zijn in spectroscopie' kom je er tegenwoordig niet meer. Daarom was de intensieve samenwerking met meerdere mensen van de Universiteit van Utrecht zo waardevol: niet alleen vanwege de toegang tot 'state-of-the-art' (nano-)materialen, maar ook door de vele interessante discussies rondom de interpretatie van resultaten. Een speciaal woord van dank gaat uit naar mijn co-promotor Daniel Vanmaekelbergh. Je was mijn begeleider op afstand, maar ik heb veel gehad aan je kritische maar altijd constructieve opmerkingen. Ik heb altijd waardering gehad voor de integere manier waarop jij wetenschap bedrijft. Verder wil ik Celso de Mello Donegá, Rolf Koole, Arjan Houtepen en Wiel Evers bedanken voor het bijbrengen van de chemische kneepjes van het quantum dot vak en ook voor vele waardevolle discussies.

On the theoretical level, I would like to thank Christophe Delerue from the University of Lille for various useful contributions. Without your help, we could have never understood many of our experimental results to the extent that we understand them now.

The people who have surrounded me every day at AMOLF were the members of the Bakker and Bonn groups. A special place is reserved for the various THz-buddies over the years, who were not only colleagues but also friends. Euan and Mattijs, you had the difficult task to re-educate a chemical engineer into a spectroscopist and I admire the patience you had while executing this somewhat daunting task. Ronald and Klaas, for the majority of my PhD, the three of us were making up the 'THz-department'. Besides the fact that it was really good for me chemist to work together with two physicists, I think we had a very cooperative spirit in the Dave lab, resulting in many useful discussions and helping each other out with measurements and analysis. Memorable was of course the road trip along the US west coast in 2009. Thanks also for being my paranymphs! Domenico, your parmigiano will never be forgotten! Søren, Puck, Simon, and Enrique: good to see that the THz-flame is handed over to you guys; keep on the good spirit! Finally I would like to thank my colleagues from the first hour (Maaike, Maria, Sjors, Avi, and Han-Kwang) and all other members of the (significantly grown) Bakker/Bonn groups for the wonderful collegiality and friendship.

Promoveren is de diepte ingaan: hoe mooi dat vaak ook is, het is niet mogelijk om 4 jaar lang alleen op de bodem van de oceaan te zitten. Voor de nodige relativering, goede gesprekken, en het op z'n tijd afstand nemen van alle promotie-beslommeringen heb ik erg veel gehad aan de vele vrienden die door de jaren heen in mijn leven zijn gekomen. Helaas is hier geen ruimte om bij iedereen persoonlijk stil te staan, maar ik wil jullie allemaal bedanken voor de fijne momenten die ik met jullie heb mogen doorbrengen!

Tenslotte nog een laatste woord van dank voor mijn familie. Roos, jij was toch wel een beetje de wegbereider bij mijn keuze voor een promotie. Ik wens jou en Daphne alle goeds toe in de toekomst. Fons, gelukkig toch nog iemand in de familie die wel een band kan plakken. Heel veel succes bij het begaan van je eigen pad, ik heb er alle vertrouwen in! Papa en mama, toe ik onlangs weer eens door oude foto-albums bladerde, besefte ik weer hoeveel mooie herinneringen ik meedraag en hoeveel ik van jullie heb geleerd. Heel veel dank hiervoor!

Amsterdam, 17 maart 2010